UNIVERSITY OF SOUTHAMPTON

FACULTY OF ENGINEERING, SCIENCE AND MATHEMATICS

School of Engineering Sciences

Development of the Boundary Conditions Required for Simulating a Wave Tank using Smoothed Particle Hydrodynamics

by

Mark Pearce

Thesis for the degree of Doctor of Philosophy

April 2017

UNIVERSITY OF SOUTHAMPTON

ABSTRACT

FACULTY OF ENGINEERING, SCIENCE AND MATHEMATICS

SCHOOL OF ENGINEERING SCIENCES

Doctor of Philosophy

DEVELOPMENT OF THE BOUNDARY CONDITIONS REQUIRED FOR SIMULATING A WAVE TANK USING SMOOTHED PARTICLE HYDRODYNAMICS

By Mark Pearce

Smoothed Particle Hydrodynamics, SPH, is a Lagrangian method that has been applied to a number of fields including maritime applications. However little work has been done concerning the simulation of the motion of ships' hulls. A weakness of SPH is in the modelling of boundaries, both permeable and impermeable. This thesis investigates some of the latest SPH methods used to simulate these boundaries. Particular emphasis is placed upon the development of an approach that idealises the permeable inflow and outflow boundaries of a domain that are required to simulate the boundaries of a wave tank.

In the method presented the inflow boundary has been designed such that it can also generate waves. This allows for the simulation of a ship hull subject to head waves. The inflow boundary is also capable of creating a mean flow speed along with the wave generation. The outflow boundary serves as both a plane which allows particles that have crossed it to be removed and also incorporates a sponge layer that is designed to damp out incoming waves and prevent any unphysical wave reflection. These developments, used together, allow a small section of a wave tank to be simulated, this requires a minimum of computational resources.

Each new development has been tested against published data from experiments or numerical simulation. The computational models discussed in this thesis compare the performance of the new approach against experimental data and simulations using both classic SPH and Reynolds-Averaged Navier-Stokes methods. The wave generation and damping methods have been compared against the motion predicted by the Airy wave theory. The hull motion simulations have been compared against Wigley hull experimental data.

Table of Contents

List of Figures

List of Tables

List of Nomenclature

A - Smoothed particle hydrodynamics (SPH) approximation

r - SPH co-ordinates

W - Weighting function

h - Smoothing distance

m - Particle mass

ρ - Density

q - Non-dimensional particle distance

α_D - Particle distance

ν - Viscosity

P - Pressure

g - Acceleration due to gravity

Θ - Diffusion terms

∇ - Gradient operator

τ - Sub-particle stress (SPS) tensor

S_{ij} - Element of the SPS strain tensor

E_k - SPS turbulence kinetic energy

δ_{ij} - Delta function

C_s - Smagorinsky constant

Δ - Characteristic length of the filter function

C_l - Constant

Δl - Particle - particle spacing

B - Constant

γ - Constant

c_0 - Speed of sound at reference density

E - Coefficient

F - Force

D - Density contribution

V - Velocity contribution

v - Velocity of particle

t - Time

Ω - Volume of particle

n - Time step iteration

x - Longitudinal axis

y - Lateral axis

z - Vertical axis

$\vec{f}$ - Force applied by boundary particle

$\vec{n}$ - Normal of boundary

R - Repulsion function

G - Coefficient

ψ - Perpendicular distance of fluid particle to boundary

ξ - Projection of interpolation location joining two boundary particles

$u_{\perp}$ - Particle velocity onto normal

c_i - Particle speed of sound

Δb - Distance between 2 boundary particles

ε - Depth and normal velocity function

H_1 - User defined coefficient

H_2 - User defined coefficient

Z_{MIN} - Minimum approach distance

λ - Wavelength

a - Wave amplitude

d - Mean depth of fluid

k - Wavenumber

σ - Intrinsic angular frequency

ω - Observed angular frequency

U - Mean flow speed

θ - Wave phase

ξ_x - Horizontal motion of particle

c_p - Wave phase speed

u_s - Stokes' drift

steps - Time steps between adding particles

$\dot{W}_{New}$ - Modified vertical acceleration

$\dot{W}_{Original}$ - Original vertical acceleration

Z_{GAIN} - Damping tuning coefficient

W_{DAMP} - Damping factor

u - Longitudinal horizontal velocity

v - Lateral horizontal velocity

w - Vertical velocity

ρ_T - Target density

$\Delta\rho_d$ - Rate of change of density with depth

V_{GAIN} - Velocity tuning coefficient

$F_{OUTFLOW}$ - Force applied by outflow boundary particles

$F_{REPULSIVE}$ - Standard boundary particle repulsive force

ρ_{GAIN} - Density tuning coefficient

Error - Non-dimensional wave height error

$Result_{SIM}$ - Simulated result

$Result_{AIRY}$ - Airy wave theory predicted result

η - Wigley hull lateral axis

ζ - Wigley hull vertical axis

ι - Wigley hull longitudinal axis

WH_l - Wigley hull length

WH_b - Wigley hull breadth

WH_d - Wigley hull draught

a_2 - Wigley hull variable

a_4 - Wigley hull variable

α - Wigley hull variable

WH_v - Wigley hull volume of displacement

k_{yy} - Wigley hull radius of inertia for pitch

I_{yy} - Wigley hull pitch moment of inertia

X_{w3a}'' - Non-dimensional heave force

X_{w3a} - Maximum corrected heave force

C_{33} - Wigley hull static coefficient

X_{w1a}'' - Non-dimensional surge force

X_{w1a} - Maximum corrected surge force

X_{w5a}'' - Non-dimensional pitching moment

X_{w5a} - Maximum corrected pitching moment

C_{55} - Wigley hull static coefficient

z_a'' - Non-dimensional maximum vertical displacement

z_a - Maximum vertical displacement

θ_a'' - Non-dimnesional pitch angle

θ_a - Corrected maximum pitch angle

DECLARATION OF AUTHORSHIP

I, Mark Pearce

declare that the thesis entitled:

Development of the Boundary Conditions Required for Simulating a Wave Tank using Smoothed Particle Hydrodynamics

and the work presented in the thesis are both my own, and have been generated by me as the result of my own original research. I confirm that:

- this work was done wholly or mainly while in candidature for a research degree at this University;
- where any part of this thesis has previously been submitted for a degree or any other qualification at this University or any other institution, this has been clearly stated;
- where I have consulted the published work of others, this is always clearly attributed;
- where I have quoted from the work of others, the source is always given. With the exception of such quotations, this thesis is entirely my own work;
- I have acknowledged all main sources of help;
- where the thesis is based on work done by myself jointly with others, I have made clear exactly what was done by others and what I have contributed myself;
- none of this work has been published before submission.

Signed: …………………………………………………………………………..

Date:……………………………………………………………………………….

Acknowledgements

I would like to thank my supervisory team, Dr. Kenji Takeda, Dr. Dominic Hudson and Dr. Glyn Thomas, for their support and advice over the course of my doctorate. I would particularly like to thank Dr. Kenji Takeda for allowing me to be involved with the flight simulator laboratory that gave a welcome break to doctoral work. Thanks is also given to BAe Systems for providing the funding for the project.

I am very grateful to the team behind SPHysics for allowing their code to be freely available, without which the completion of this thesis would have been a much more arduous task. Special thanks should go to Dr. Benedict Rogers (The University of Manchester) who has provided further assistance when I had questions about SPHysics.

I would like to thank the members of the Southampton University Gliding Club for enabling me to participate in one of my favourite pastimes. I would also like to thank the staff at 622 Volunteer Gliding Squadron for allowing me to join their team and gain my wings.

Finally, and most importantly, I wish to thank my family for their support during my doctoral work; especially my father who provided the inspiration to become an engineer.

Chapter 1

Introduction

1.1 - Motivation

This dissertation concerns the development of a computer code that is capable of simulating maritime problems. Numerous methods exist that may be used for this purpose. However as computers get faster the scope of the problems that the methods are applied to increases. Older methods that are capable of solving some older problems may not be appropriate as technology advances. The motivation for the work in this thesis is the requirement to model ships in close proximity to each other in heavy seas, in real time. Many classical methods are not capable of simulating this situation as they either do not lend themselves to scaling to take advantage of newer, more powerful supercomputers or the method is not capable of capturing the physics of a complex hydrodynamic problem.

The Lagrangian method Smoothed Particle Hydrodynamics has been chosen as the methodology that is used in this thesis. Accordingly the open source Smoothed Particle Hydrodynamics code SPHysics (*http://www.sphysics.org*) has been modified and adapted to allow for suitable idealisation of the problem.

1.2 - Objectives

The objectives of this thesis are to:

1. Develop a robust inflow-outflow boundary condition that can allow a channel flow to be simulated in both two and three dimensions.
2. Create a wave generator that is capable of generating regular waves and works with the inflow boundary to generate a channel flow with waves.
3. Devise a wave damping mechanism that can be placed at the outflow end of the domain to damp out waves to prevent unwanted wave reflection. Combined with objectives 1 and 2 this will allow for the simulation of a wave tank.
4. Modify the floating body method within SPHysics to simulate a ships' hull.
5. Combine all of the features together to allow a floating body to be simulated in a wave tank with a mean flow.

1.3 - Novel Contributions

The following novel contributions to the field are discussed in this thesis:

1. The inflow boundary, which allows the simultaneous generation of regular waves and also a mean flow, has not been modelled in SPH with a free surface. Wave generation in most existing SPH methods only use a physical wave generator and do not require an inflow boundary.
2. The outflow boundary is adaptable to allow for different mean flow speeds without any requirement for tuning. It is also capable of damping out incoming waves to prevent significant wave reflection based upon a similar method that is used in other CFD methods.
3. The measurement of the heave and pitch forces, moments and motions of a generic hull form when subjected to regular head waves in a mean flow.

1.4 - Outline of Thesis

The layout of the thesis is outlined below:

Chapter 1 gives an introduction, describes the motivation behind the thesis and outlines the objectives.

Chapter 2 comprises of an extensive literature review that gives a full overview of the history of Smoothed Particle Hydrodynamics, the current state-of-the-art and identifies some drawbacks associated with the methodology. The literature review also outlines some other Computational Fluid Dynamics methods that have been used to simulate maritime problems.

Chapter 3 describes the methodology used by Smoothed Particle Hydrodynamics and the implementation of this methodology in SPHysics. The description of SPHysics is based upon the SPHysics user guide Gómez-Gesteira *et al* (2008). A number of key variables that can be chosen by the user are described.

Chapter 4 investigates and evaluates different boundary conditions used in different implementations of Smoothed Particle Hydrodynamics. The simulations in this chapter are based upon experiments and simulations in Yim *et al* (2008) and Crespo (2008).

Chapter 5 concerns wave generation. A new method has been devised that uses the Airy Wave Theory proposed by Airy (1841). The wave generation implementation is tested using a series of two dimensional cases to ensure that the waves are being generated and propagated correctly.

Chapter 6 describes the use of the wave generator outlined in chapter 5 to simulate a wave tank; the main focus of this chapter is a new implementation that damps out waves at the end of the wave tank to prevent unphysical wave reflection. The wave damping is achieved by the use of a sponge layer at the end of the wave tank that damps out incoming waves to such an extent that they will not be reflected and interfere with the incoming waves. A secondary part of this chapter involves the adaptation of the wave generator to allow a mean flow to be generated and an outflow method to regulate and remove particles once they have left the domain was devised. Both two and three dimensional test cases are described in this chapter, the main focus being that the waves are generated, propagated and dissipated correctly.

Chapter 7 combines all of the new features described in the previous chapters to allow for the simulation of a hull in a three dimensional wave tank. The forces and motions of the ships' hull to be measured. Computational results are compared against the experiments presented in Journée (1992).

Chapter 8 draws conclusions on the work presented in this thesis and suggest a way forward.

Chapter 2

Background and Motivation

2.1 - Literature Review

The first task for this project was to decide upon a Computational Fluid Dynamics (CFD) method that would give sufficient accuracy to model the problem and also be capable of being run at the required rate for use in a real-time simulation. The Lagrangian Smooth Particle Hydrodynamics (SPH) method was chosen for initial investigation. Originally this method was developed for modelling galaxies as described in Lucy (1977) and Gingold & Monaghan (1977). The method has recently begun to be used in the marine field and also in the computer and film graphics industry.

2.1.1 – CFD Methods Used to Simulate Water

A number of different methods have been used by various researchers to simulate water and vessels floating in the water. Two of the more established methods are Strip Theory and Reynolds Averaged Navier-Stokes (RANS). The method introduced by Kim & Shin (2007) is an example of Strip Theory being used to calculate the sea keeping characteristics of a Wigley hull in waves. Weymouth *et al* (2005), Price & Chen (2006), Quérard *et al* (2009) and Guo *et al* (2012) are examples of the use of RANS to predict ships' sea keeping response in waves. Weymouth *et al* (2005) uses the data presented by Journée (1992) to validate their method. Shibata *et al* (2012) use the Lagrangian Moving Particle Semi-Implicit (MPS) method to simulate a ships' hull in rough seas, concentrating on modelling the physics of waves breaking over the deck.

A newer and less mature method used in this field is SPH. An example of this method used to model ship motion has been presented by Cartwright *et al* (2006). SPH has also been used to simulate other cases detailed by Marsh *et al* (2010), Vacondio *et al* (2010), Colagrossi *et* al (2009) and De Padova *et al* (2010).

Any numerical method requires extensive validation before it can be accepted as a viable method that can be used. This validation process requires comparisons against experimental data. The data in Journée (1992), Lewis *et al* (2010) and

Gerritsma (1988) gives experimental data that is pertinent to the problems of this project. Yim *et al* (2008) present both experimental and numerical simulation data. Marrone *et al* (2012) use a parallel version of SPH to simulate the waves generated by a hull in a mean flow. In this work no attempt is made to damp out any waves at the outflow boundary.

2.1.2 - Overview of Smoothed Particle Hydrodynamics Methods

SPH was first developed by Lucy (1977) and Gingold and Monaghan (1977), originally developed to model astrophysical phenomena. A detailed description of the SPH methodology appears in chapter 3. What follows in this section is a brief account of the basics of the method. It solves partial differential equations of the field variables (for example density, velocity and energy), approximating the fluid as a set of particles. The partial differential equations are converted to ordinary differential equations with respect only to time by the use of a function approximation known as "kernel". The kernel approximation calculates the value of a field variable of a particle by: (a) summing the values of the nearest neighbour particles and (b) weighting the contribution of each neighbour by the distance between the two particles. If two particles are above a certain distance apart (chosen by the user) then the contribution will be zero. The ordinary differential equations are then solved using an explicit integration algorithm. This helps to determine the position of each particle at each time step.

Liu and Liu (2010) give an overview of recent research and progress on SPH methodology. Their paper identifies the advantages of using SPH over traditional grid based numerical methods as: 'treating large deformation, tracking free surfaces, moving interfaces and deformable boundaries'. All of these advantages are problems that are observed in modelling ship motion. For example, the ability to treat large deformation of the free surface is very useful when modelling heavy seas where the free surface will be deforming constantly. The moving interface between the water and the hull of a ship is also very important when trying to model the motion of a ship.

Shadloo *et al* (2012) compare the two main variants of the SPH method, namely weakly compressible and incompressible. The paper identifies that the main advantage of using a weakly compressible SPH method is that it is much easier to program. However, the weakly compressible method has a drawback in that it predicts very large oscillations in the pressure field. There is still some debate in the literature as to which SPH method is superior.

Kelager (2006) uses SPH to model small scale fluid simulations in real-time. The paper brings up a number of issues relevant to the project. Firstly when SPH is used in a small scale simulation, where fluids are usually seen as incompressible, a very small time step is required which can affect interactivity. Secondly performance issues were encountered relating to the processing hardware, requiring careful thought as to how the algorithm is implemented. Finally the paper states that for real-time fluid simulations a Langrangian method (such as SPH) is superior to an Eulerian method.

Vesterlund (2004) states that when using a graphics processing unit (GPU) for SPH calculations it is desirable to run the entire simulation on the GPU and not on a combination of central processing unit (CPU) and GPU as reading from the GPU memory can cause a decrease in simulation rate. Harada *et al* (2007) describe a method of running an SPH entirely on the GPU, using an nVidia 8800 GTX graphics card they are able to run an SPH simulation with 60,000 particles at a frame rate of 17 frames per second (FPS). This is a significant achievement using a graphics card that was state-of-the-art in 2006. Crespo *et al* (2010) uses a dual CPU-GPU method based on SPHysics that has been released as an open source code DualSPHysics. Oger *et al* (2010) takes a code that was developed to run on massively parallel computing architectures and converts it to hybrid CPU-GPU, preserving the message passing interface (MPI) architecture allowing multiple GPUs to be used. Ferrari *et al* (2009) implements an SPH scheme using the MPI standard to allow multiple processors to be used simultaneously. The dynamic load-balancing method has also been utilised. This method means that at all times each processor is handling almost the same number of particles as the others. For this reason the full power of each processor is constantly utilised.

Hoetzlein and Höllerer (2008) investigate the effect of hardware on computerefficiency. In the paper numerous other recent SPH papers are compared in terms of performance and efficiency.

Performance relates to the number of particles simulated multiplied by the number of frames per second. Efficiency is calculated as the performance divided by the number of floating point operations per second (Flops) of the hardware used. This paper shows that over time whilst performance has increased due to the increase in computational power available the efficiency has generally decreased.

Yim *et al* (2008) compare two modelling methods, namely a Reynolds-Averaged Navier-Stokes (RANS) simulation and an SPH simulation, with experimental data.

The experiment involves dropping a plunger, either with the plunger above the water or already partially submerged, into one end of a water trough and measuring the height of the waves created at certain points and the free surface profile at certain times. The experiment is devised so that it is essentially 2 dimensional. Of particular interest are the results of wave heights at certain points, the SPH model is less able than the RANS model to simulate the height of the trailing waves. This shows that for this SPH model damping is high.

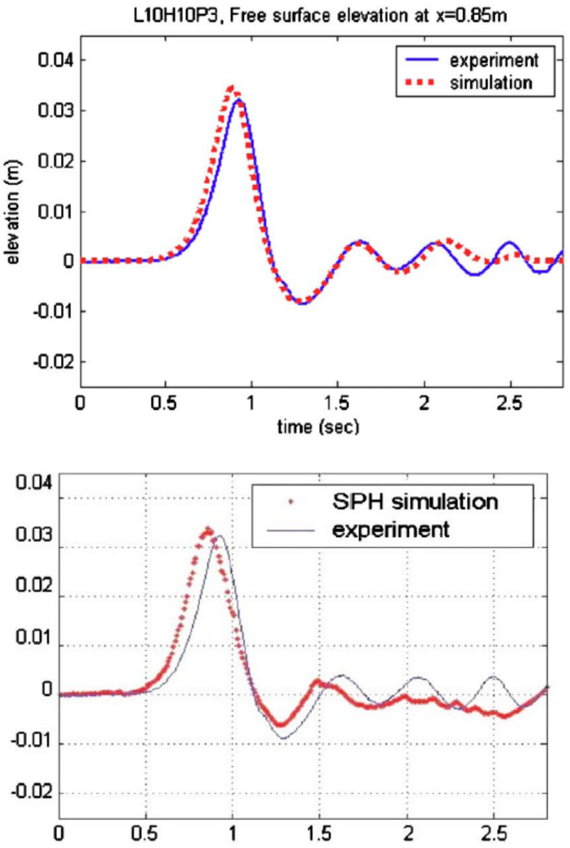

Figure 2.1: Graphs Showing Wave Height at a Fixed Point. Top: RANS Simulation Versus Experiment, Bottom: SPH Simulation Versus Experiment. Figure taken from Yim *et al* (2008).

Yim *et al* (2008) has significant relevance to this project as the plunger dropping into the water is a good model of a ships' hull heaving. It also highlights a significant drawback in the SPH method. Hoetzlein and Höllerer (2008) show that although over time computer power has increased corresponding increasing complexity of models used lead to a decrease in the efficiency of simulations.

Discussions in Ferrari *et al* (2009), Harada *et al* (2007), Vesterlund (2004) and Kelager (2006) are of particular relevance to this project. These papers investigate various aspects of running SPH simulations on multi-processor or GPU hardware.

This may be critical to any project that requires high-fidelity real time simulations. The dynamic load-balancing method described by Ferrari *et al* (2009) is especially important as it allows the maximum potential processing power of each processor to be utilised and therefore increase the computational efficiency of the simulation.

Groenenboom and Cartwright (2010) describe a new method of wave generation, using SPH. Rather than trying to model a physical wave maker (such as a plunger or paddle) the lower boundary of the computational domain is moved in accordance with analytical equations. In this paper deep water is simulated but the full depth is not modelled to reduce the computational expense. One advantage of this method is that the excessive wave damping often seen as waves propagate along a computational domain is not observed as the wave generator is located along the bottom of the domain rather than at one end.

Lind *et al* (2011) developed an incompressible SPH code that has been used to simulate a wave tank test case. The test case uses a paddle type wave maker to create regular waves and the propagation of these waves along the wave tank is compared to stream function theory analytical data. A sponge layer damping zone is used at the end of the wave tank to damp out waves and prevent wave reflection. The velocity of particles in the damping zone is damped out using a simple exponential function. The length of the damping zone is at least one wavelength. Clearly this will be a problem if the wavelength of the waves is very long (the sort of waves encountered at sea) as the damping zone would be very large, hence requiring huge computational resources.

Macià *et al* (2011) compare two commonly used SPH kernels, Gaussian and quintic (Wendland). Particular emphasis is placed on the flow patterns and energy dissipation mechanisms that occur when each kernel is used. The paper determines that for simulations where a free-surface is present the quintic (Wendland) kernel is superior to the Gaussian.

2.1.3 - The Importance of Smoothed Particle Hydrodynamics Solid Wall Boundary Conditions

Crespo (2008) defines three fundamental types of boundary conditions commonly used in SPH. These are: Ghost particles, Repulsive particles and Dynamic particles. Ghost particles, as detailed in Libersky & Petscheck (1991), Randles & Libersky (1996), Colagrossi & Landrini (2003) and Bierbrauer *et al* (2009), are created when a real particle moves within a certain distance of the boundary. The distance used is the kernel smoothing length. The ghost particle is created outside the system. It has the same pressure and density as its real counterpart, but opposite velocity. The disadvantage of this method is that the number of particles changes with each time step and therefore complicates its implementation in the code. This method would also have problems with modelling an object in a fluid if the thickness of the object were less than the kernel smoothing length. This is because the ghost particles associated with the normal fluid particles on the opposite side of the object may be placed outside the object, in the fluid.

Repulsive particles described in Monaghan (1994), Monaghan & Kos (1999) and Monaghan *et al* (2003) constitute fixed particles that form a boundary. If a normal fluid particle moves within a certain distance of a boundary particle a force is exerted on the normal fluid particle. The force can be described by the Lennard-Jones potential or a delta function. The method has been refined to use interpolation to minimise the effect of boundary particle spacing. Souto-Iglesias *et al* (2006) describe a problem with the repulsive method. When a simulation that requires a body of fluid at rest is begun the particles are not in equilibrium. Therefore it is necessary to run the simulation for some time until a state approximating to equilibrium has been reached.

Dynamic particles Dalrymple & Knio (2001) are boundary particles that satisfy the same equations as normal fluid particles but are fixed in space to form the boundary. Since the boundary particles are treated as being the same as the normal fluid particles the calculations can be done in the same loop. This saves computational time.

Particle type	Advantages	Limitations
Ghost	• The boundary particles are fluid particles, which simplifies the code implementation.	• Boundary particles may need to be created or destroyed in each time step. • Method may not work when the boundary is modelling a floating object.
Repulsive	• The repulsive force applied can be tuned according to the situation simulated.	• The simulation may require pre-calculation to allow the fluid to reach equilibrium.
Dynamic	• The boundary particles are fluid particles, which simplifies the code implementation.	• More boundary particles are required as the boundary must be at least as thick as the kernel smoothing length.

Table 2.1: Advantages and limitations of the boundary approaches used in SPH.

Souto-Iglesias *et al* (2010) investigates the shortfalls of the main methods used to model solid boundaries. Crespo (2008) considers the most basic scenario of a single particle in an inviscid medium without gravity being projected at a wall; the dynamic particle boundary method is used. The return point, the minimum distance to the wall over the smoothing distance, was calculated for a number of increasing initial particle velocities. The results show an almost straight line with negative slope on a graph of return point versus particle velocity. Although not shown on the graph, extrapolation would imply that above a certain velocity the particle would go through the boundary and therefore never return into the domain.

During SPH simulations it has been observed by numerous users that in some cases water particles can stick to the boundary walls. Narayanaswamy (2008) states that the particles sticking to boundaries creates a boundary layer that is not physically observed. They propose a new type of boundary condition that involves defining a number of virtual boundary grid cells placed next to, but inside the domain, the actual solid boundary. The average normal velocity of particles in each grid cell is forced to be zero; this enforces the no penetration constraint.

Vaughan (2009) proposes using line segments instead of particles for the repulsive method. This has the advantage of requiring far fewer elements than the equivalent particles and avoids the corrugated effect of using particles. He *et al* (2010) outlines a new method to allow fast solid boundary collision detection where a complex boundary geometry is required. Marrone *et al* (2010) details a variant of the ghost particle boundary method where instead of a ghost particle being created when a real particle moves close enough to the boundary the 'mirror' particle is always present. Ferrand *et al* (2010) proposes a novel method where the missing kernel support caused by the presence of a solid boundary is accounted for. This method allows a much better reproduction of the pressure field next to solid boundaries. Lehnart *et al* (2010) uses a method that involves modelling a solid boundary as a triangular surface mesh, the method also prevents fluid particles on opposite sides of a thin solid boundary from interacting with each other.

The problem of boundary conditions seems to be causing the most trouble for researchers; this is borne out by the number of papers written by researchers proposing solutions. It can be assumed therefore that this project will require a significant amount of work on this topic. The three main boundary conditions outlined by Crespo (2008) all have their benefits and drawbacks as described above. The papers in this section describe boundary conditions that model solid walls (usually simple flat walls), although this is not the only type of boundary that a marine simulator requires. The test case described by Crespo (2008) is also important as it implies that a wall using the dynamic boundary method is not impermeable as a real wall would be, the other methods will also suffer from this problem.

2.1.4 - Modelling Solid Objects and Open Boundary Conditions

The papers in this section consider how boundary conditions other than simple flat walls can be modelled in SPH.

Fernández-Méndez *et al* (2005) outlines a coupled method that uses the Finite Element Method (FEM) and SPH. FEM is used to model the boundary of a solid object, and therefore the inherit problems with enforcing boundary conditions is avoided. A transition region is used to couple the two methods; however this adds extra complexity to the simulation.

Fleissner & Eberhard (2007) describe a coupled Smoothed Particle Hydrodynamics – Discrete Element Method (DEM) formulation that uses SPH to model the fluid flow and DEM to model solid objects. This formulation uses two coupled methods that are both meshless particle methods and therefore do not suffer from the disadvantages of trying to couple a grid-based and a non-grid-based method.

Lastiwka *et al* (2009) present a method for modelling open boundary conditions (i.e. when the computational domain is a volume of the sea). Around the edges of the domain are inflow or outflow zones where new incoming particles are added and outgoing particles are removed. The properties, including velocity and position of the particles can be defined by the users. This allows a continuous or possibly variable flow rate to be modelled; also if the vertical position of the incoming particles is varied then the waves could be created. The paper also investigates the problem of undesired wave reflection from open boundaries and proposes a solution.

Federico *et al* (2010) also presents an open-boundary method that uses a very similar method to that proposed in Lastiwka *et al* (2009). Chang and Chang (2012) further extend the open-boundary method described by Federico *et al* (2010) to use for non-rectangular channel flows. Cherfils *et al* (2010) details a method of modelling the solid boundaries of immersed objects with complex geometries. The method is a variant of the ghost particle method. Shadloo *et al* (2010) uses the Multiple Boundary Tangents method to model solid boundaries of complex shapes. This method is also a variant of the ghost particle method. Mahmood *et al* (2012) extend the methodology proposed in Lastiwka *et al* (2009) to 2 dimensions and also to allow turbulent flows to be simulated.

Rogers *et al* (2003) uses the dynamic boundary particle method detailed in Dalrymple & Knio (2001) to model the flow past a submerged hydrofoil. The boundaries are used to model the hydrofoil, seabed and inflow & outflow boundaries. However it is found that a much larger than expected boundary layer around the hydrofoil is created. This may be a consequence of the spatial resolution, and hence the number of fluid particles, chosen.

Delorme *et al* (2009) describe some methods for calculating the pressure at certain points in a fluid, including on a solid surface. This allows the force applied by a body of fluid on a solid body to be calculated. The merits and drawbacks of each method are described and a new method that uses the ghost particle boundary method is outlined. The paper also investigates the accuracy of using SPH to simulate waves breaking on a solid object.

Vandamme *et al* (2011) outline the use of weakly compressible SPH to model a floating body, with particular emphasis on a body impacting with a free surface. The simulation results show good agreement with experimental data, particularly the free-surface deformation. The authors suggest that the benefits of modelling the effect of air-water interaction is also important in these impact test cases. Bouscasse *et al* (2012) use SPH to model the bow wave generated by a ships' hull. Particular emphasis is placed upon the dynamics of the breaking waves generated by the hull. Further emphasis is placed upon the motion of the flow under the free surface.

The hull of a ship is a complex shape and therefore a ship simulator will require a solid wall boundary condition capable of various complex geometries. Fernández-Méndez *et al* (2005) and Fleissner & Eberhard (2007) describe an alternate boundary condition method to those described in Crespo (2008), both using a different CFD method to model the boundary conditions and then coupling this method to the SPH method used to simulate the rest of the flow. Whilst this increases the complexity and possibly decreases the efficiency of the simulation there is an improvement in the quality of the results.

As mentioned in the previous section boundary conditions are a problem area in SPH. The following papers have particular relevance to this project. Lastiwka *et al* (2009) outline a method that models an open boundary, as required when the computational domain does not end in a wall, this will almost certainly be required by a ship simulator. The method will also allow the creation of sea states, which are required by the project description. The calculation of pressure, and therefore force when multiplied by surface area, detailed by Delorme *et al* (2009) is very important as this will allow the motion of the simulated fluid to apply a force to the hull(s) of the ship(s) in the simulation. However, it must be noted that this paper only concerns the calculation of forces when the ghost particle boundary condition is used.

Modave *et al* (2010) describe the use of an absorbing sponge layer around the boundaries of the computational domain to model an open boundary that damps out waves that are leaving the domain to prevent wave reflection. This method uses a target solution, which is often that the wave is damped out completely, each time step the waves that are in the sponge layer are nudged slightly towards the target solution. The effectiveness of the damping is varied so that there is no damping at the boundary between the simulation domain and the sponge layer, as this can cause unwanted wave reflection off that boundary. The effectiveness of the damping can also be tuned and the size of the sponge layer varied to ensure that the desired wave damping occurs with the minimum amount of extra computational resources.

Vignjevic and Powell (2011) use a non-reflecting boundary condition coupled with a multi-scale SPH scheme. The method is capable of preventing wave reflection off an outflow boundary with minimal extra computational effort but, at present, the method is only able to achieve its objectives where the wave is normal to a straight boundary.

2.2 - Conclusions

Smoothed Particle Hydrodynamics is a maturing CFD method that has recently been applied to more practical applications. The method has advantages over Eulerian methods, especially in the ability of SPH to handle free surface deformation easily. There are still weaknesses in the method; one of the major weaknesses is the modelling of boundaries, both solid (non-permeable) and permeable. The modelling of boundaries is of particular importance to the problems that are to be addressed in this thesis. A number of methods that have been used by others have been identified in this chapter. However none of them are capable of correctly simulating the open boundaries.

Progress has also been made in adapting the method to high performance computing simulations that have a sufficient spatial resolution and run time to allow accurate simulations of test cases to be conducted.

Chapter 3

Smoothed Particle Hydrodynamics (SPH) and SPHysics

3.1 - Introduction

The simulation method chosen for this project is Smoothed Particle Hydrodynamics (SPH), the methodology of which will be described in this section. The open source SPH code SPHysics is used in the simulations presented in this thesis. The main part of this chapter describes the formulation of SPHysics.

3.2 - SPH Background

There are two fundamental ways of describing the governing equations that are used in Computational Fluid Dynamics (CFD) methods, these are the Eulerian and Lagrangian descriptions. The Eulerian description is a spatial description. A very commonly used Eulerian method is the finite difference method. The Lagrangian description is based upon the material or fluid itself. A frequently used method is the finite element method. Both of these approaches have been successfully used as grid based methods. The Lagrangian grid moves with the material and is frequently used for modelling solid materials as the method is very suited to simulations where there is little deformation. Conversely, the Eulerian grid is fixed in space, the flux of mass, momentum and energy across the boundaries of cells in the grid is used to calculate the distribution of the material within the grid. This allows large deformations of the material or fluid to occur as this does not affect the grid, which is fixed in space. This means that Eulerian grid methods are frequently used to simulate fluid dynamics.

Despite the successful application of grid based methods in computational fluid dynamics there are a number of drawbacks that are inherent with using a grid based method.

The first drawback is in generating the grid itself; this can be an incredibly complex task, depending on the nature of the problem being solved. A second drawback, that is of particular importance for free surface simulation, is determining precisely where the free surface is located when using an Eulerian grid method can be difficult.

To eliminate the problems in using grid based methods for computational fluid dynamics there have been a number of new computational methods proposed that do not use a grid. These are the meshfree or meshless methods. A list of typical meshfree methods appears in table 4.1 below. The methods appear in chronological order.

Method	**References**	**Method of approximation**
Smoothed Particle Hydrodynamics	(Lucy, 1977) and (Gingold and Monaghan, 1977)	Integral representation
Finite Point Method	(Liszka and Orkisz, 1980)	Finite difference representation
Diffuse Element Method	(Nayroles *et al*, 1992)	Moving Least Square (MLS) approximation, Galerkin method
Element Free Galerkin Method	(Belytschko *et al*, 1994)	MLS approximation, Galerkin method
Reproduced Kernel Particle Method	(Liu *et al*, 1995)	Integral representation, Galerkin method
HP-Cloud Method	(Duarte and Oden, 1996)	MLS approximation, partition of unity
Free Mesh Method	(Yagawa and Yamada, 1996)	Galerkin method
Meshless Local Petrov-Galerkin Method	(Atluri and Zhu, 1998)	MLS approximation, Petrov-Galerkin method
Point Interpolation Method	(Liu and Gu, 1999)	Point interpolation, Galerkin or Petrov-Galerkin
Meshfree Weak-Strong Form	(Liu and Gu, 2002)	MLS, point interpolation, collocation, Petrov Galerkin

Table 3.1: Typical meshfree methods.

A sub-division of the new meshfree methods are meshfree particle methods. These methods use discrete particles to represent the material or fluid. Most meshfree particle methods are Lagrangian methods in which the particles move according to internal and external forces imposed on them. However, some meshfree particle methods are Eulerian methods where the particles are positioned in way of fixed interpolation points. The time integration scheme that is most commonly used by meshfree particle methods is the explicit method. There are some exceptions that use implicit methods. The explicit method calculates the future state of a system by using the current state of the system plus a small time step. The implicit method solves an equation that includes both the current and future states of the system. The implementation of an implicit method is more difficult to implement in practical terms. However, if the explicit method is used some problems will require the use of a very small time step which is computationally very expensive. In this case the implicit method may be the preferred implementation even though it is more difficult to implement.

The following are advantages of using a meshfree particle method over the more conventional grid based methods:

- The domain is discretised by using particles instead of a grid the treatment of large deformations (such as would be expected when simulating free surface waves) is much easier.
- The discretisation of a complex domain is simpler as only an initial discretisation is required.
- It is easy to determine the features of a system such as the free surface, moving interface or deformable boundary.

3.3 – SPHysics Method

SPHysics is an open source SPH code. It uses a weakly compressible formulation. There are a number of serial (single processor) versions available: 1.4, 2.0, 2.2 and 2.2.001. It allows 2D and 3D simulation, choice of kernel, dynamic or repulsive boundary conditions, choice of viscosity treatment and moving objects (including floating objects in version 2.0 onwards). The dynamic boundary particle method uses normal fluid particles which are fixed in space to model the boundary. The repulsive boundary particle method uses boundary particles which apply a repulsive force on any normal fluid particle that moves into the range of influence of the boundary. In each case the objective of the boundary is to simulate a solid wall which fluid particles should not penetrate. The code has also been adapted to be used in a parallel environment and also on Graphics processing unit (GPUs).

The following methodology is taken from the user guide for serial SPHysics Gómez-Gesteira *et al* (2008).

3.3.1 – The SPH Method

The fundamental principle behind SPH is to approximate any function as:

$$A(\vec{r}) = \int A(\vec{r})W(\vec{r} - \overrightarrow{r'}, h)d\overrightarrow{r'} \tag{3.1}$$

Where h is the smoothing distance and $W(\vec{r} - \overrightarrow{r'}, h)$ is the weighting function, also known as the kernel. Using equation 3.1 an approximation of the function at a particle (a) can be made:

$$A(\vec{r}) = \sum_b m_b \frac{A_b}{\rho_b} W_{ab} \tag{3.2}$$

Where the summation is over all particles within the smoothing distance of particle a, m_b and ρ_b are mass and density respectively and $W_{ab} = W(\vec{r}_a - \vec{r}_b, h)$ is the kernel.

3.3.2 – The Smoothing Kernel

The kernel should satisfy several conditions such as positivity, compact support and normalisation, they must also be decreasing monotonically with increasing distance from particle a and behave like a delta function when h approaches zero.

- Normalisation: The smoothing function must be unity over its support domain, $\int W(\vec{r} - \overrightarrow{r'}, h)d\overrightarrow{r'} = 1$.
- Compact Support: The smoothing function must be zero if the distance between two particles is greater than the smoothing distance multiplied by a scalar (i.e. the particles are not within each others' support domain). This property transforms the SPH approximation from a global operation to a local operation.
- Positivity: $W(\vec{r}_a - \vec{r}_b, h) \geq 0$ for any point within the support domain. This is of particular importance when simulating fluids as if the function becomes negative there is a possibility for fluid particles to have negative density or energy.
- Decreasing monotonically: This property is based upon the physical consideration that a nearer particle should have greater influence on the concerned particle.

Kernels depend on the smoothing distance, h, and the non-dimensional distance between particles, q, where $q = \frac{r}{h}$ and r is the distance between particles a and b. Any particles which are beyond the smoothing distance of a particle have no effect on that particle. There are a number of different kernels that can be used:

- Gaussian: $$W(r,h) = \alpha_D \exp(-q^2) \quad (3.3)$$

Where α_D is $\frac{1}{\pi h^2}$ in 2D and $\frac{1}{\pi^{3/2} h^3}$ in 3D.

- Quadratic: $$W(r,h) = \alpha_D \left[\frac{3}{16}q^2 - \frac{3}{4}q + \frac{3}{4}\right] \quad 0 \leq q \leq 2 \quad (3.4)$$

Where α_D is $\frac{2}{\pi h^2}$ in 2D and $\frac{5}{4\pi h^3}$ in 3D.

- Quintic (Wendland): $$W(r,h) = \alpha_D \left(1 - \frac{q}{2}\right)^4 (2q+1) \quad 0 \leq q \leq 2 \quad (3.6)$$

Where α_D is $\frac{7}{4\pi h^2}$ in 2D and $\frac{7}{8\pi h^3}$ in 3D.

3.3.3 – The Momentum Equation

The momentum conservation equation in a continuum field is:

$$\frac{D\vec{v}}{Dt} = -\frac{1}{\rho}\vec{\nabla}P + \vec{g} + \vec{\Theta} \quad (3.7)$$

Where Θ refers to diffusion terms.

Where $\vec{g} = (0, 0, -9.81)\ ms^{-2}$ is gravitational acceleration.

The following section describes the full viscosity method (laminar viscosity + sub-particle scale (SPS) turbulence):

The momentum conservation equation is:

$$\frac{D\vec{v}}{Dt} = -\frac{1}{\rho}\vec{\nabla}P + \vec{g} + \nu_0 \nabla^2 \vec{v} + \frac{1}{\rho}\nabla\vec{\tau} \quad (3.8)$$

Where $\vec{\tau}$ represents the SPS tensor. The laminar stress term simplifies to:

$$(\nu_0 \nabla^2 \vec{v})_a = \sum_b m_b \left(\frac{4\nu_0 \vec{r}_{ab} \vec{\nabla}_a W_{ab}}{(\rho_a + \rho_b)|\vec{r}_{ab}|^2}\right) \vec{V}_{ab} \quad (3.9)$$

Where ν_0 is the kinetic viscosity of laminar flow (10^{-6} m^2s^{-1}).

The eddy viscosity assumption (Boussinesq's hypothesis) is often used to model the SPS tensor using Favre-averaging (for a compressible fluid). Favre averaging is used to separate the turbulent fluctuations from the mean flow:

$$\frac{\tau_{ij}}{\rho} = 2v_t S_{ij} - \frac{2}{3} E_k \delta_{ij} - \frac{2}{3} C_I \Delta^2 \delta_{ij} \left|S_{ij}\right|^2 \tag{3.10}$$

Where $\vec{\tau}_{ij}$ is the sub-particle stress tensor, $v_t = [min(C_s \Delta l)]^2 |S|$ the turbulence eddy viscosity, E_k the SPS turbulence kinetic energy, C_s the Smagorinsky constant (0.12), $C_I = 0.0066$, Δl the particle-particle spacing and $|S| = \left(2S_{ij}S_{ij}\right)^{\frac{1}{2}}$, where S_{ij} is the element of SPS strain tensor.

So, equation 3.8 can be re-written as:

$$\frac{d\vec{v}_a}{dt} = -\sum_b m_b \left(\frac{P_b}{\rho_b^2} + \frac{P_a}{\rho_a^2}\right) \vec{\nabla}_a W_{ab} + \vec{g} +$$

$$\sum_b m_b \left(\frac{4v_0 \vec{r}_{ab} \nabla_a W_{ab}}{(\rho_a + \rho_b)|\vec{r}_{ab}|^2}\right) \vec{V}_{ab} + \sum_b m_b \left(\frac{\tau_b}{\rho_b^2} + \frac{\tau_a}{\rho_a^2}\right) \vec{\nabla}_a W_{ab} \tag{3.11}$$

3.3.4 – The Continuity Equation

The continuity equation calculates changes in fluid density:

$$\frac{d\rho_a}{dt} = \sum_b m_b \vec{v}_{ab} \vec{\nabla}_a W_{ab} \tag{3.12}$$

3.3.5 – Equation of State

The fluid in SPH is treated as weakly compressible; this allows the use of an equation of state to calculate fluid pressure. The compressibility is adjusted so that the speed of sound is slow enough to allow the time step to be reasonable. The relationship between density and pressure is assumed to follow the expression:

$$P = B\left[\left(\frac{\rho}{\rho_0}\right)^\gamma - 1\right] \tag{3.13}$$

Where $\gamma = 7$, $B = c_0^2 \frac{\rho_0}{\gamma}$ where $\rho_0 = 1000\, kg\, m^{-3}$ and $c_0 = c(\rho_0) = \sqrt{(\partial P / \partial \rho)}\Big|_{\rho_0}$.

3.3.6 – Moving the Particles

Particles are moved using:

$$\frac{d\vec{r}_a}{dt} = \vec{v}_a + E \sum_b \frac{m_b}{\overline{\rho_{ab}}} \vec{v}_{ba} W_{ab} \tag{3.14}$$

Where $E = 0.5$ and $\overline{\rho_{ab}} = \frac{(\rho_a + \rho_b)}{2}$.

3.3.7 – Density Filter

Whilst the dynamics of SPH simulations are generally realistic the pressure field can exhibit large pressure oscillations. One of the simplest ways of accounting for this is to perform a filter over the density of the particles.

- Zeroth order – Shepard filter:

The following procedure is applied every 30 time steps:

$$\rho_a^{new} = \sum_b \rho_b \widehat{W}_{ab} \frac{m_b}{\rho_b} = \sum_b m_b \widehat{W}_{ab} \tag{3.15}$$

Where the kernel has been corrected using zeroth-order correction:

$$\widehat{W}_{ab} = \frac{W_{ab}}{\sum_b W_{ab} \frac{m_b}{\rho_b}} \tag{3.16}$$

3.3.8 – Time Stepping

Consider the momentum (equation 3.7), density (equation 3.12) and position (equation 3.14) in the following form:

$$\frac{d\vec{v}_a}{dt} = \vec{F}_a \tag{3.17}$$

$$\frac{d\rho_a}{dt} = D_a \tag{3.18}$$

$$\frac{d\vec{r}_a}{dt} = \vec{V}_a \tag{3.19}$$

Where $\vec{F}_a$ represents the force contribution from particle *a* and the neighbouring particles. D_a represents the density contribution from particle *a* and the neighbouring particles. $\vec{V}_a$ represents the velocity contribution from particle *a* and the neighbouring particles.

Two time stepping schemes that are available in SPHysics have been used in the simulations presented in this thesis. They are the Predictor-Corrector scheme described by Monaghan (1989) and the Symplectic scheme. The Predictor-Corrector scheme was used in the simulations presented in chapter 4 as it was the only time stepping scheme that had been implemented in the version of SPHysics used. The Symplectic scheme was used in the simulations presented in chapters 5, 6 and 7 as it was found to be the best scheme available in SPHysics in terms of simulation stability.

- Predictor-Corrector Scheme:

This scheme predicts the evolution in time as:

$$\vec{v}_a^{n+1/2} = \vec{v}_a^{n} + \frac{\Delta t}{2}\vec{F}_a^{n} ; \quad \rho_a^{n+1/2} = \rho_a^{n} + \frac{\Delta t}{2} D_a^{n}$$

$$\vec{r}_a^{n+1/2} = \vec{r}_a^{n} + \frac{\Delta t}{2}\vec{V}_a^{n} \tag{3.20}$$

Calculating $P_a^{n+1/2} = f\left(\rho_a^{n+1/2}\right)$ according to equation 3.18.

These values are then corrected using forces at the half step:

$$\vec{v}_a^{n+1/2} = \vec{v}_a^{n} + \frac{\Delta t}{2}\vec{F}_a^{n+1/2} ; \quad \rho_a^{n+1/2} = \rho_a^{n} + \frac{\Delta t}{2} D_a^{n+1/2}$$

$$\vec{r}_a^{n+1/2} = \vec{r}_a^{n} + \frac{\Delta t}{2}\vec{V}_a^{n+1/2} \tag{3.21}$$

Finally, the values are calculated at the end of the time step:

$$\vec{v}_a^{n+1} = 2\vec{v}_a^{n+1/2} - \vec{v}_a^{n}; \quad \rho_a^{n+1} = 2\rho_a^{n+1/2} - \rho_a^{n}$$

$$\vec{r}_a^{n+1} = 2\vec{r}_a^{n+1/2} - \vec{r}_a^{n} \tag{3.22}$$

Finally, the pressure is calculated from density using $P_a^{n+1} = f(\rho_a^{n+1})$.

- Symplectic Scheme:

The values of density and acceleration are calculated in the middle of the time step:

$$\rho_a^{n+\frac{1}{2}} = \rho_a^{n} + \frac{\Delta t}{2}\frac{d\rho_a^{n}}{dt}; \quad \underline{r}_a^{n+\frac{1}{2}} = \underline{r}_a^{n} + \frac{\Delta t}{2}\frac{d\underline{r}_a^{n}}{dt} \tag{3.23}$$

Where the superscript n denotes time step and $t = n\Delta t$. Pressure $p_a^{n+\frac{1}{2}}$ is calculated using the equation of state. In the second stage $\frac{d(\Omega_i\rho_i\underline{v}_i)^{n+\frac{1}{2}}}{dt}$ gives the velocity and hence the position of the particles at the end of the time step:

$$(\Omega_a\rho_a\underline{v}_a)^{n+1} = (\Omega_a\rho_a\underline{v}_a)^{n+\frac{1}{2}} + \frac{\Delta t}{2}\frac{d(\Omega_a\rho_a\underline{v}_a)^{n+\frac{1}{2}}}{dt}\ ;\quad \underline{r}_a^{n+1} = \underline{r}_a^{n+\frac{1}{2}} + \frac{\Delta t}{2}\underline{v}_a^{n+1} \tag{3.24}$$

At the end of the time step $\frac{d\rho_a^{n+1}}{dt}$ is calculated using updated values of $\underline{v}_a^{n+1}$ and $\underline{r}_a^{n+1}$.

3.4 – Boundary Conditions

Two solid boundary conditions are implemented in SPHysics: Dynamic and Repulsive. Modifications are required to allow modelling of such features as permeable non-reflecting boundary conditions and wave generators. A non-reflecting boundary must have the ability to damp out the energy of incoming waves to prevent the reflection of this energy back into the simulation domain. Wave generators, often modelled as a physical paddle that has a prescribed motion, need to be able to generate waves to the required specifications of the user.

3.4.1 – Dynamic Boundary Conditions

The boundary particles are treated in exactly the same manner as the fluid particles, however they do not move, unless they represent a moving boundary. In such case they move in some pre-determined fashion. The boundary particles are arranged in a staggered manner as shown in figure 3.1. In figure 3.1 dx and dz are the spatial resolution in the x and z axes. The thickness of a dynamic boundary must be chosen . When a fluid particle approaches a boundary the density of the boundary particles increases according to equation 3.12, resulting in a pressure increase following equation 3.13. Thus, the force exerted on the fluid particle increases due to the pressure term (P/ρ^2) in the momentum equation (equation 3.11).

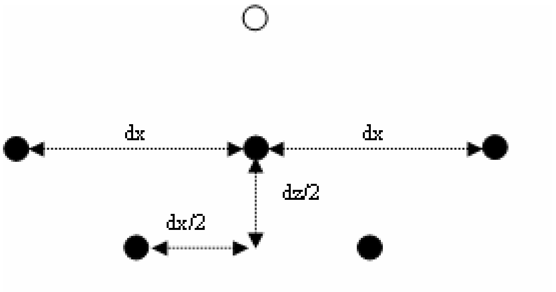

Figure 3.1: Arrangement of dynamic boundary particles shown in black. Figure taken from Gómez-Gesteira *et al*, (2008).

3.4.2 – Repulsive Boundary Conditions

The repulsive boundary condition uses boundary particles that exert a repulsive force on any fluid particle that is within the range of influence of the boundary particle. If a boundary and fluid particle are separated by distance r the force per unit mass has a form given by the Lennard-Jones potential, as described in Lennard-Jones (1924). Another approach is to assume the existence of forces in the boundary, which can be described by a delta function. This method has been refined by means of an interpolation process, minimising the inter-spacing effect of the boundary particles on the repulsion force of the boundary as described by Monaghan & Kos (1999)

Following this approach, the force experienced by a water particle, $\vec{f}$, acting normal to the wall, is given by:

$$\vec{f} = \vec{n}R(\psi)P(\xi)\varepsilon(z,u_{\perp}) \tag{3.25}$$

Where $\vec{n}$ is the normal of the boundary. The distance ψ is the perpendicular distance of the particle from the boundary , while ξ is the projection of the interpolation location ξ_i onto the chord joining the two adjacent boundary particles and $u_{\perp}$ is the velocity of the water particle projected onto the normal. The repulsion function, $R(\psi)$, is evaluated in terms of the normalised distance from the wall, $q = \psi/2h$, as:

$$R(\psi) = G\frac{1}{\sqrt{q}}(1-q) \tag{3.26}$$

Where the coefficient G is:

$$G = \frac{1}{h} 0.01 c_i^2 \tag{3.27}$$

c_i being the speed of sound of particle i.

The function $P(\xi)$ is chosen so that a fluid particle experiences a constant a repulsive force when travelling parallel to the wall:

$$P(\xi) = \frac{1}{2}\left(1 + \cos\left(\frac{2\pi\xi}{\Delta b}\right)\right) \tag{3.28}$$

Where Δb is the distance between two adjacent boundary particles. Finally, the function $\varepsilon(z, u_\perp)$ adjusts the magnitude of the force according to the local water depth and velocity of the water particle normal to the boundary:

$$\varepsilon(z, u_\perp) = \varepsilon(z) + \varepsilon(u_\perp) \tag{3.29}$$

Where:

$$\varepsilon(z) = \begin{cases} 0.02 & z \geq 0 \\ |z/h_0| + 0.02 & 0 > z \geq -h_0 \\ 1 & |z/h_0| > 1 \end{cases} \tag{3.30}$$

And

$$\varepsilon(u_\perp) = \begin{cases} 0 & u_\perp > 0 \\ |20u_\perp|/c_0 & |20u_\perp| < c_0 \\ 1 & |20u_\perp| > c_0 \end{cases} \tag{3.31}$$

In equations 3.29, 3.30 and 3.31, z is the elevation above the local still-water level h_0, $u_\perp = (\vec{v}_{WP} - \vec{v}_{BP}) \cdot \vec{n}$, where subscripts WP and BP refer to water and boundary particles respectively, and $c_0 = \sqrt{B\gamma/\rho_0}$ the speed of sound at the reference density. The system of normals requires each boundary particle to know the coordinates of its immediate neighbours. In 2D boundary particle i is surrounded by i-1 and i+1 so that the tangential vector is given by:

$$\vec{t} = (\vec{r}_{i+1} - \vec{r}_{i-1})/|\vec{r}_{i+1} - \vec{r}_{i-1}| \tag{3.32}$$

So that the normal is then found from $\vec{n}\vec{t} = 0$.

An alteration was made to the standard SPHysics repulsive boundary method in an attempt to reduce the effect of solid wall penetration that had been identified in the single particle test cases. The aim of the alteration was to increase the force that the repulsive boundary particles applied to a fluid particle that was very close to the boundary. This was done because a particle that is very close to a boundary is very close to penetrating the boundary.

The alteration was made to the standard SPHysics repulsive boundary condition and has been used for all 2D and 3D test cases presented in chapters 4, 5, 6 and 7. This alteration is to equation 3.26, which in standard SPHysics uses a delta function; this has been altered to a Lennard-Jones function (as described in Lennard-Jones (1924)):

$$R(\psi) = 4\left(\left(\frac{1}{q}\right)^{0.45} - \left(\frac{1}{q}\right)^{0.2}\right) \qquad (3.33)$$

The coefficients were chosen to ensure that when the fluid particle is not very close to the wall the repulsive force is as similar as possible to the original delta function but when the fluid particle is very close to the wall the applied force is greater than would be the case if the delta function were used. This should reduce the likelihood of a fluid particle penetrating a solid boundary. A comparison of the standard SPHysics delta function (equation 3.26) and the Lennard-Jones potential (equation 3.33) is shown in figure 3.2.

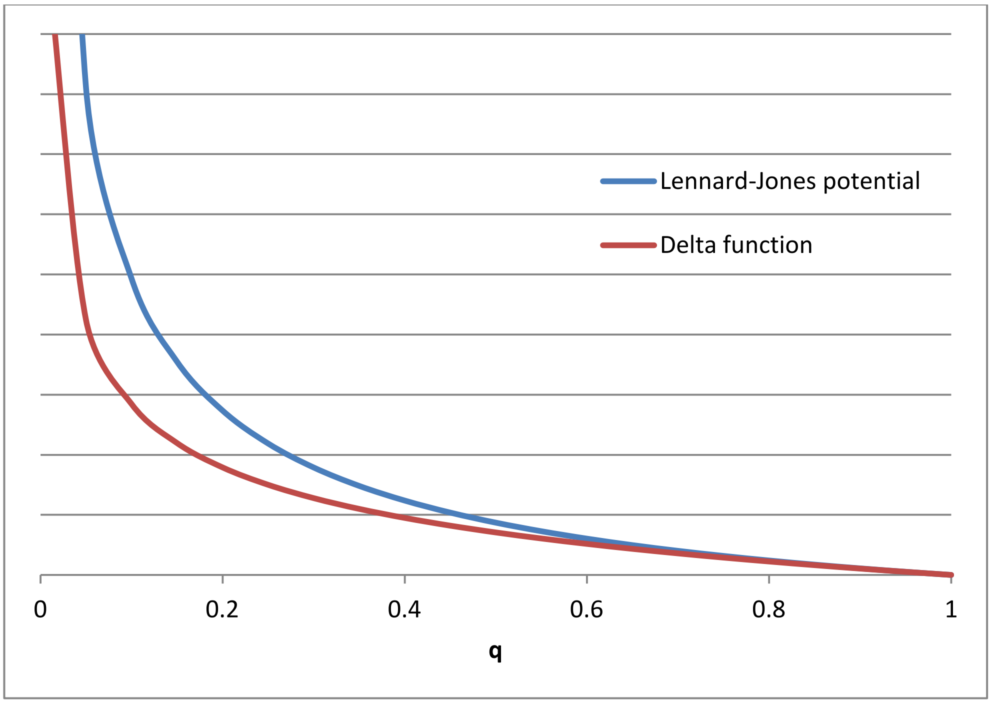

Figure 3.2: Comparison of the Delta function and Lennard-Jones potential.

The repulsive boundary condition is the only boundary condition that can be used in the current version of SPHysics if a floating body is to be used. However the decision to use the repulsive boundary condition was made before the floating body mechanism was introduced to SPHysics. The repulsive boundary condition uses fewer boundary particles than the dynamic boundary condition which is an advantage in terms of computational resources.

Chapter 4

SPH Boundaries

4.1 - Introduction

Yim *et al* (2008) and Crespo (2008) both outline test cases using Smoothed Particle Hydrodynamics (SPH); this section covers a number of test cases. The first of these is an extension of the single particle test case in Crespo (2008), the second is an attempt to replicate the simulation found in Yim *et al* (2008).

4.2 – Creating the Permeable Non-Reflecting Open Boundary

A number of the test cases that have been identified in the literature review require a simulation domain that is not always bound by solid boundaries (e.g. Yim *et al* (2008), Journée (1992)). This requires the use of a permeable non-reflecting open boundary which is not yet implemented in SPHysics. The main requirement of the non-reflecting open boundary is that if a wave impacts on the boundary the energy of the wave leaves the domain and there is no reflected wave.

Two attempts were made at implementing a non-reflecting open boundary in SPHysics. Each method was first tested by running 2D simulations of a water tank with the right wall being a non-reflecting open boundary. The test criterion was to ensure that when the fluid was static no fluid left the domain. The next test was to use a wave maker to create a wave that must leave the domain with no reflected wave being created by the non-reflecting open boundary.

The first attempt involved modifying equation 3.26 so that if the distance between the boundary and fluid particles is greater than the smoothing length, h, the applied force is zero; otherwise the force applied is constant by setting the normalised distance from the boundary, q, to 0.5. This method was flawed as it still included the $\varepsilon(u_\perp)$ coefficient which caused waves to be partially reflected as the increased normal speed of the fluid particles increased the repulsive force applied.

The second attempt involved modifying equation 3.29. The repulsive force correction due to the velocity of a fluid particle normal to the boundary, defined in equation 3.31, was removed. This was done as when a wave is approaching a boundary it will have a velocity normal to that boundary. If the repulsive force that the boundary applies is increased by the velocity of the fluid particle normal to the boundary then wave reflection will occur.

In this attempt the repulsive force applied was not modified by the velocity correction ($\varepsilon(u_\perp)$), as it was in the original code implementation. It was modified by the depth correction ($\varepsilon(z)$). Equation 3.31 was therefore no longer required. Equation 3.29 was modified to become:

$$\varepsilon(z, u_\perp) = H_1\big(1 + H_2 \times \varepsilon(z)\big) \tag{4.1}$$

For the plunger test case (where there is no inflow) a simpler modification has been used:

$$\varepsilon(z, u_\perp) = H_2 \times \varepsilon(z) \tag{4.2}$$

Where H_1 and H_2 are user-defined coefficients and $\varepsilon(z)$ is the fluid depth correction. The values of the coefficients were chosen based on freestream flow speed (if applicable) and particle resolution. If the fluid starts at rest then the coefficient H_2 is chosen so that particles will not pass through the non-reflecting open boundary unless there is a disturbance.

Different values of H_2 are tested for each time the spatial resolution or still water depth is changed. A short simulation is allowed to run to observe the behaviour of the particles close to the non-reflecting open boundary. In the zero inflow case the criteria for selecting the value of H_2 is that no particles should go through the non-reflecting open boundary. If particles do leave the domain then the value of H_2 was increased. If the particles remain in the domain then the value of H_2 was decreased. Using this process the critical value of H_2 can be found. A similar process can be used to set the value of H_1 if an inflow is present.

The fluid particles are removed from the domain if the particle is forced (by a disturbance) through the non-reflecting open boundary. If there is an initial flow speed then the coefficients are chosen to simulate a simple channel flow situation (with no waves or floating objects). In this case the number of particles leaving and entering the domain are equal, therefore maintaining a constant volume of fluid in the domain.

4.3 - Experiments

4.3.1 - Single Particle Test Case

The single particle test case in Crespo (2008) uses a single particle fired at different velocities towards a boundary. The boundary is a flat wall and the boundary uses dynamic particles. The single particle is given an initial velocity normal to the wall and gravity and viscosity are set to zero. The only force that acts on the particle is that from the boundary. The simulations described in Crespo (2008) use the dynamic boundary particle method. The test cases detailed in this section use the repulsive boundary particle method. This method has been chosen to compare the results between the two methodologies.

As some problems were found when experimenting with moving boundary particles this test case was also carried out using a moving boundary, again a flat wall. The test used a moving flat wall with constant velocity of 1 ms^{-1} throughout the simulation. The single particle was then fired towards the boundary. The total speed was calculated as the speed of the wall plus the initial speed of the single particle. The major input variables for these test cases are shown in table 4.1.

Kernel	Gaussian
Time-Stepping	Predictor-Corrector
Spatial Resolution	0.05m
Smoothing Distance, h	0.065m

Table 4.1: SPHysics inputs for single particle test case.

The tests were run with a selection of time steps to investigate the effect of varying the time step, especially on whether a smaller time step would prevent boundary penetration. The Gaussian kernel is used as the quintic (Wendland) kernel. which was determined to be superior in Macià *et al* (2011), had not been implemented in the version of SPHysics used in these test cases. The Predictor-Corrector scheme is used for time-stepping as the other time-stepping schemes had also not been implemented in the version of SPHysics used is these test cases. Figures 4.1 and 4.2 demonstrate the initial conditions for the test cases using the dynamic boundary particle method and repulsive boundary particle method respectively.

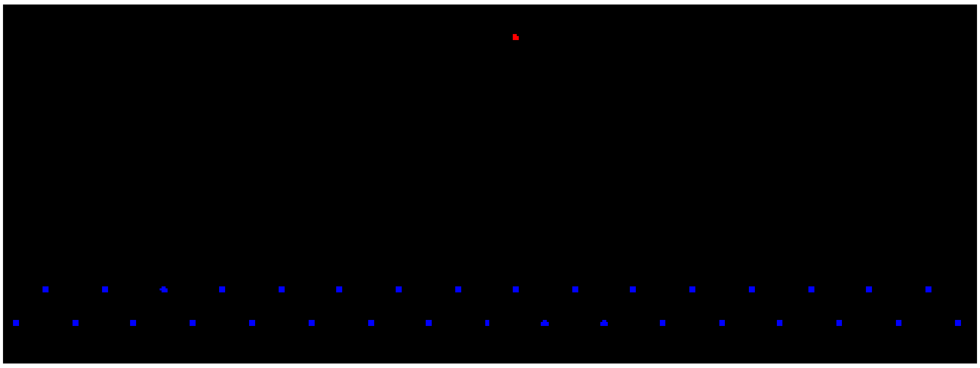

Figure 4.1: Single particle test case using dynamic boundary particles.

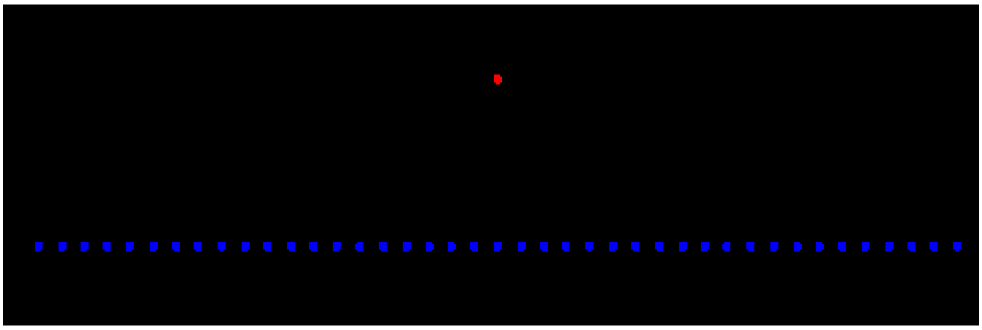

Figure 4.2: Single particle test case using repulsive force boundary particles.

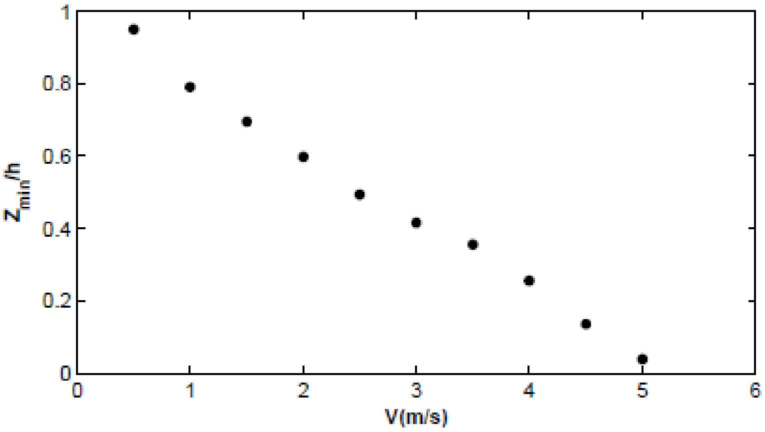

Figure 4.3: Zmin/h versus Initial Velocity, figure taken from Crespo (2008).

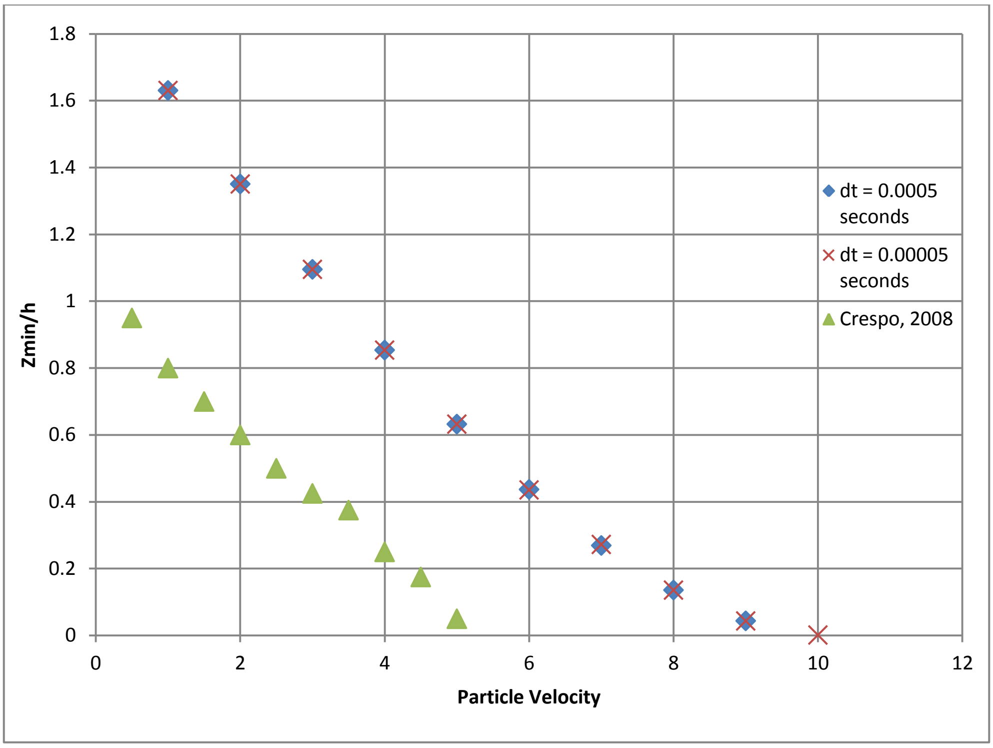

Figure 4.4: Z_{min}/h versus Initial Velocity when the boundary wall is stationary.

The graph shown in figure 4.3 shows the minimum distance (Z_{min}/h) of a single particle approaching a flat wall that is represented by dynamic boundary particles. The graph shows that as initial velocity increases the minimum distance decreases. Although it is not shown in figure 4.3 extrapolation of the data shows that above a certain initial velocity the particle will pass through the boundary. Figures 4.4 and 4.5 (where a stationary and moving repulsive particle boundary were used respectively) show the same trend as figure 4.3. This is as would be expected. However, whereas the trend in figure 4.3 is virtually straight the trends in figure 4.4 are curved. This is likely to be due to the very high repulsive force that will be applied to the fluid particle when the distance between the boundary and the fluid particle is very small as shown in equation 3.26.

Care has been taken to ensure that all possible variables that have been used in these test case are identical to those detailed in Crespo (2008). One conclusion that can be drawn from the results shown in figure 4.4 is that for a particle to penetrate a repulsive boundary it requires almost twice the initial velocity than would be required if a dynamic boundary is used. If this is indeed the case then the repulsive boundary method is superior to the dynamic as boundary penetration is a severe drawback with SPH.

The results shown in figure 4.4 show that if the initial velocity is high enough then the particle will penetrate the boundary. Each simulation was run with increasing initial velocity until the boundary particle passed through the boundary. In figure 4.4 the last point where dt = 0.0005 is where the initial velocity was 9 ms^{-1}; therefore since the initial velocity was increased by 1 ms^{-1} each time the graph implies that when the initial velocity was 10 ms^{-1} and dt = 0.0005 the particle passed through the boundary. However when dt = 0.00005 the final point was when the initial velocity was set to 10ms^{-1}. This occurred because the smaller time step allowed the repulsive boundary force to have enough effect to prevent penetration. Further simulations were carried out with dt = 0.000005 and dt = 0.0000005 but the results were the same as for dt = 0.00005.

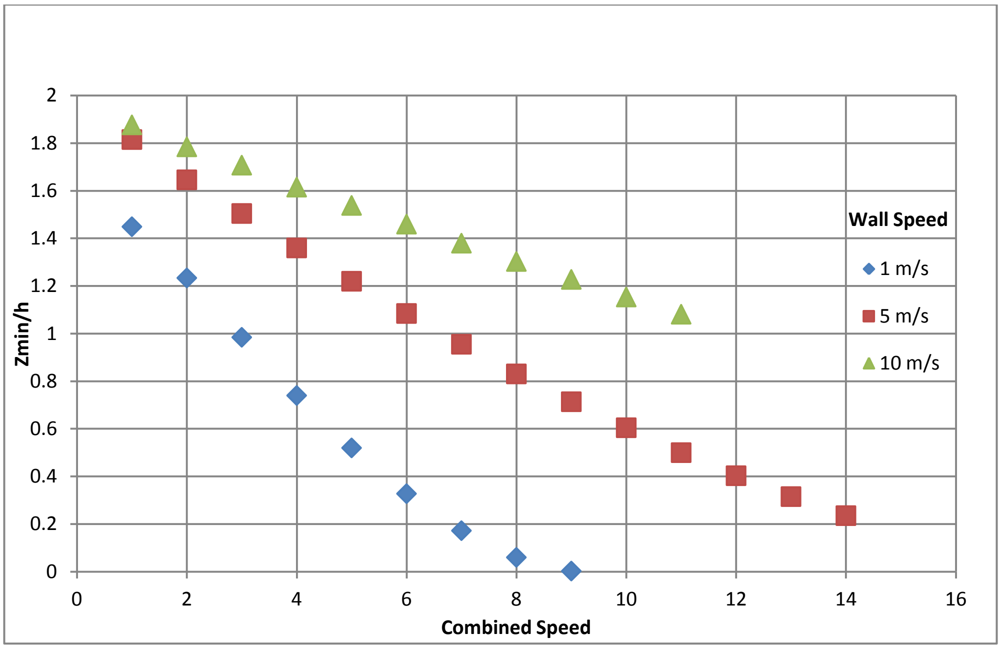

Figure 4.5: Z_{min}/h versus Combined Speed when the boundary wall is moving at 1, 5 and 10 ms^{-1}.

Figure 4.5 shows the results from simulations carried out using a moving boundary. Each point on the graph shows the minimum approach distance for each combined speed. When the wall is moving at 1 ms^{-1} there is very little difference between the two cases. However further simulations were carried out with time steps an order of magnitude smaller in the same way as was done with the stationary boundary case. In the case of the moving boundary there was no effect on the maximum initial velocity before penetration. This simulation was carried out because of problems found when using moving boundaries in simulations with large numbers of fluid particles. Although the difference between the wall moving at 1 ms^{-1} and stationary boundary cases was smaller than expected it still highlights a potential flaw in the moving boundary method.

Further simulations were carried out where the moving boundary was moving at 5 and 10 ms^{-1}. Both simulations allowed a greater combined speed before boundary penetration although in each case Z_{min}/h was greater than for the 1 ms^{-1} case. The 5 ms^{-1} case follows a very similar pattern to the 1 ms^{-1} case. The maximum initial particle velocity was 9 ms^{-1} for the 5 ms^{-1} case and 8 ms^{-1} for the 1 ms^{-1} case. However the 10 ms^{-1} case was very different, for the maximum initial particle velocity of 1 ms^{-1}. This is unexpected as a faster moving wall should exert a greater repulsive force than a slower moving one, as described by equation 3.31. Perhaps a possible cause of this problem may be the time step which may not be small enough to allow the repulsive force time to repel the particle.

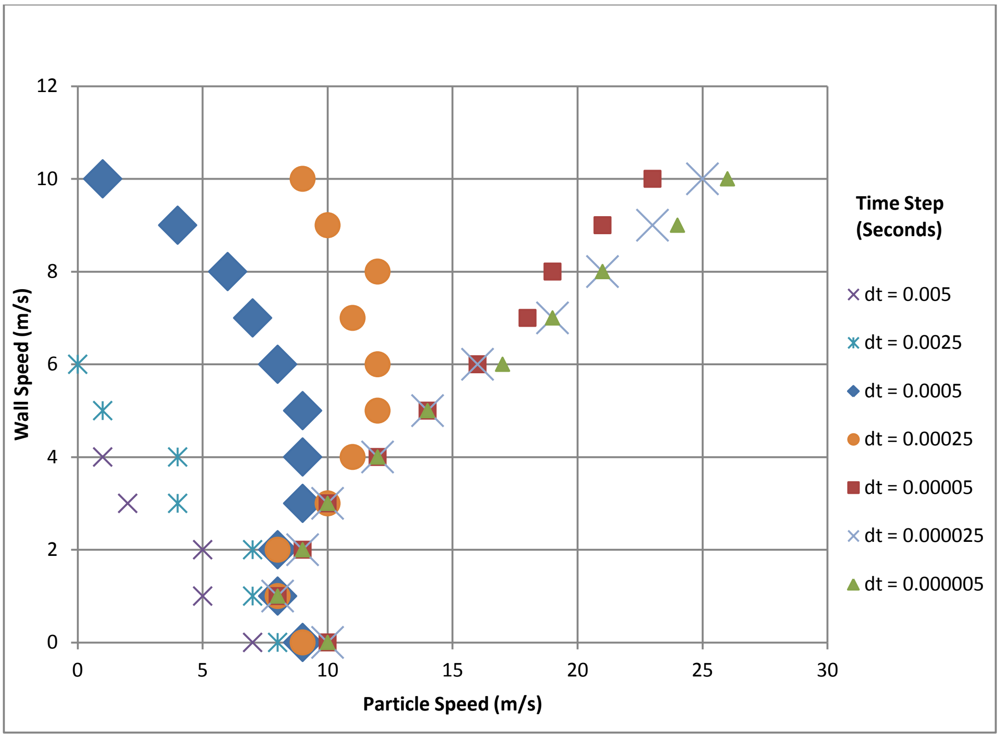

Figure 4.6: The relationship between particle speeds, wall speeds and time step.

Figure 4.6 shows the relationship between particle speeds, wall speeds and time step. Each point on the graph shows the maximum initial particle velocity for a given wall speed and time step. Any initial particle velocity lower than the value at any point on the graph the particle will not penetrate the boundary at that wall speed and time step.

It can clearly be seen that there are three distinct trends on the graph. Firstly, when a time step of 0.005 or 0.0025 is used the maximum initial particle velocity is much too low to capture the behaviour correctly. The second trend refers to time steps of 0.0005 or 0.00025 at low wall speeds. The results seem correct but when the wall speed is increased the maximum initial particle velocity decreases. As the repulsive force applied by a boundary increases with wall speed this suggests that the behaviour is not correct because of a too coarse time step. The third trend is shown by time steps 0.00005, 0.000025 and 0.000005. The time step is sufficiently small to allow the initial particle velocity to increase as wall speed increases. This is the behaviour that is to be expected given the method used to adjust the repulsive force applied by a moving boundary.

4.3.2 – 2D Plunger

A series of 2D simulations were carried out to replicate the simulations of the wave tank with plunger test in Yim *et al* (2008). The test case involved dropping a rectangular plunger into the left-hand end of a wave tank. The experiments carried out in Yim *et al* (2008) used a wave tank of length 16m. This length was used so that the waves generated did not have enough time to travel the length of the tank and back. The simulations in Yim *et al* (2008) (both Reynolds-Averaged Navier-Stokes (RANS) and SPH) used a domain of length 2m with a non-reflecting boundary at the right-hand end.

The simulations carried out in SPHysics idealised the plunger as a sinkable floating body of high mass. The motion of the plunger was limited to motion in the z-axis This means that the plunger sinks straight downwards and cannot pitch. The case that was studied was the L10H10P3 case (10cm long wedge, 10cm water depth, wedge starting position 3cm above still water level). Both time step (dt) and spatial resolution (dx, dz) studies were carried out. The wave height is measured at x = 0.4m and x = 0.85m. The main variables that were varied throughout the tests were: length of domain, spatial resolution (in all cases dx = dz) and time step.

To measure the height of the free surface at a given point a new wave height routine had to be added to the SPHysics code. This routine searches for fluid particles on either side of the measuring point up to a distance of dx. On either side of the measuring point the fluid particle with the greatest height (i.e. the greatest value of z) is found. An imaginary line is drawn between these two particles. Where this line crosses the measuring point the value of wave height is measured. This method is outlined in figure 4.7.

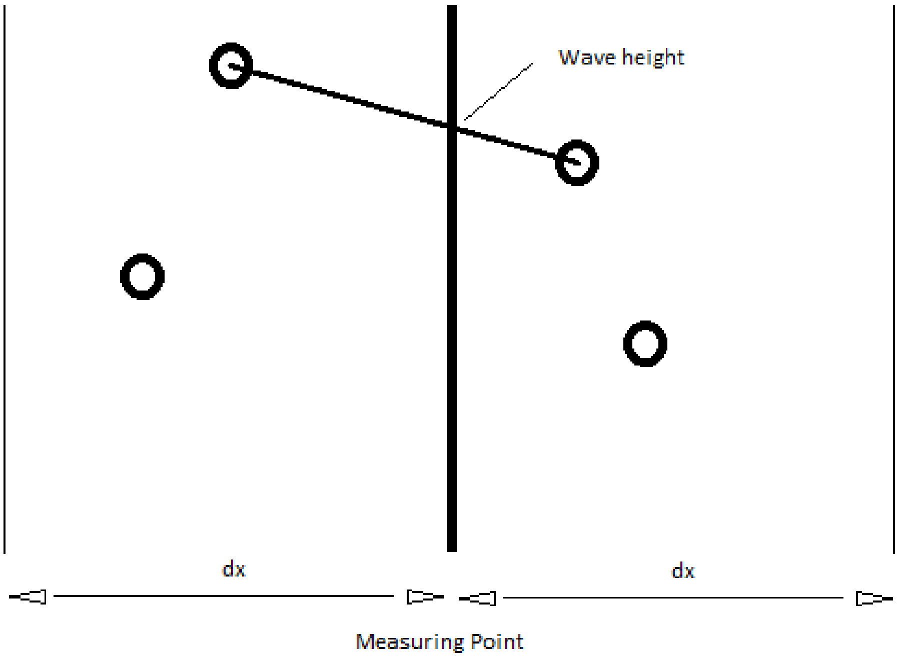

Figure 4.7: Illustration of the wave height measuring method. Black circles represent fluid particles.

Case Number	Domain Length (m)	Spatial Resolution (m)	Time Step (s)
4A	1	0.005	0.00005
4B	1	0.0025	0.00005
4C	1	0.0025	0.000025
4D	1	0.0025	0.00001
4E	2	0.005	0.00005
4F	2	0.0025	0.00005

Table 4.2: Plunger test case variables (Each case simulates 3 seconds of real time.

Kernel	Quadratic
Time-Stepping	Predictor-Corrector
Viscosity Treatment	Full viscosity method
Spatial Resolution	0.005m / 0.0025m
Smoothing Distance, h	0.065m / 0.0325m

Table 4.3: SPHysics inputs for the plunger test case.

The Quadratic kernel was used as it is suited to simulations where severe particle compression is expected. The kernel prevents particle clustering which would occur as the plunger compressed the particles underneath it. The Predictor-Corrector time-stepping scheme was used as the other time-stepping schemes were not implemented in the version of SPHysics used for these test cases. The full viscosity method was used as it offers the most accurate viscosity scheme implemented in SPHysics and the viscosity model is important in this highly turbulent simulation.

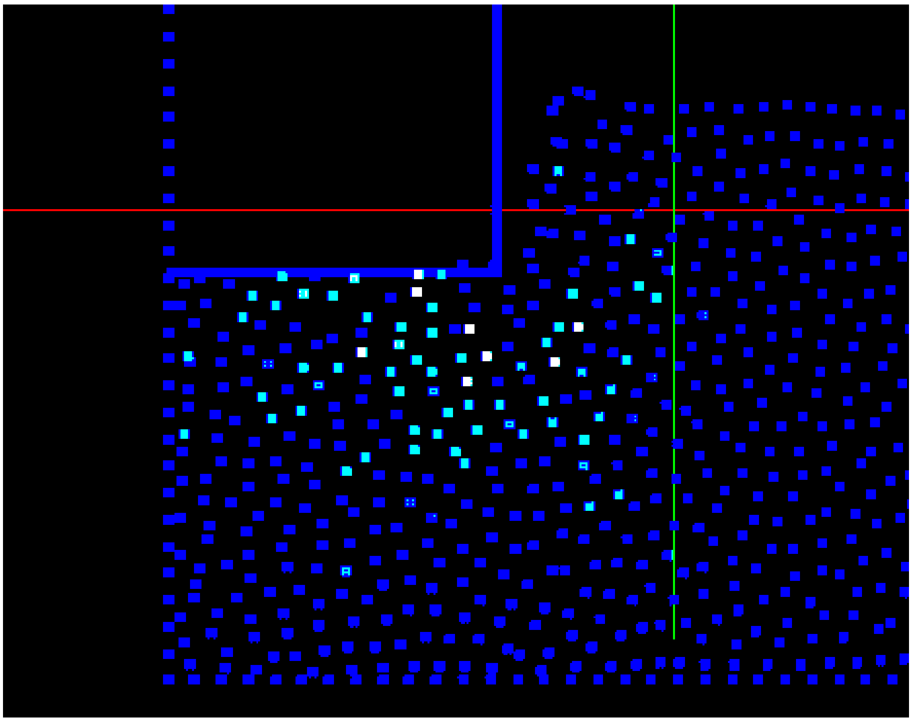

Figure 4.8: Close-up of the bottom-left corner (first 0.2m shown) of the tank at t = 1.00 seconds.

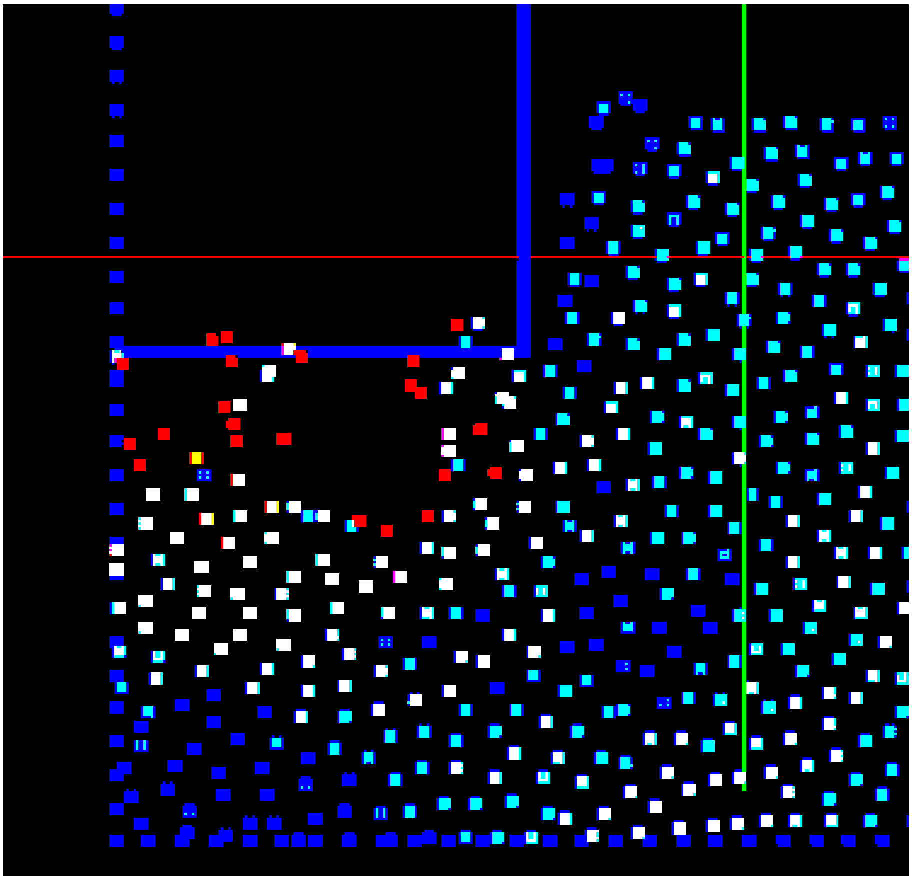

Figure 4.9: Close-up of the bottom-left corner (first 0.2m shown) of the tank at t = 1.02 seconds.

Figures 4.8 and 4.9 show snapshots of simulations carried out in an attempt to repeat the simulations in Yim *et al* (2008). Four problems have been encountered during the simulation process:

- The fluid in the tank does not remain stationary at the beginning of the simulation, a problem discussed in Souto-Iglesias *et al* (2006).
- The plunger walls are penetrated by some fluid particles.
- When the plunger reaches the bottom of the tank not all of the fluid particles have moved out of the way and are forced out of the computational domain.
- During some simulations the fluid is seen to explode and then rapidly collapse.

The first problem can be overcome by either running the simulation until the fluid has reached a state of equilibrium or by refining the initial conditions so that the problem does not arise. The second problem was the reason that the single particle test cases were investigated. However, during the multi-particle simulations the particles were able to penetrate the moving boundary far more easily than the stationary boundaries; a result not shown in the single particle test cases in the previous section. The single particle test cases did not simulate the forces exerted on fluid particles by other fluid particles. Therefore the unphysical behaviour can be attributed to the presence of other fluid particles.

It is believed that if the simulation was carried out in 3D then the third problem would be alleviated somewhat although not completely. Another possible solution is to impose a density limit, if a particle were to have a density above this limit it would be removed from the domain. When a more thorough set of simulations has been carried out the effect of this problem on the results can be analysed and the need for a solution be determined.

The fourth problem is a curious effect that only occurs in some simulations. Figure 4.8 shows a screenshot of the part of the domain where the plunger impacts on the fluid at t = 1.00 seconds. The colour of the particles shows the speed of each particle (blue is slow and red is high speed). Figure 4.9 shows the same area at t = 1.02 seconds. It can clearly be seen that the particles which were relatively ordered have suddenly become very disordered. When sequences of screenshots are viewed the fluid appears to explode and then collapse very rapidly. In some situations the process repeats. No mention of this sort of behaviour is made in Yim *et al* (2008). A possible cause of these explosions is a particle moving into very close proximity to the repulsive boundary and therefore being accelerated at a huge rate. If this is the case then a possible solution to this problem is to implement a restriction on the maximum speed of a particle. However, this would be computationally expensive and would not be a realistic representation of physics.

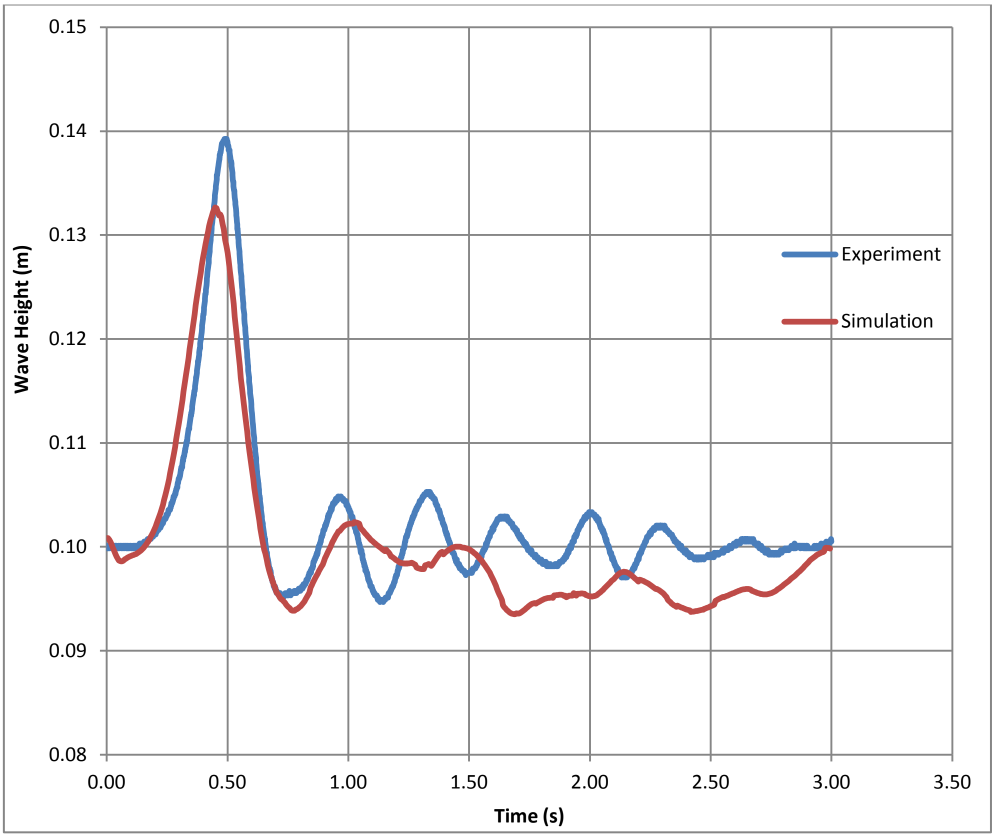

Figure 4.10: Case 4A, x = 0.4m.

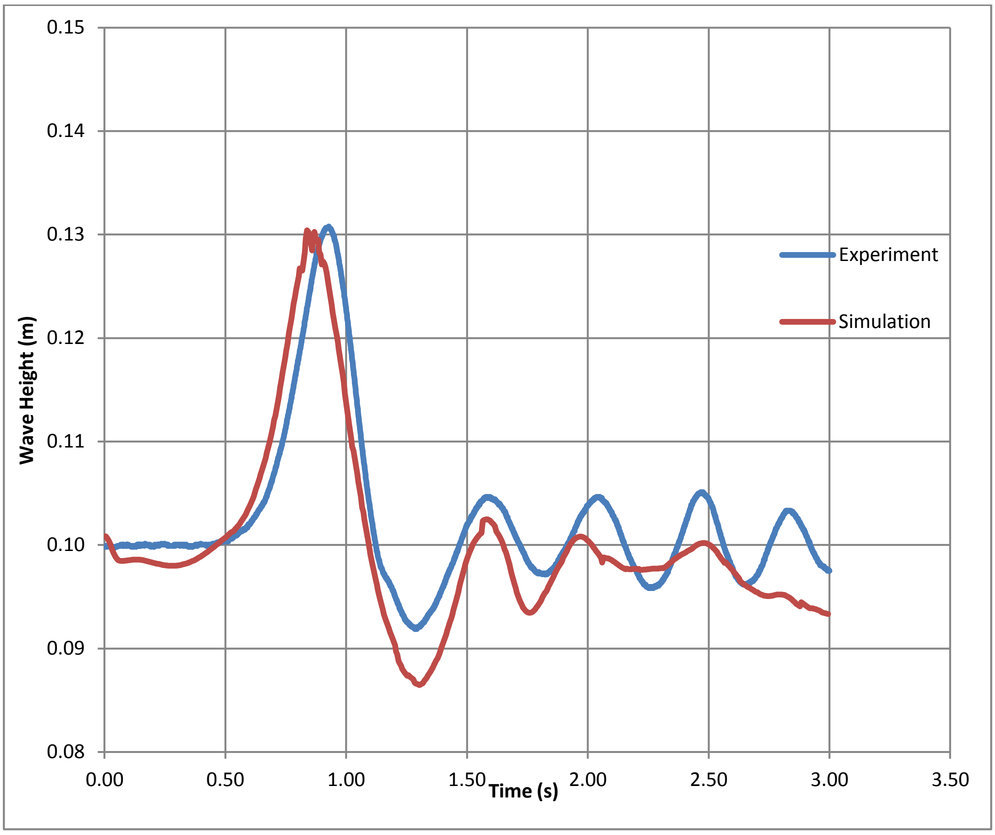

Figure 4.11: Case 4A, x = 0.85m.

Having created a viable non-reflecting open boundary a more extensive series of simulations were conducted. These are cases 4A – 4F as detailed in table 4.2. Figures 4.10 and 4.11 show the lower resolution 1 metre test case At both wave measuring points the shape of the initial wave is very similar to that of the experimental data. At x = 0.4m (figure 4.10) after the initial wave has passed the following waves seem to be over damped. They also have lower frequency. However, at x = 0.85m (figure 4.11) the subsequent waves seem better defined with both amplitude and frequency being closer to the experimental data.

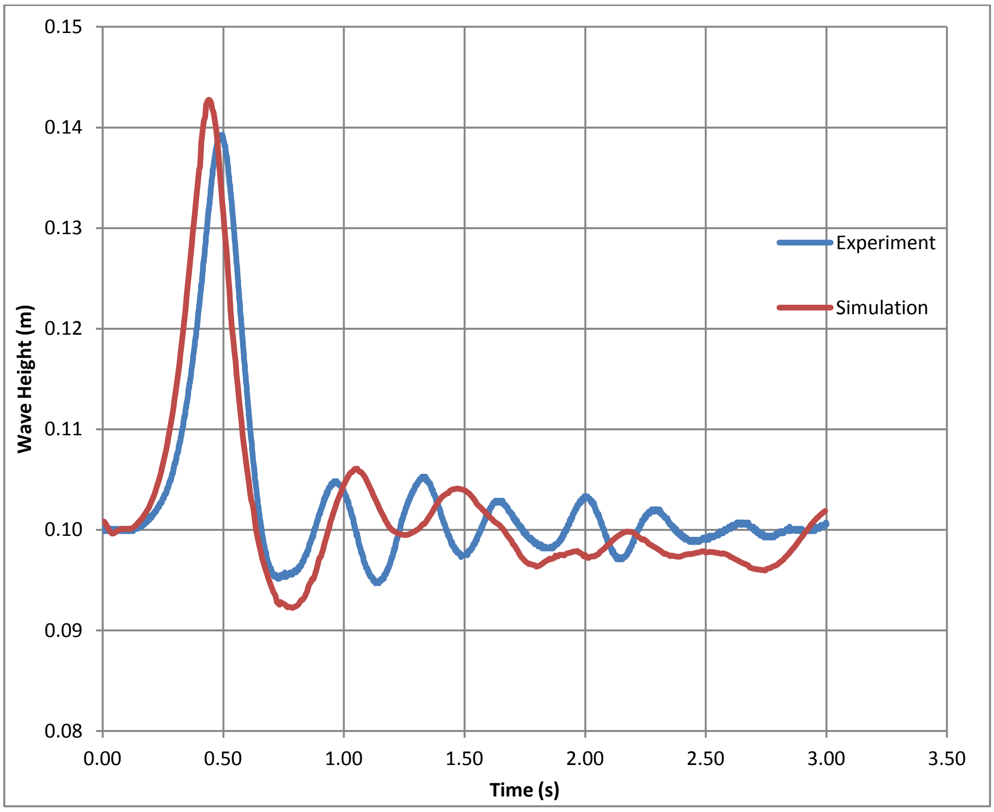

Figure 4.12: Case 4B, x = 0.4m.

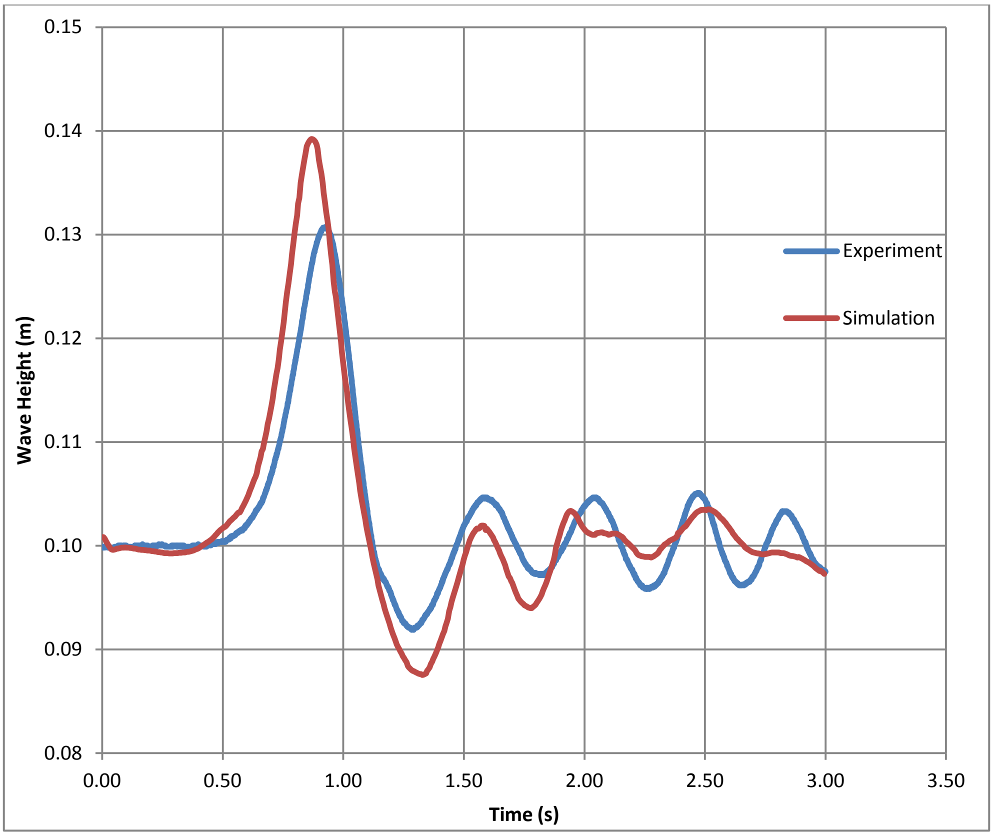

Figure 4.13: Case 4B, x = 0.85m.

Figures 4.12 and 4.13 show the higher spatial resolution 1 metre test case. Compared to the previous case the x = 0.4m results (figure 4.12) shows a closer agreement with the experimental data. As before the x = 0.85m (figure 4.13) results are very close to the experimental data. The experimental data show a drop in the height of the initial wave of about 0.01m between x = 0.4m (figure 4.12) and x = 0.85m (figure 4.13). However, in most of the cases the simulations show a much smaller difference in initial wave height between the two measuring points.

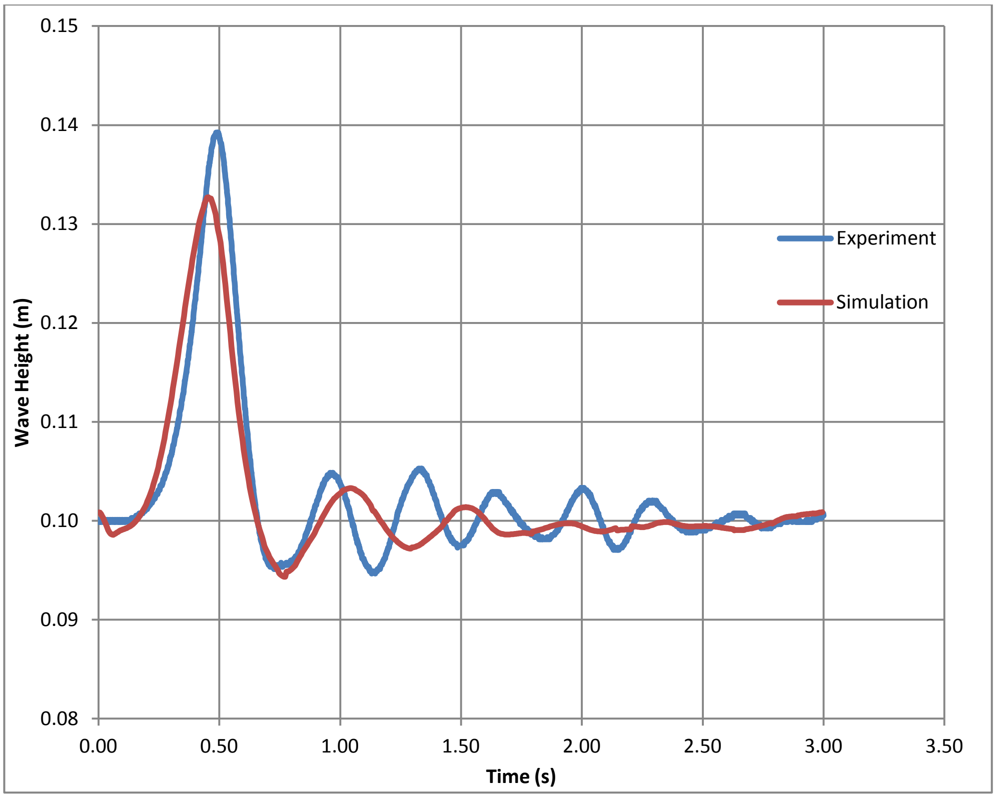

Figure 4.14: Case 4E, x = 0.4m.

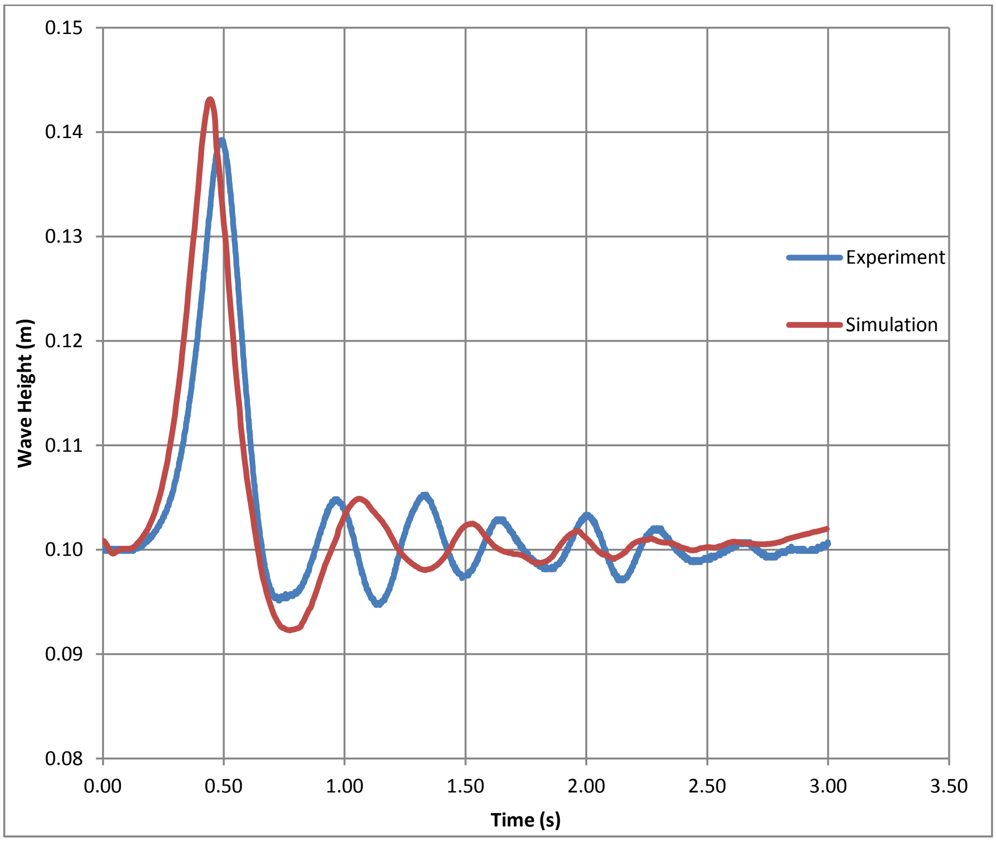

Figure 4.15: Case 4E, x = 0.85m.

Figures 4.14 and 4.15 show the lower spatial resolution 2 metre test case. In these figures the simulation results show a similar trend to that seen in the low resolution 1 metre case. The first wave at both measuring points is lower than in the experiment. However the magnitude of the drop in initial wave height between x = 0.4m (figure 4.14) and x = 0.85m (figure 4.15) is similar in this simulation as it is in the experiment.

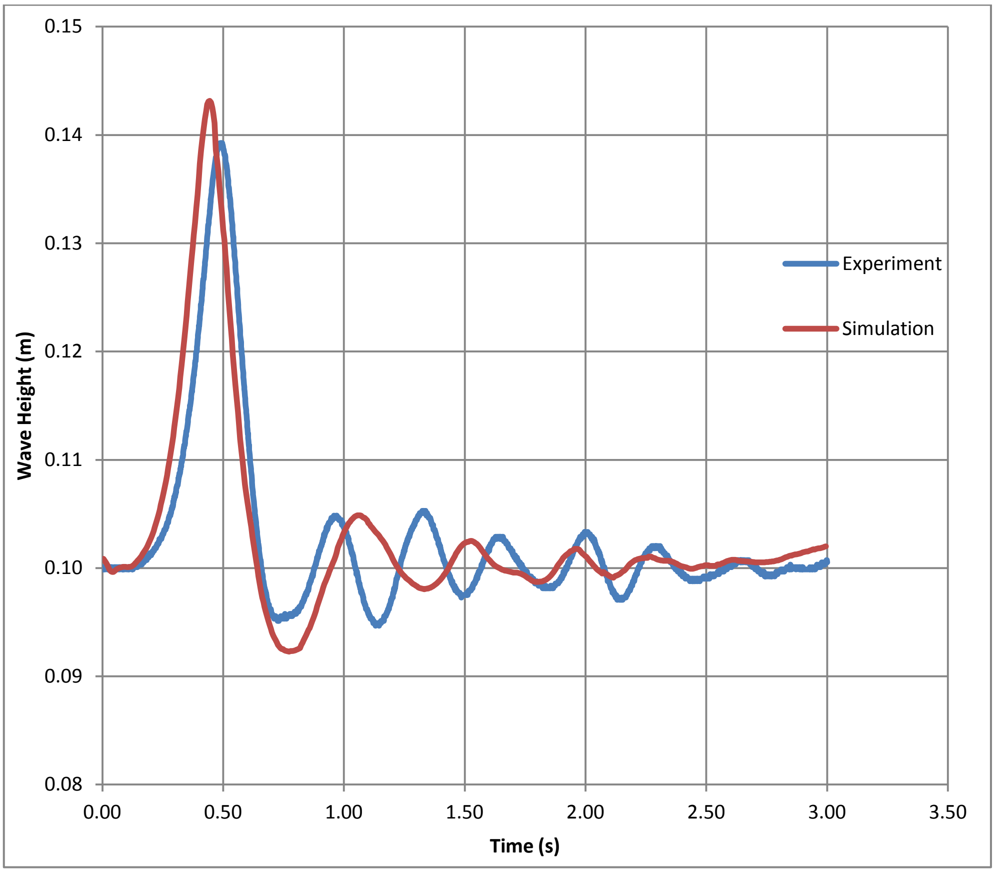

Figure 4.16: Case 4F, x = 0.4m.

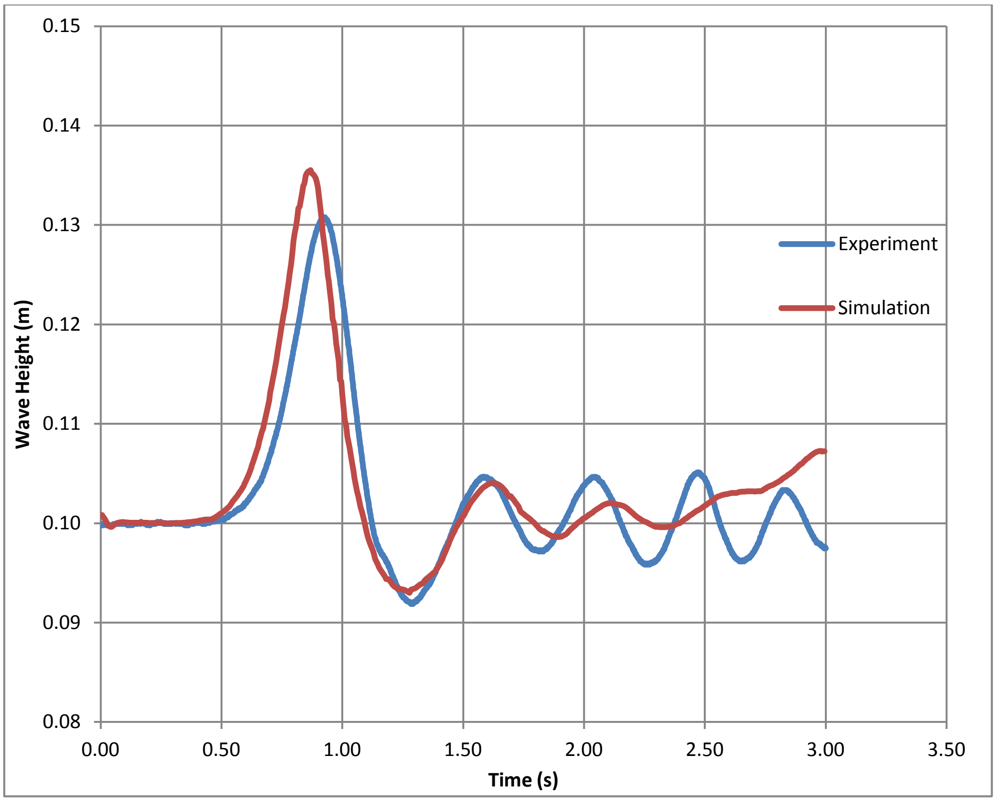

Figure 4.17: Case 4F, x = 0.85m.

Figures 4.16 and 4.17 show the higher spatial resolution 2 metre test case and again the results are similar to those of the experiment. However in contrast to the previous test case the first wave height is over-predicted although again the magnitude of the drop in initial wave height between the two measuring points is comparable to that found in the experimental data.

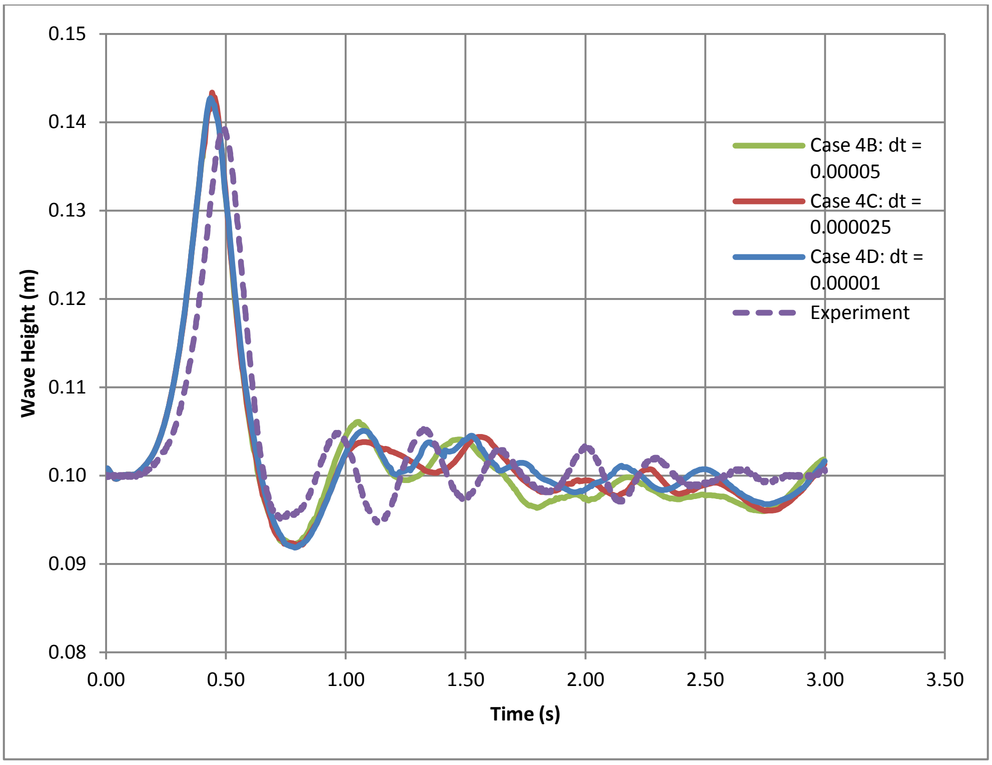

Figure 4.18: Time step comparison, x = 0.4m.

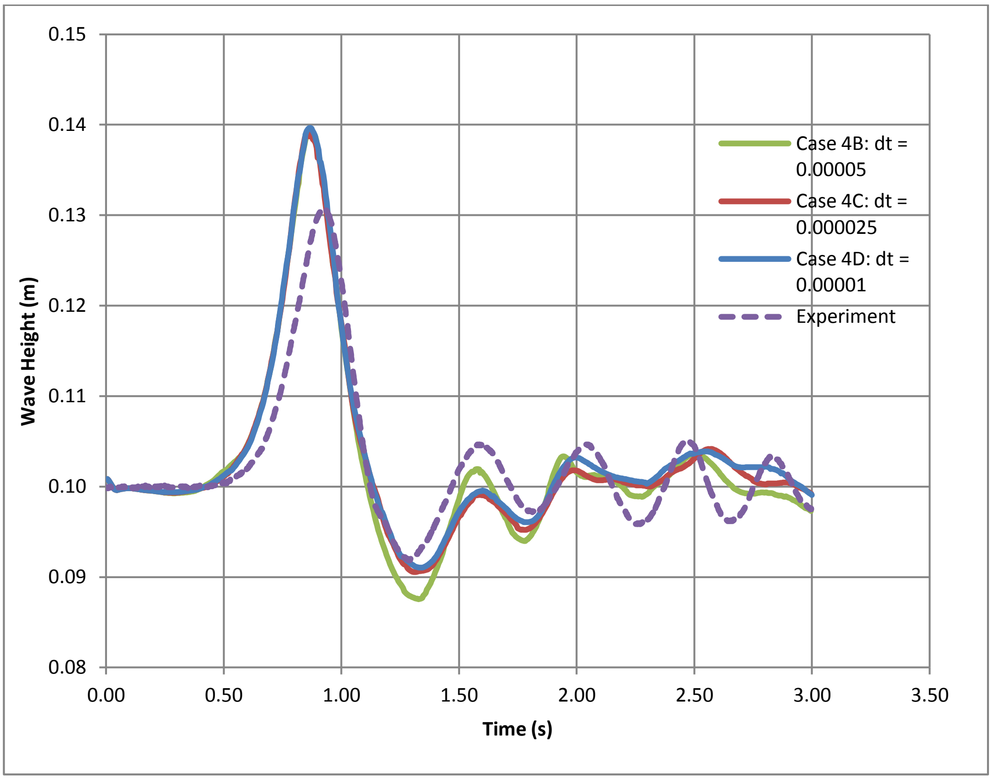

Figure 4.19: Time step comparison, x = 0.85m.

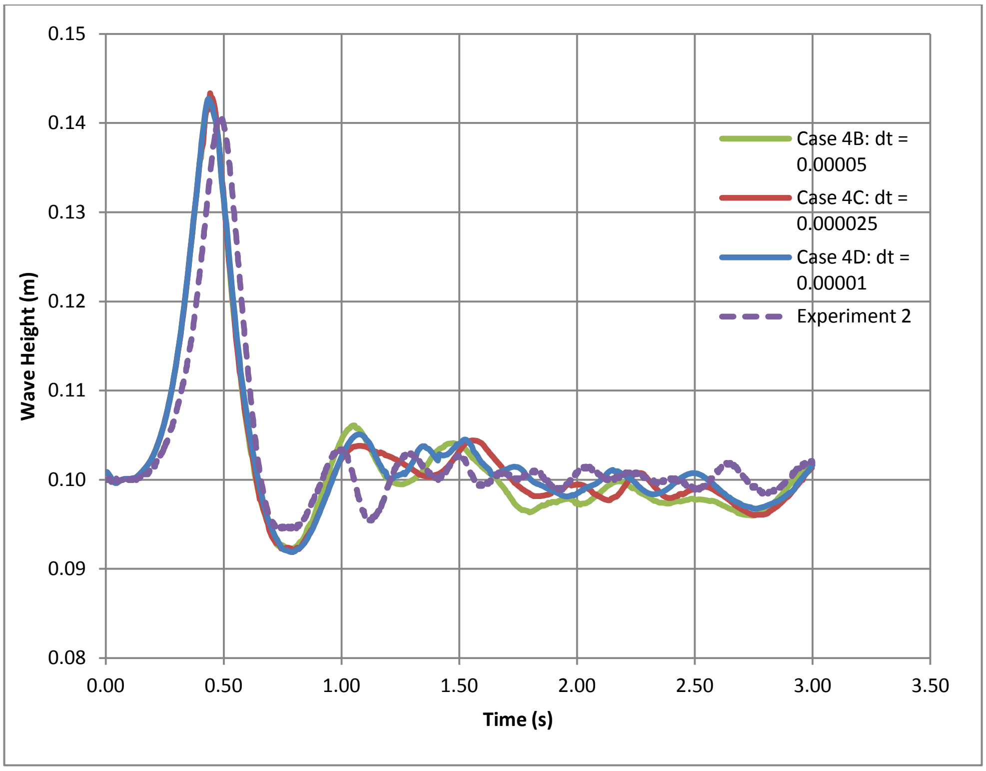

Figure 4.20: Time step comparison (with experimental data 2), x = 0.4m.

Figures 4.18, 4.19 and 4.20 show the results of a time step comparison. Figures 4.18 and 4.19 use the first set of experimental data in Yim *et al* (2008). Figure 4.20 shows the second set of experimental data. Ignoring the comparison of the two sets of experimental data (which is shown in figures 4.25 and 4.26) and concentrating on the results of the time step comparison it can be seen that there are no major differences between the different time steps. It should be noted that larger time steps were tried. However, none of the runs were completed due to numerical instability. Smaller time steps resulted in excessive run times. In this case these results point toward the requirement to find the largest time step that is stable. Smaller time steps offer no benefit in terms of accuracy and are computationally expensive.

One feature that is common to all of the test cases is that the first waves generated show good accuracy when compared to the experimental results. However the subsequent waves show an increasing amount of damping. The frequency of the waves also varies; a fact that is probably caused by wave reflection in way of the open boundary. This is shown in the difference between the 1m and 2m tank length test cases. It is clear that the wave height in the 1m tank length simulations begins to deviate from the experimental results earlier than in the 2m tank length simulations. This may be attributed to wave reflection. Reflected waves have less distance to travel before they interfere with the wave height in way of the measuring points in the 1m tank length simulations. Therefore they are able to influence the results earlier. This effect can be seen when the results of test case 4A is compared to those of test case 4E. Similar comparisons can be made between test cases 4B and 4F.

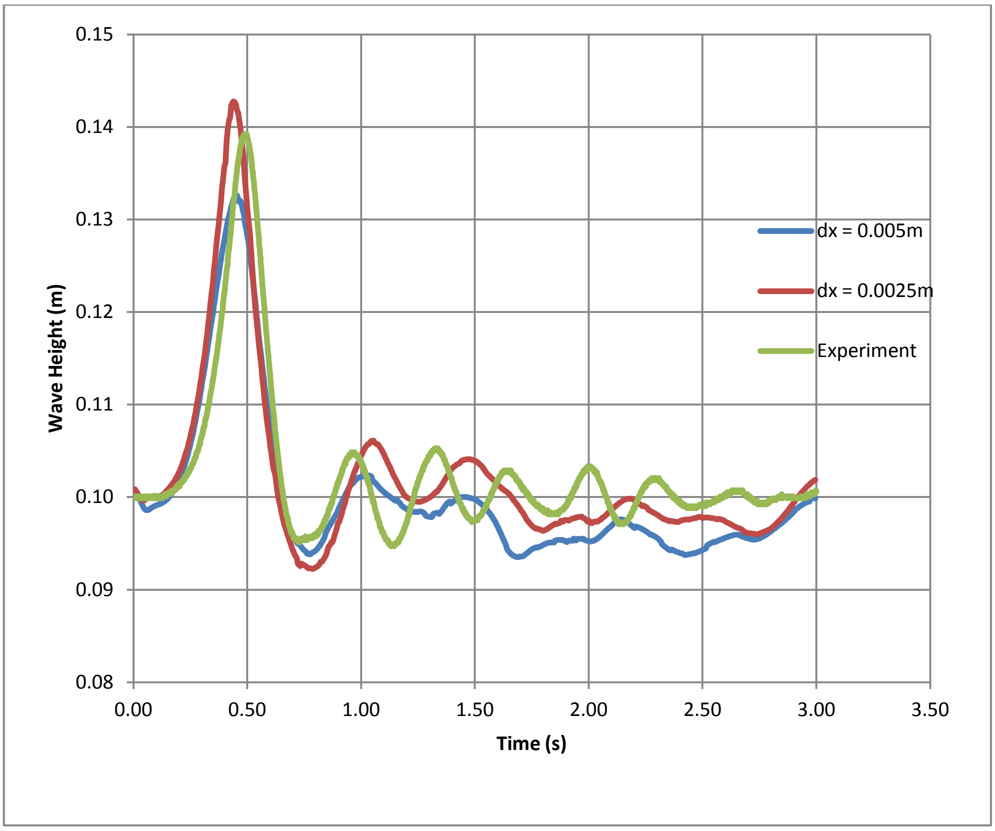

Figure 4.21: Spatial resolution comparison, length = 1m, x = 0.4m.

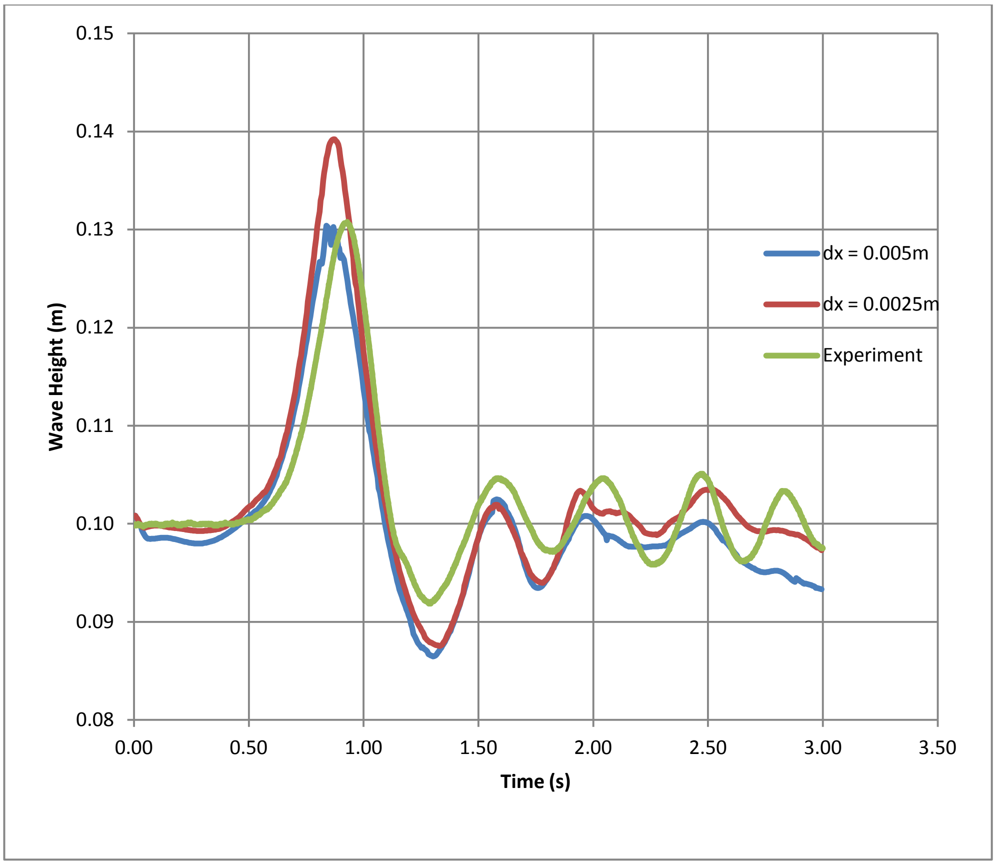

Figure 4.22: Spatial resolution comparison, length = 1m, x = 0.85m.

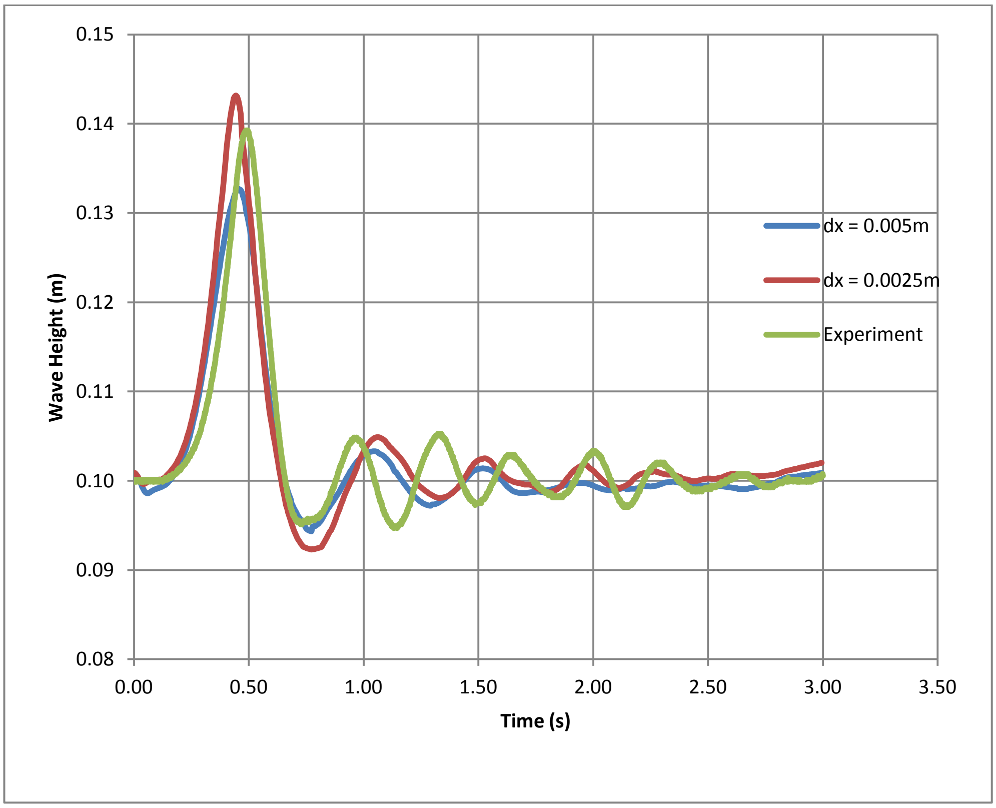

Figure 4.23: Spatial resolution comparison, length = 2m, x = 0.4m.

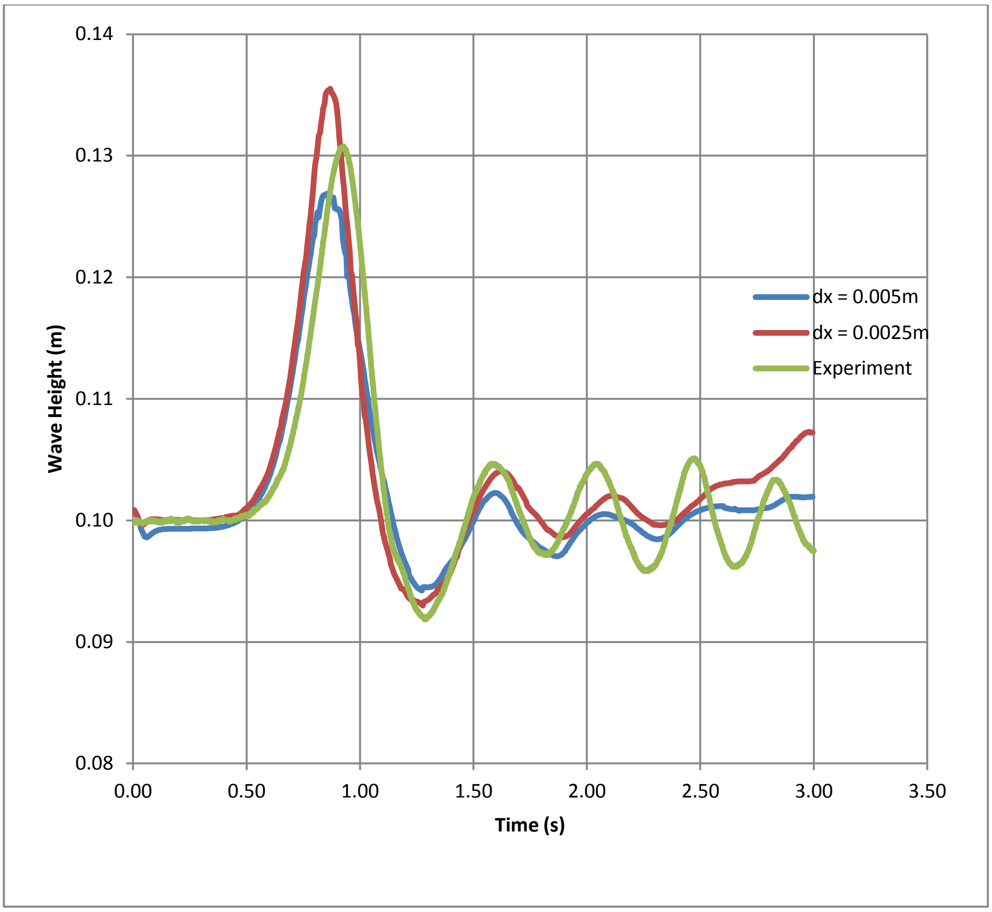

Figure 4.24: Spatial resolution comparison, length = 2m, x = 0.85m.

Figures 4.21, 4.22, 4.23 and 4.24 show the results of a spatial resolution study. A coarse spatial resolution results in the wave height being lower than the experimental data. In contrast the results when using a fine spatial resolution show better agreement with the experimental data in terms of wave height. Both cases show over-damping of the waves, especially as time passes. However the finer resolution test case show less over-damping than the coarser resolution case.

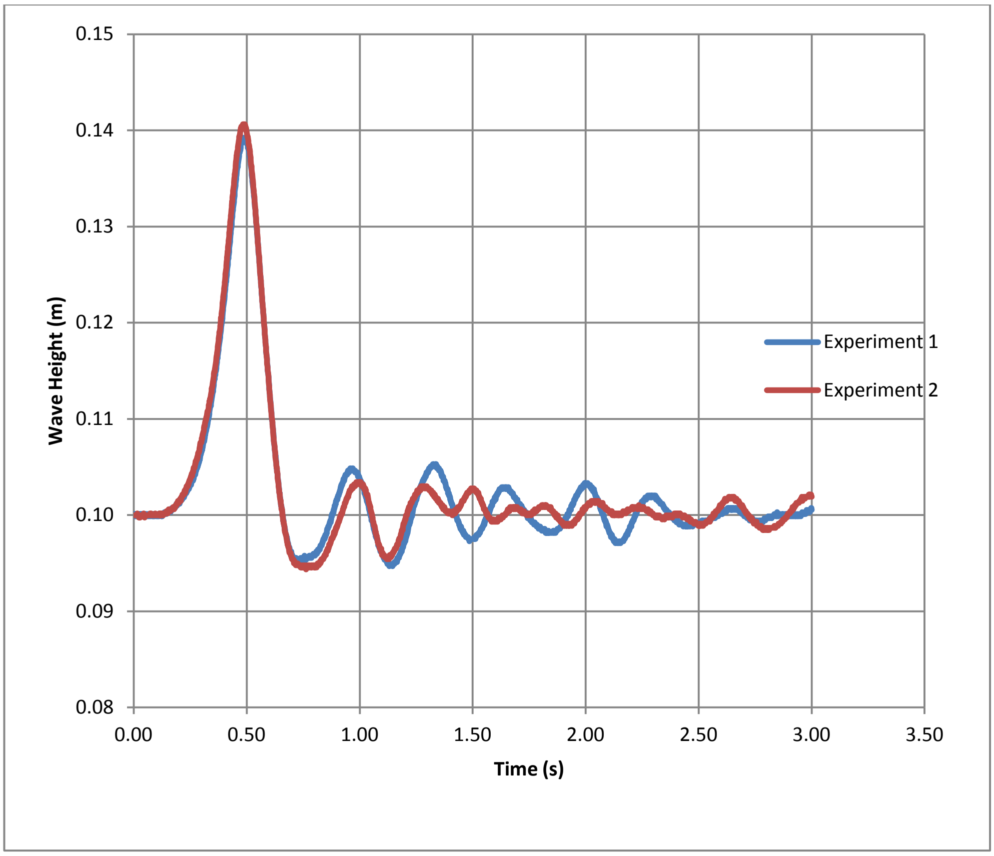

Figure 4.25: Experimental data comparison, x = 0.4m.

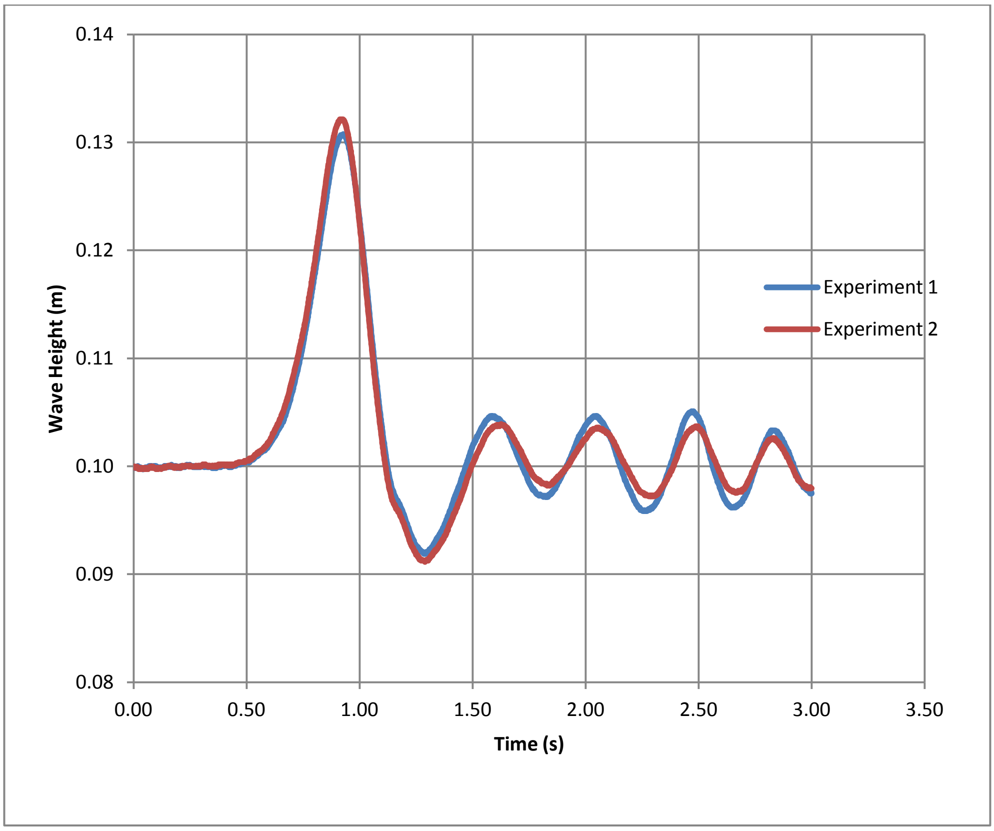

Figure 4.26: Experimental data comparison, x = 0.85m.

All but one of the figures thus far discussed have used the results from the first set of experiment data as the benchmark (the exception is figure 4.20). Figures 4.25 and 4.26 show a direct comparison between these two sets of experimental data. Figure 4.26 (measuring wave height at x = 0.85m) shows very little difference between the two data sets. However, the difference between the results in figure 4.25 is much greater. The wave amplitude and frequency of the second set of results are very much different after the second wave.

The peculiar disparity between the two data sets at x = 0.4m and x = 0.85m is very odd as the waves passing through x = 0.4m are very different but by the time they have arrived at x = 0.85m they are very similar. One explanation for this may be that x = 0.4m is very much closer to the impact area. The complex flow created by this violent event causes variable flow patterns. Those lead to a much greater variation in the waves at x = 0.4m. However, each time the simulation or experiment is run the end result is the same. As a result the plunger displaces a relatively fixed volume of water which then travels down the tank.

4.4 - Conclusions

The single particle test cases detailed in this chapter demonstrate that the solid boundaries modelled in SPHysics are not impermeable in some cases. The test cases are based upon the single particle test cases presented by Crespo (2008). However, a repulsive boundary method is used instead of the dynamic boundary method simulated in Crespo (2008). This result lead to the use of the Lennard-Jones potential equation in the repulsive boundary methodology shown in equation 3.33. A comparison of the results presented in Crespo (2008) and the simulation results show that the repulsive boundary method is superior to the dynamic method as far as preventing boundary penetration is concerned.

The plunger test cases were primarily devised to test the effectiveness of the novel open boundary condition. A number of problems were encountered in initial simulation attempts and solutions to these problems have been proposed. The simulation results show reasonable accuracy when compared to the first set of experimental results in Yim *et al* (2008).

The simulation results become less accurate as the simulation progresses in time. The discrepancy is caused by waves being reflected off the open boundary in an unphysical manner, as proved by the comparison of the 1m and 2m wave tank results. This shows that the open boundary condition has failed to meet one of the main objectives of a non-reflecting open boundary. The results of the time resolution study show that the simulation results are not sensitive to the time resolution chosen. The exception to this is if the time step chosen is too coarse which will cause numerical instability. The results of the spatial resolution study show that using a finer spatial resolution will result in more accurate results when compared to experimental data both in terms of wave height and also wave damping.

The advantage of this method is that it is very simple to implement and requires little extra computational resources. Overall, the wave reflection would appear to be too great to ignore and therefore a more suitable method must be developed.

Chapter 5

Airy Wave Theory Wave Maker and Wave Propagation

5.1 - Introduction

To accurately simulate the motion of a ship it is essential that the physics of the waves that cause the ship motion are modelled correctly. To achieve this a new wave maker based upon the Airy wave theory, described in Airy (1841), is proposed. The effectiveness of the wave maker in generating waves that are accurate when compared to Airy wave theory in way of their propagation is also discussed.

5.2 - Methodology

The Airy wave theory was developed by George Biddell Airy. It describes the propagation of surface gravity waves in a fluid with uniform mean depth. The theory assumes that the flow is inviscid, incompressible and irrotational Clearly this is not the case with the flow modelled by SPHysics as SPHysics has a viscosity model and uses a weakly compressible formulation. However the Airy wave theory is often successfully used to estimate wave characteristics and has been selected in this case for its simplicity.

The outputs of the Airy wave theory that are used by the wave maker are the x (horizontal) and z (vertical) axis velocities. To define an Airy wave the wavelength (λ), wave amplitude (a) and the mean depth of the fluid (d) must be prescribed. The wavelength is used to calculate the angular wavenumber (k):

$$k = \frac{2\pi}{\lambda} \tag{5.1}$$

The observed angular frequency (ω) of a wave is given by:

$$\omega = \sqrt{g \times d \times \tanh(k \times d)} \tag{5.2}$$

Where g is the acceleration due to gravity. The Airy wave theory is capable of simulating waves where there is a mean flow, that is uniform over depth, in the x direction. The observed angular frequency uses an Earth-fixed frame of reference. A non-zero mean flow speed will introduce a Doppler shift so an angular frequency which uses a frame of reference that moves with the mean flow is required. This is known as the intrinsic angular frequency defined as:

$$\sigma = \omega - \boldsymbol{k} \cdot \boldsymbol{U} \tag{5.3}$$

k is the wavenumber vector and ***U*** is the mean flow speed. The wave phase (θ) is given by:

$$\theta = \boldsymbol{k} \cdot \boldsymbol{x} - \omega \times t \tag{5.4}$$

Where $\boldsymbol{x}$ is the x axis position of the particle and t is the time elapsed. The horizontal and vertical velocities of a particle can now be calculated:

$$u_x = \sigma \times a \times \frac{\cosh(k \times (z+d))}{\sinh(k \times d)} \times \cos\theta \tag{5.5}$$

$$u_z = \sigma \times a \times \frac{\sinh(k \times (z+d))}{\sinh(k \times d)} \times \sin\theta \tag{5.6}$$

Where z is the vertical position of the particle where the mean surface is the origin and downwards is positive (note that this is different to the SPHysics axis system). Using equations 5.5 and 5.6 the velocity of a particle, whose position is known, according to the Airy wave theory can be calculated.

To utilise the Airy wave theory for wave generation, the SPH domain has been split into two separate domains. The first domain is the wave maker domain where the velocities of particles are determined by equations 5.5. and 5.6. The second domain is the main domain where the particles follow standard SPH equations. Determining which domain a particle belongs is based upon the particles' position. Any particle which crosses the boundary between the two domains becomes a part of the domain into which it has moved.

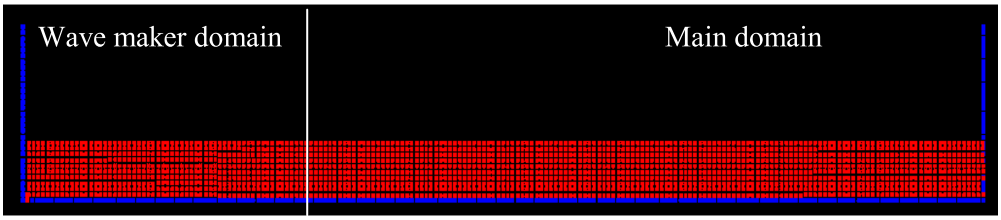

Figure 5.1: Layout of the two domains.

The particles in the wave maker domain follow all of the standard SPH equations with the exception of the velocity equations (which are used to calculate the particles' new position in the time stepping equations). This means that the particles within the wave maker domain have all the properties of normal SPH particles. In this way when a wave maker domain particle moves into the main SPH domain it has values for all the necessary properties for use in the standard SPH equations. This means that a particle may move across the boundary freely in either direction. It is important that the length of the wave maker domain is sufficiently large so that any particle within the main domain has complete kernel support. Therefore the wave maker domain must be at least length 2h.

In practice there is one more factor that needs to be considered when choosing the length of the wave maker domain. That is the motion described by the particles which becomes elliptical as particles move horizontally. It is possible that all of the particles in the wave maker domain may move out of the wave maker domain into the main domain (they will of course eventually return). This case must be avoided firstly because the particles at the edge of the main domain will have incomplete particle support and secondly because if there are no particles in the wave maker domain no waves will be generated. The horizontal motion of a particle (ξ_x) described by the Airy wave theory is given by:

$$\xi_x = a \times \frac{\cosh(k \times (z+d))}{\sinh(k \times d)} \times \sin\theta \tag{5.7}$$

The maximum horizontal particle motion can then be summed with the value of Stokes' drift (equation 5.9) to calculate the minimum possible length of the wave maker domain for each simulation.

As the motion of the wave maker particles follow the Airy wave equations the wave maker particles will describe the motion of an Airy wave (dependant on the mean depth, wavelength and wave amplitude chosen). The particles in the wave maker domain are somewhat similar to the boundary particles in a conventional fixed motion wave maker; whilst in the wave maker domain the particles follow a prescribed motion. This means that the particles at the edge of the wave maker domain closest to the main domain will generate waves in the main domain. The main difference between the two methods is that the wave maker particles can become standard SPH fluid particles if they cross the boundary between the two domains.

Two further values can be calculated using the Airy wave theory. These are the wave phase speed (c_p) and Stokes' drift (u_s). The wave phase speed (i.e. the speed at which the wave propagates) can be calculated by:

$$c_p = \sqrt{\frac{g}{k} \times \tanh(k \times d)} \tag{5.8}$$

Stokes' drift (i.e. the net speed at which fluid moves in the direction of the wave propagation) is calculated by:

$$u_s = \frac{1}{2} \times \sigma \times k \times a^2 \times \frac{\cosh(2 \times k \times (z+d))}{\sinh(k \times h) \times \sinh(k \times d)} \tag{5.9}$$

5.3 - Experiments

In order to test the adequacy of the Airy wave theory the waves generated should propagate along the wave tank with very little or no damping. The wavelength (and therefore its frequency and period) should also not change. The wave tank is of sufficient length that a wave does not have time to travel along the length of the tank, be reflected off the boundary wall and travel back again. This eliminates the possibility of a returning wave interfering with the measurement of the incoming waves.

The maximum particle height is measured at points along the first part of the wave tank. The measuring method used is the same as described in the previous chapter. The measuring points are at 1.0, 3.0, 5.0, 7.0, 9.0, 11.0, 13.0 and 15.0 metres from the left hand end of the wave tank. The measuring point at 1.0m is in the wave maker domain. All other points are in the main domain. Two wave tank lengths were used, namely a 50m wave tank and a 100m wave tank. In both tests the wave maker domain was of length 2m. The rest of the wave tank was the main domain. Clearly the wave maker domain length is far greater than it needs to be to maintain full support for all main domain particles. This is to allow the wave motion prescribed by the Airy wave theory to be observed and measured. The input variables used in all simulations are shown in table 5.1.

Kernel	Quintic (Wendland)
Time-Stepping	Symplectic
Viscosity Treatment	Full viscosity method
Spatial Resolution	0.05m
Smoothing Distance, h	0.065m
Time Step, dt	0.000125s
Mean Depth	0.5m

Table 5.1: SPHysics inputs for wave propagation simulations.

The quintic (Wendland) kernel has been chosen for these simulations as it is determined to be superior to the Gaussian kernel in Macià *et al* (2011). The Symplectic time-stepping scheme has been chosen as it performed most reliably when compared to the other time-stepping schemes. The full viscosity method was used based on experience built from the test cases in the previous chapter.

All simulations were run for 40 seconds. To allow the particles to settle the wave maker was not applied for the first 5 seconds. During this initialisation period the wave maker domain does not exist as the entire domain is the main domain.

Three wavelengths have been used during the simulations, (see table 5.2). The values of wave phase speed are calculated, using equation 5.8, as 2.09, 2.18 and 2.21 ms^{-1} for wavelengths 5, 10 and 20m respectively. By choosing the largest value of phase speed and length of time for which the wave maker operates (35 seconds) it was calculated that the first wave generated can travel a maximum of 77.35m. The distance between the end of the wave maker domain and the end boundary is 48m. The final measuring point is at 15m and therefore 35m from the end boundary. Thus the distance that a wave has to travel before it interferes with the wave measuring was estimated at 83m. Based on these conditions no reflected waves should be able to interfere with the measurement of the waves generated by the wave maker. As the margin between the maximum distance that the first wave has been calculated to be able to travel within the simulation time and the distance that a wave must travel before interfering with the results is not great a further simulation (5E) has been carried out. This simulation case (5E) is identical to test 5A. However, the wave tank is of length 100m. The purpose of the exercise has been to investigate whether results for these two test cases are identical. Such conclusion would prove the case that the waves are not propagating faster than the Airy wave theory predicts they should.

Test	Tank Length (m)	Wave Length, λ (m)	Wave Amplitude, a (m)	Stokes' Drift, u_s at t=40s (m)	Figures
5A	50	10	0.05	0.444	2, 3, 4, 14
5B	50	5	0.05	0.609	5, 6
5C	50	20	0.05	0.402	7, 8
5D	50	10	0.025	0.111	9, 10
5E	100	10	0.05	0.444	11, 12

Table 5.2: Wave propagation test variables.

In all figures the results have been corrected for the effect of Stokes' drift (see equation 5.9). This effect causes the particles in the wave maker domain to drift in the direction of the propagation of the waves. The far boundary of the main domain is fixed. Therefore drift causes the length of the domain available to decrease over time and fluid depth rises. This effect is constant over time. Therefore it may be corrected by calculating the gradient of the mean fluid depth over time and subtracting this gradient multiplied by time from the raw data. The total drift due to Stokes' drift, calculated using equation 5.9, over a 35 second period (remembering that the wave maker is not applied during the first 5 seconds of the simulation so there will be no Stokes' drift during this time) is shown in Table 5.2.

The results from test 5A are shown in figures 5.2, 5.3 and 5.4. For this test case the key constraints of maintaining wave amplitude and wave length as the wave propagates are met relatively well. In each of the figures there are spikes in the data. This is caused by a particle that is close to the surface not being found within the measuring point in one of the measuring time periods. This will cause the measured wave height to drop until a particle that is closer to the actual surface moves into the measuring region.

The wave length is clearly very well maintained as the frequency of the waves measured at each measuring point is constant. For this test case the wave amplitude is also maintained very well at each measuring point. The damping of the wave amplitude is minimal.

Figure 5.4 shows the maximum particle height at 1.0m (within the wave maker domain) and at 15.0m (the final measuring point in the main domain). The motion of the maximum particle height measured at 1.0m is sinusoidal, as described by the Airy wave theory. However, motions at 15.0m, whilst maintaining the wave amplitude and frequency, are no longer sinusoidal. The motion at the troughs of the waves is very similar to that measured at 1.0m. However, the discrepancy occurs at the peaks of the waves. This disagreement with the motion predicted by the Airy wave theory tends to increase as the wave travels further from the wave maker domain (see figures 5.2 and 5.3). This shows that the waves generated by the wave maker are not propagating along the wave tank correctly.

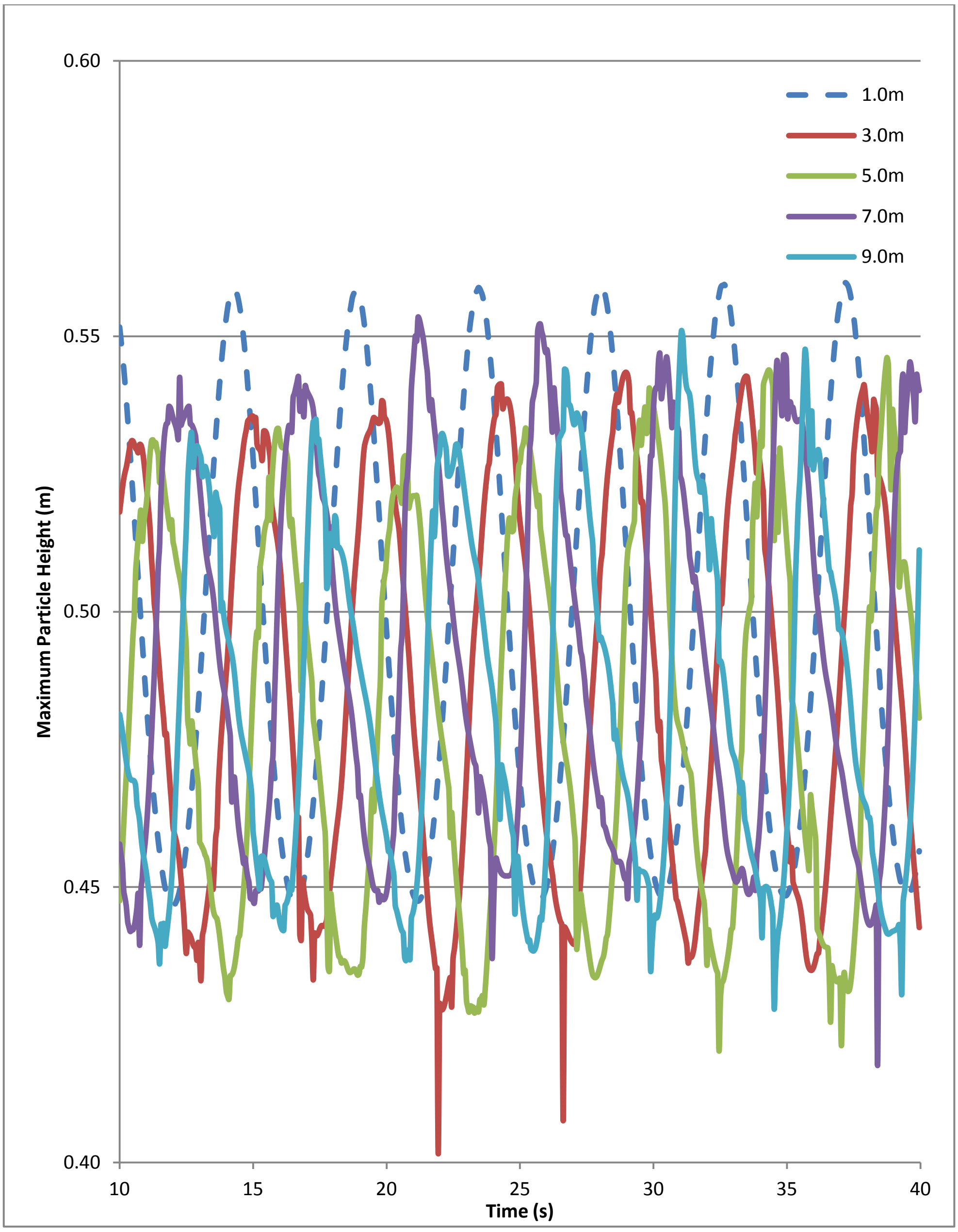

Figure 5.2: Wave propagation test 5A. 50m wave tank, 10m wavelength, 0.05m spatial resolution, 0.05m wave amplitude. Lines represent maximum particle height measured at each point over time. The blue dashed line is measured at 1.0m, within the wave maker domain. All other measuring points are in the main domain.

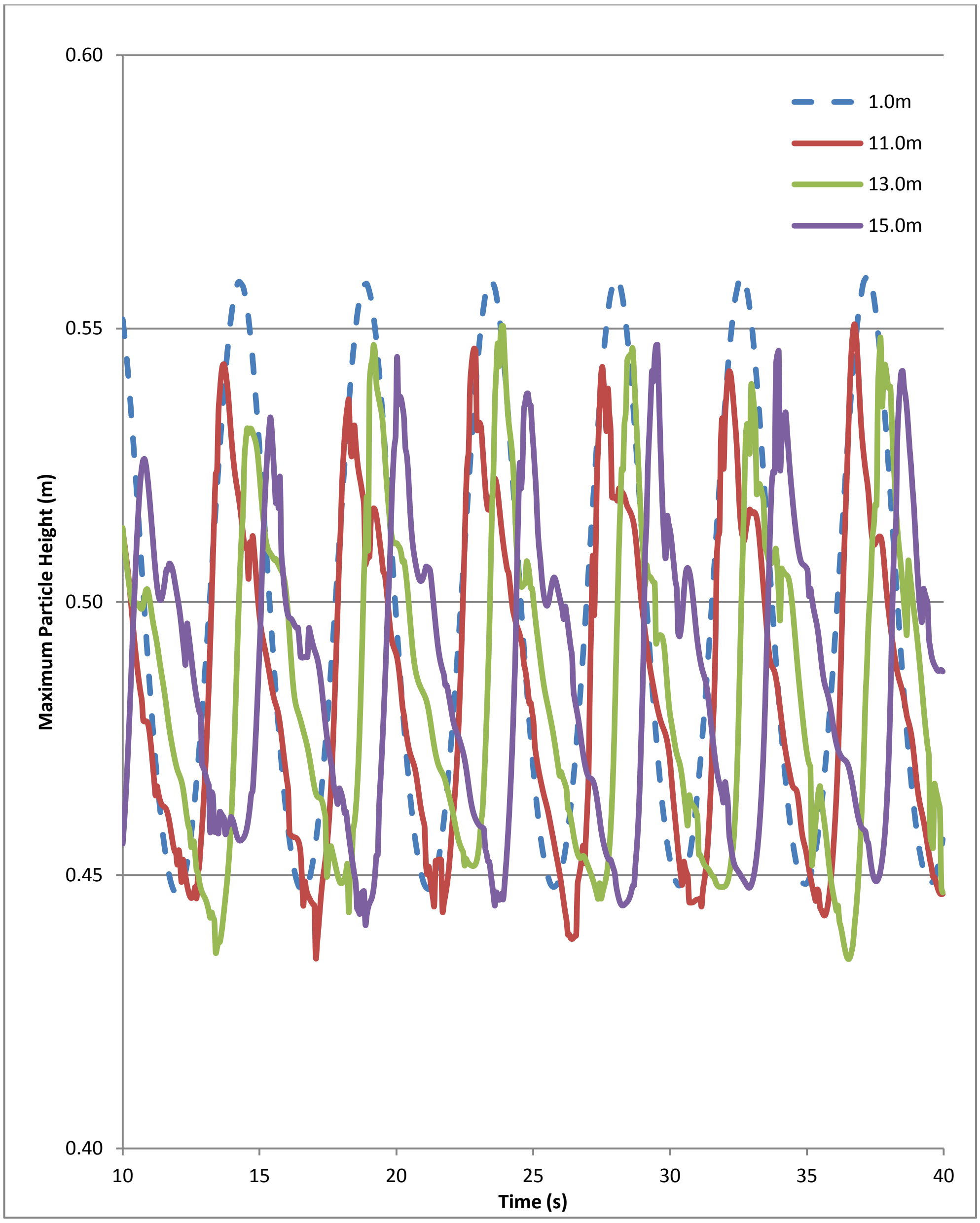

Figure 5.3: Wave propagation test 5A. 50m wave tank, 10m wavelength, 0.05m spatial resolution, 0.05m wave amplitude. Lines represent maximum particle height measured at each point over time. The blue dashed line is measured at 1.0m, within the wave maker domain. All other measuring points are in the main domain.

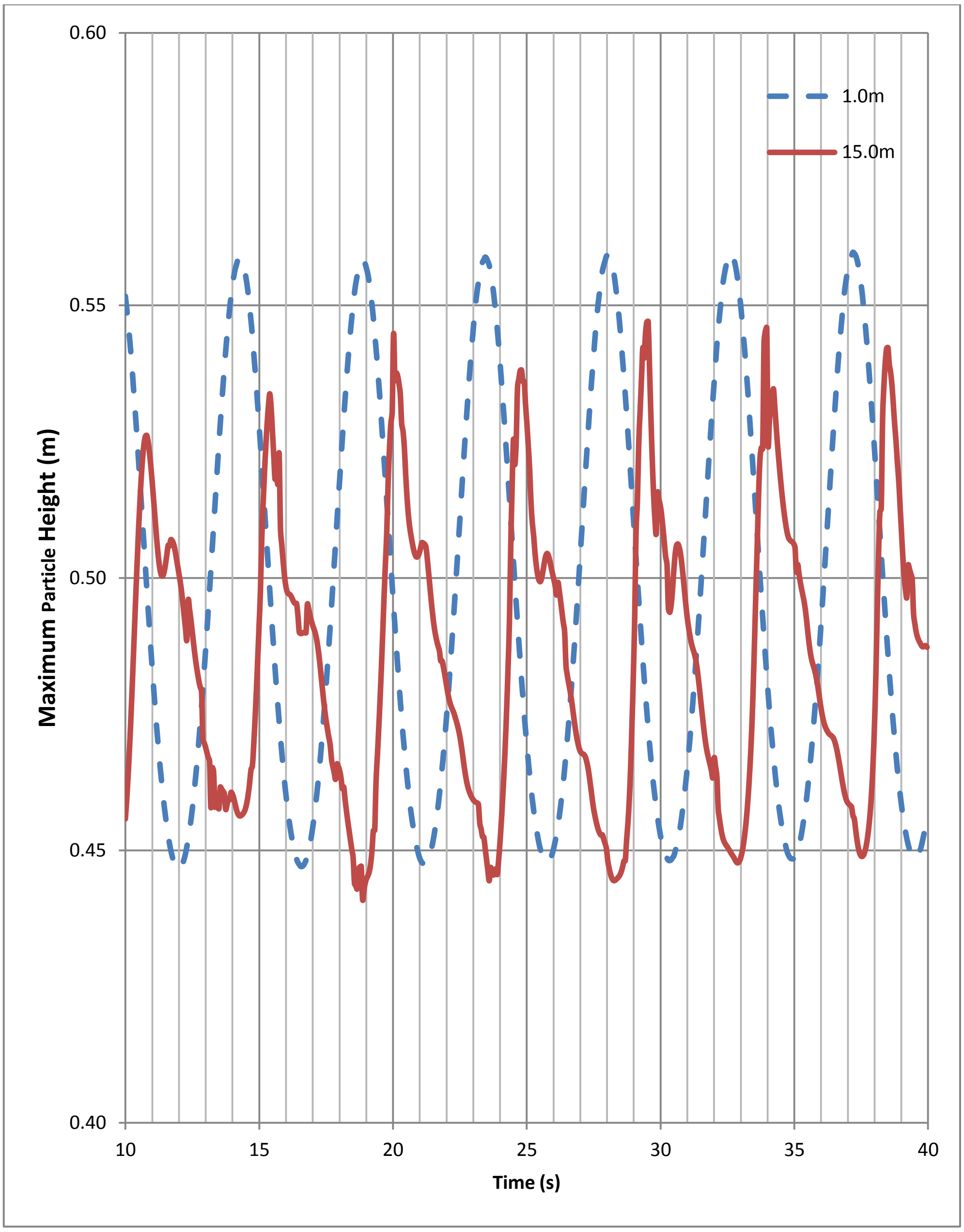

Figure 5.4: Wave propagation test 5A. 50m wave tank, 10m wavelength, 0.05m spatial resolution, 0.05m wave amplitude. Lines represent maximum particle height measured at each point over time. The blue dashed line is measured at 1.0m, within the wave maker domain. The other measuring point is at 15.0m, in the main domain.

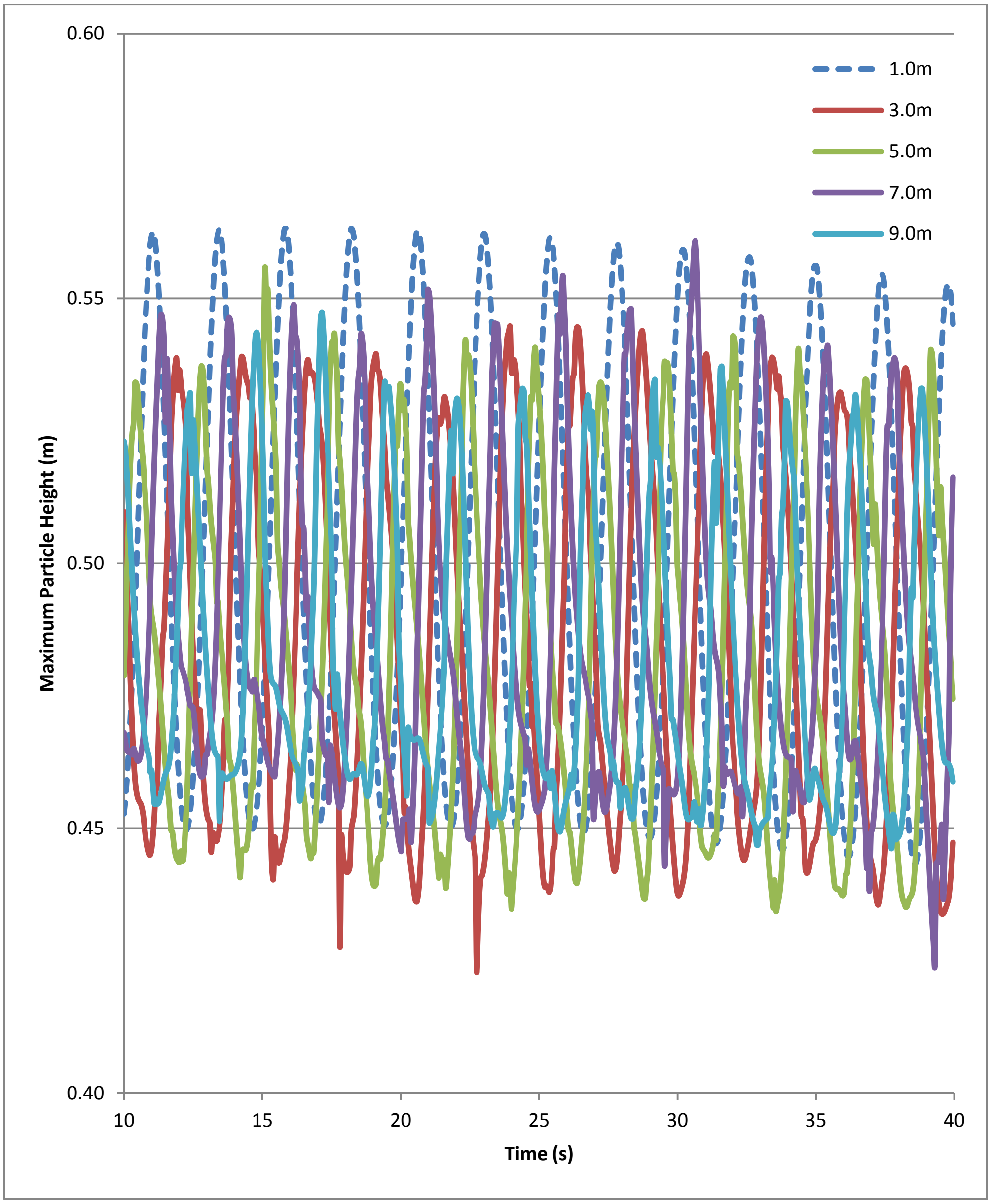

Figure 5.5: Wave propagation test 5B. 50m wave tank, 5m wavelength, 0.05m spatial resolution, 0.05m wave amplitude. Lines represent maximum particle height measured at each point over time. The blue dashed line is measured at 1.0m, within the wave maker domain. All other measuring points are in the main domain.

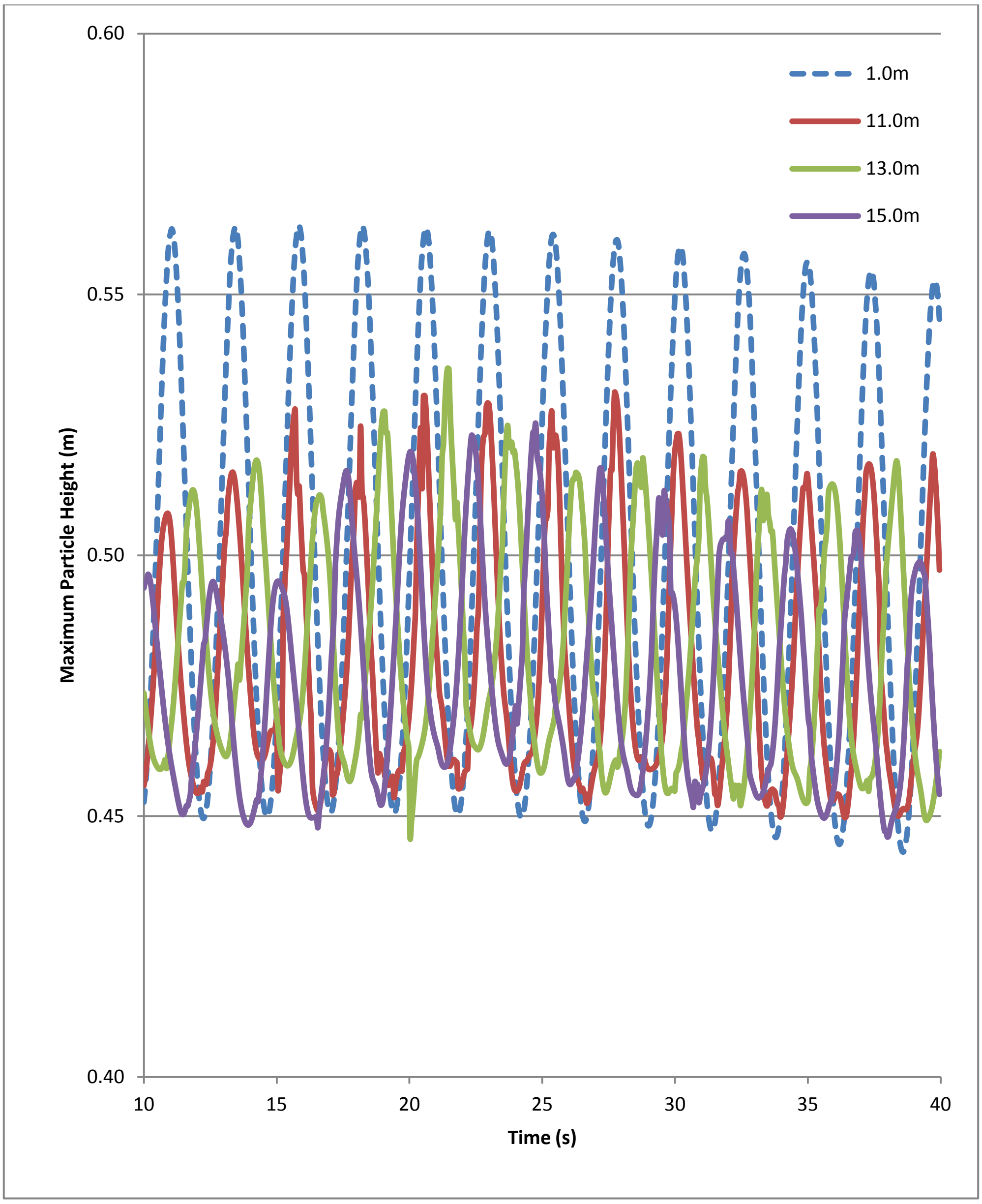

Figure 5.6: Wave propagation test 5B. 50m wave tank, 5m wavelength, 0.05m spatial resolution, 0.05m wave amplitude. Lines represent maximum particle height measured at each point over time. The blue dashed line is measured at 1.0m, within the wave maker domain. All other measuring points are in the main domain.

Figures 5.5 and 5.6 show the results from test 5B. This test case uses a shorter wavelength of 5m. When compared to the results from test 5A two differences can be seen:

- The wave amplitude damping is much greater for the shorter wavelength test case.

- The non-sinusoidal motion observed in figure 5.4 is not present in figure 5.6. As with the previous test case the wave frequency is maintained very well. The wave amplitude can clearly be seen to decrease as the wave propagates along the wave tank. However, by the time that the wave has reached the 15.0m measuring point it has lost almost 50% of its amplitude.

As the only difference between test cases 5A and 5B is the wavelength of the waves generated by the wave maker it must be concluded that, in 2D, the wave maker has some difficulty propagating waves that have short wavelengths. However, as can be seen in figure 5.5 the wave damping does not occur close to the wave maker. The amplitude of the waves measured at 9.0m (7m from the end of the wave maker domain) is roughly 90% of the input wave amplitude. This means that if the length of the domain required for an experiment is short then the excessive wave damping that occurs at short wavelengths does not matter.

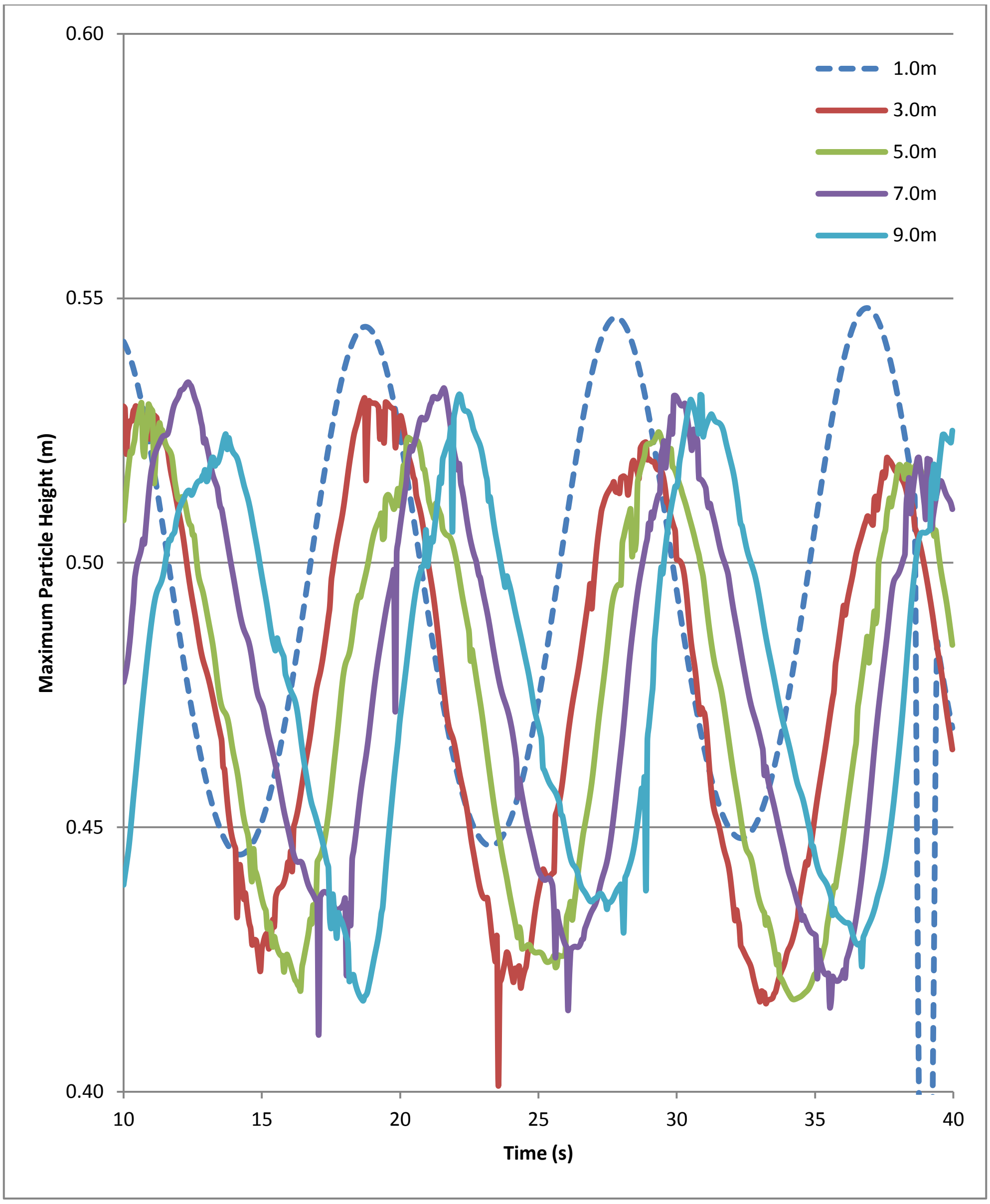

Figure 5.7: Wave propagation test 5C. 50m wave tank, 20m wavelength, 0.05m spatial resolution, 0.05m wave amplitude. Lines represent maximum particle height measured at each point over time. The blue dashed line is measured at 1.0m, within the wave maker domain. All other measuring points are in the main domain.

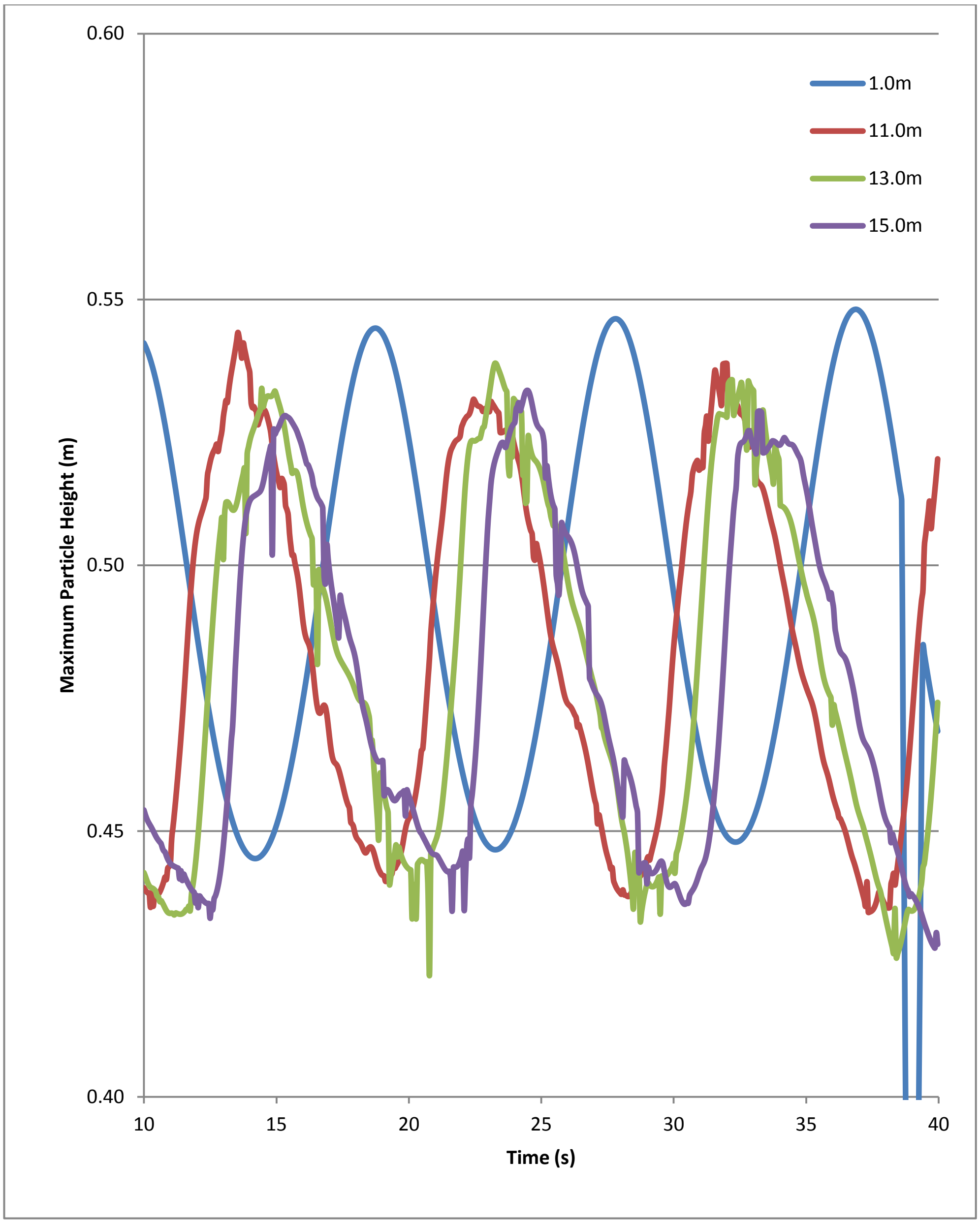

Figure 5.8: Wave propagation test 5C. 50m wave tank, 20m wavelength, 0.05m spatial resolution, 0.05m wave amplitude. Lines represent maximum particle height measured at each point over time. The blue dashed line is measured at 1.0m, within the wave maker domain. All other measuring points are in the main domain.

The results of test case 5C are shown in figure 5.7 and 5.8. In this test case a 20m wavelength is used. As this is a relatively long wavelength the amount of wave amplitude damping observed would not be expected to be large. The amount of wave damping seen in figures 5.7 and 5.8 bear out this expectation. As with the other test cases the wave frequency is maintained very well. As with test case 5A the wave form becomes less sinusoidal at the peaks as the wave propagates further along the wave tank. Notwithstanding the effect seems less pronounced than in test case 5A.

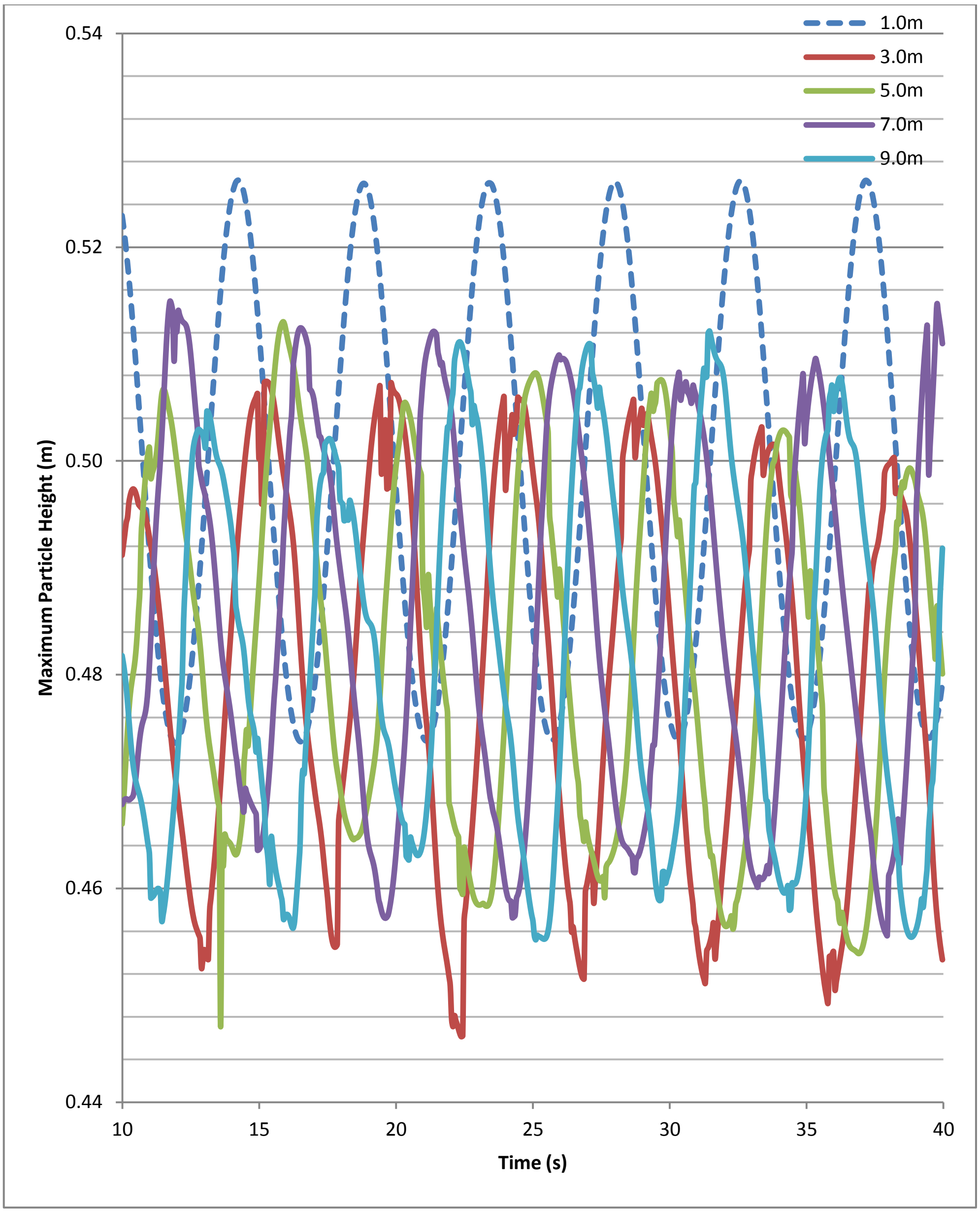

Figure 5.9: Wave propagation test 5D. 50m wave tank, 10m wavelength, 0.05m spatial resolution, 0.025m wave amplitude. Lines represent maximum particle height measured at each point over time. The blue dashed line is measured at 1.0m, within the wave maker domain. All other measuring points are in the main domain.

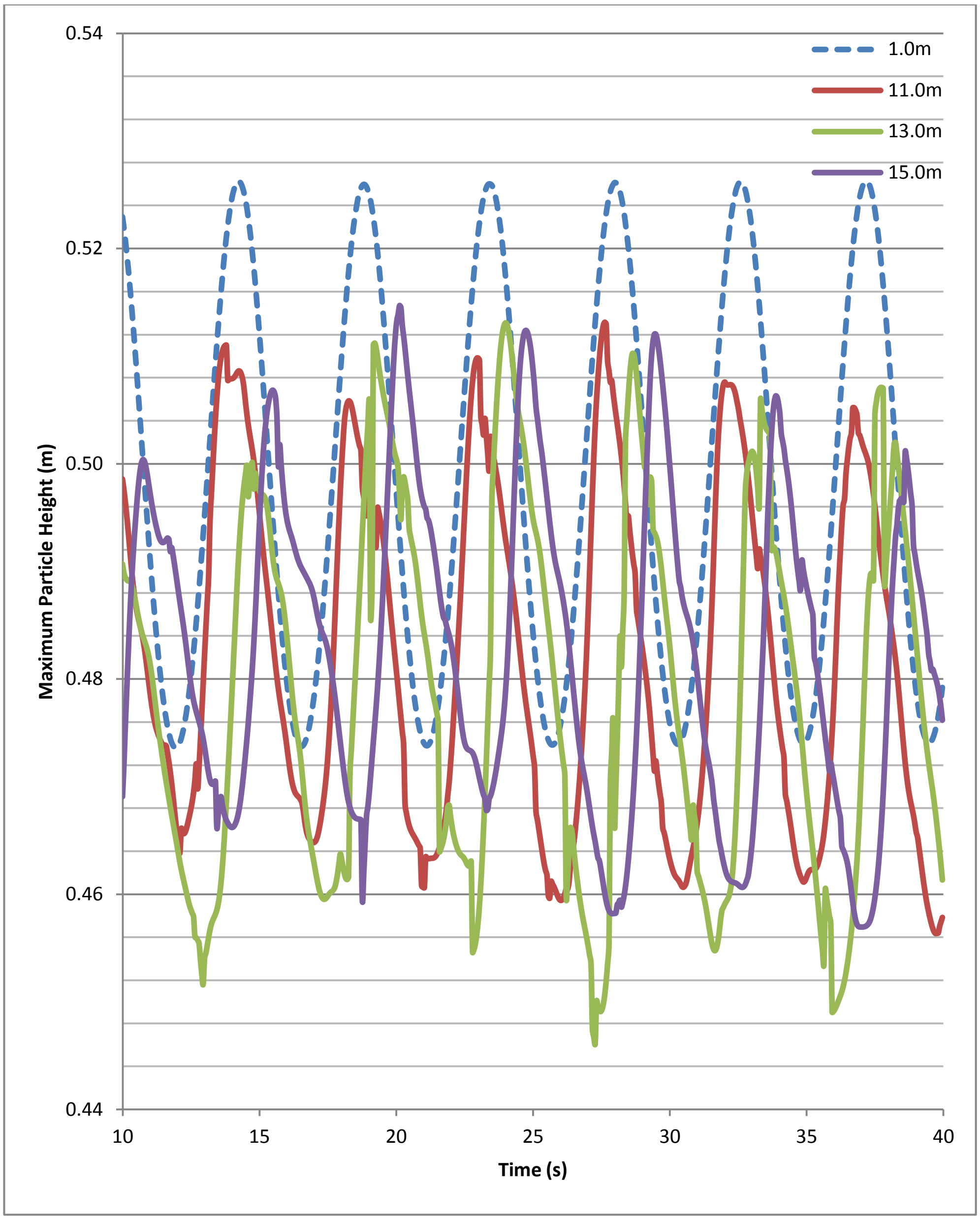

Figure 5.10: Wave propagation test 5D. 50m wave tank, 10m wavelength, 0.05m spatial resolution, 0.025m wave amplitude. Lines represent maximum particle height measured at each point over time. The blue dashed line is measured at 1.0m, within the wave maker domain. All other measuring points are in the main domain.

Test case 5D is designed to test whether the wave amplitude has any effect on the ability of the new framework to propagate waves. Therefore a wave amplitude of 0.025m is used rather than the amplitude of 0.05m used in all the other test cases. As the wavelength used is 10m the results from test case 5D need to be compared to the results from test case 5A. Overall the results are very similar. The speed at which the wave propagates remains constant along the wave tank and the amplitude of the waves is also maintained well. As with test case 5A the wave motion becomes less sinusoidal as the waves propagate along the wave tank but the discrepancy is less in test case 5D.

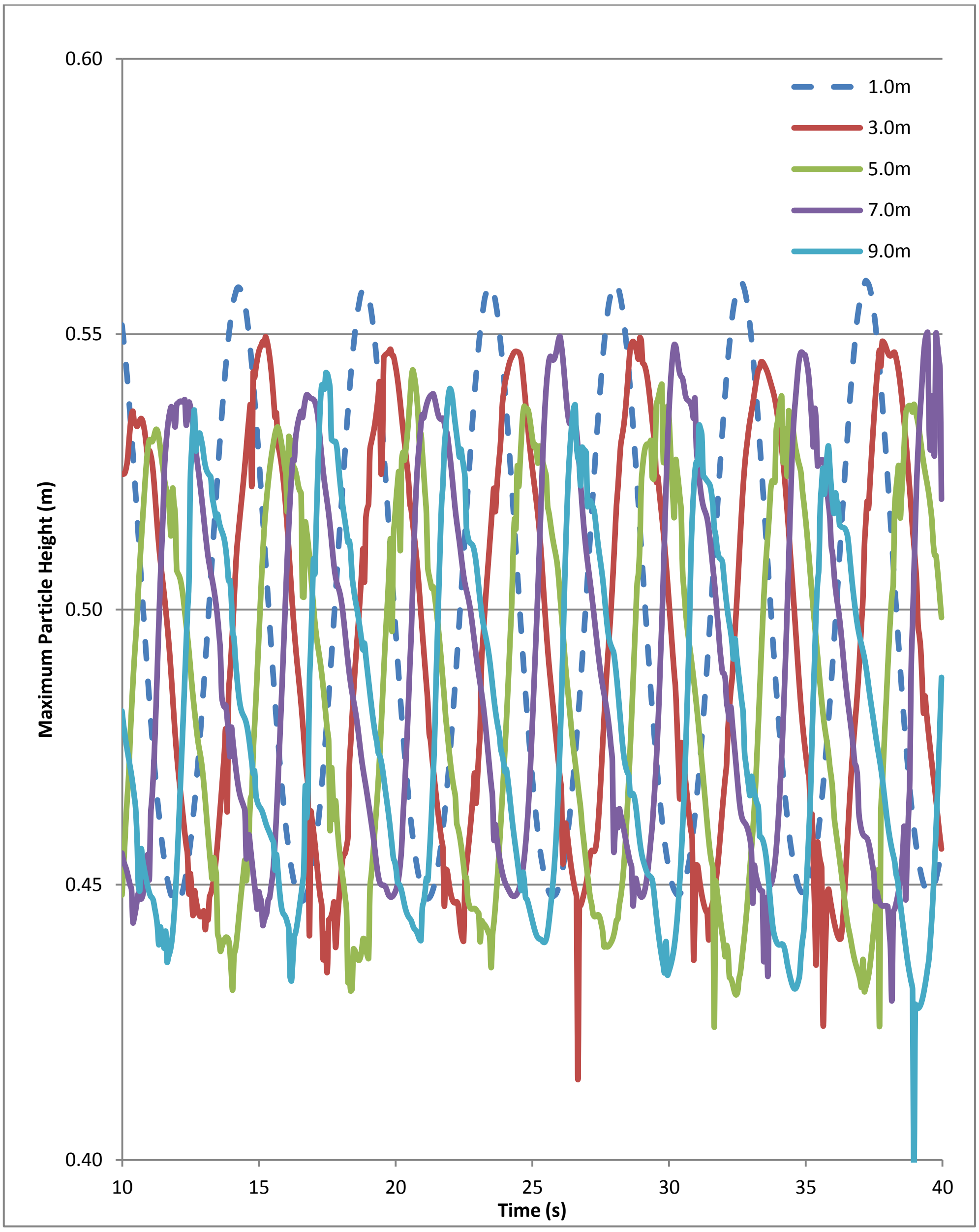

Figure 5.11: Wave propagation test 5E. 100m wave tank, 10m wavelength, 0.05m spatial resolution, 0.05m wave amplitude. Lines represent maximum particle height measured at each point over time. The blue dashed line is measured at 1.0m, within the wave maker domain. All other measuring points are in the main domain.

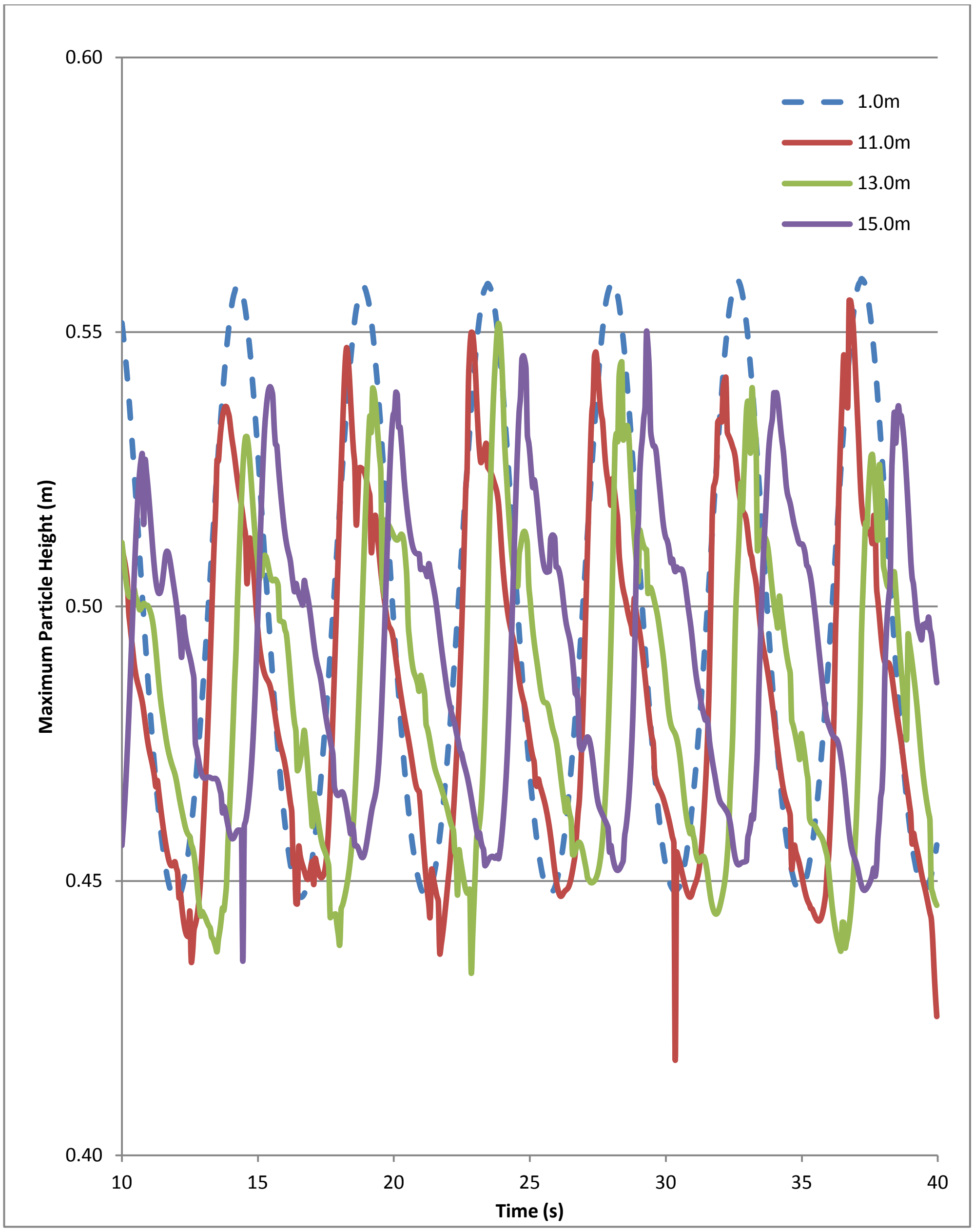

Figure 5.12: Wave propagation test 5E. 100m wave tank, 10m wavelength, 0.05m spatial resolution, 0.05m wave amplitude. Lines represent maximum particle height measured at each point over time. The blue dashed line is measured at 1.0m, within the wave maker domain. All other measuring points are in the main domain.

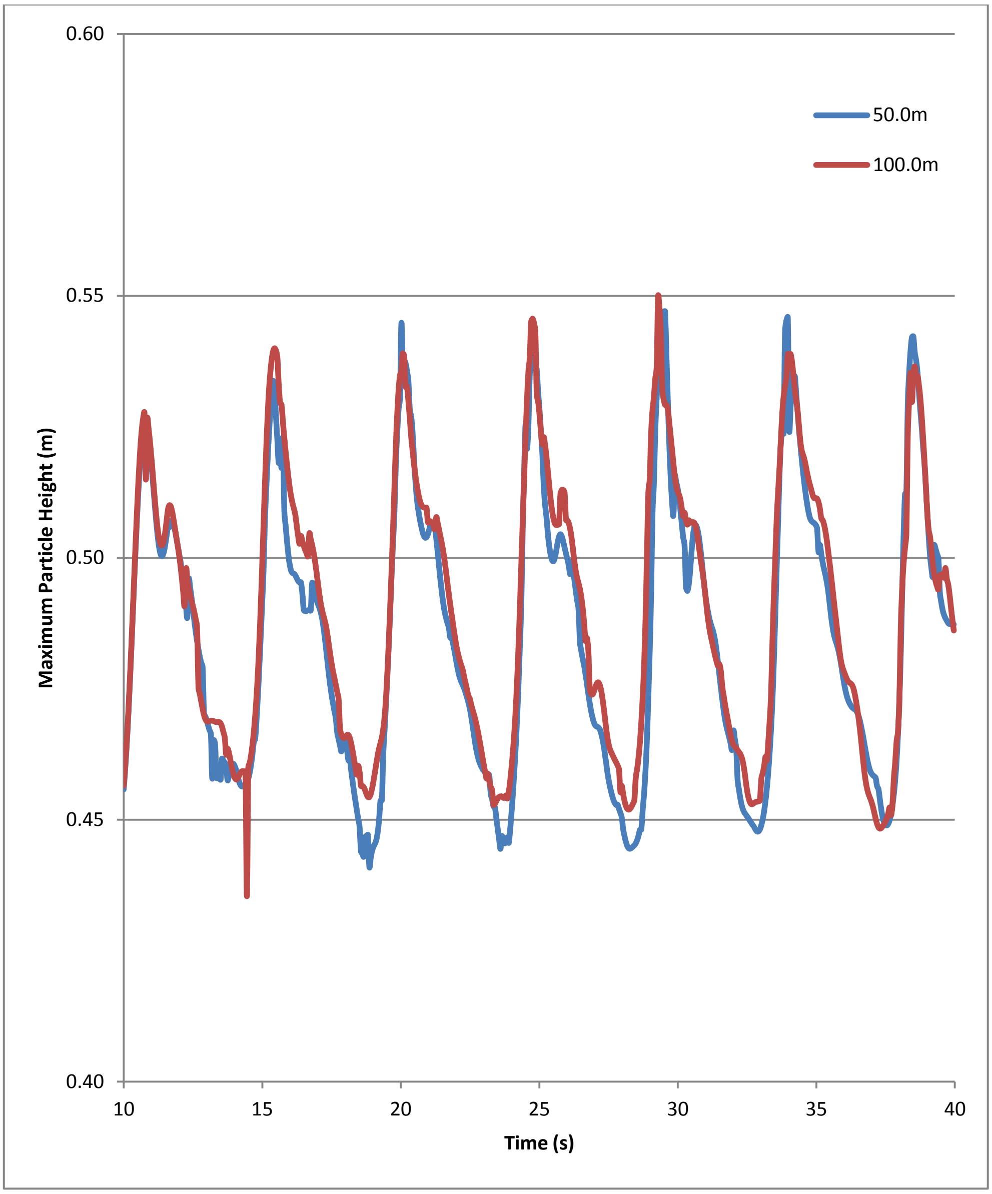

Figure 5.13: Comparison of maximum particle height at 15.0m for wave propagation tests 5A and 5E. 50/100m wave tank, 10m wavelength, 0.05m spatial resolution, 0.05m wave amplitude. Lines represent maximum particle height measured at each point over time. The blue line represents the 50m wave tank and the red line the 100m wave tank.

Figures 5.11, 5.12 and 5.13 show the results from test case 5E. This test case was compared to test case 5A. The difference being the length of the wave tank. There should have been no difference between the results of the two test cases. Figure 5.13 shows the results measured at 15m. If a wave was travelling faster than the Airy wave theory predicts then it would have time to interfere with the incoming waves measured at 15m for the 50m wave tank case. However, it is clear that the results between the two test cases are very similar. This indicates that the waves that are being generated by the wave maker are propagating at the correct speed.

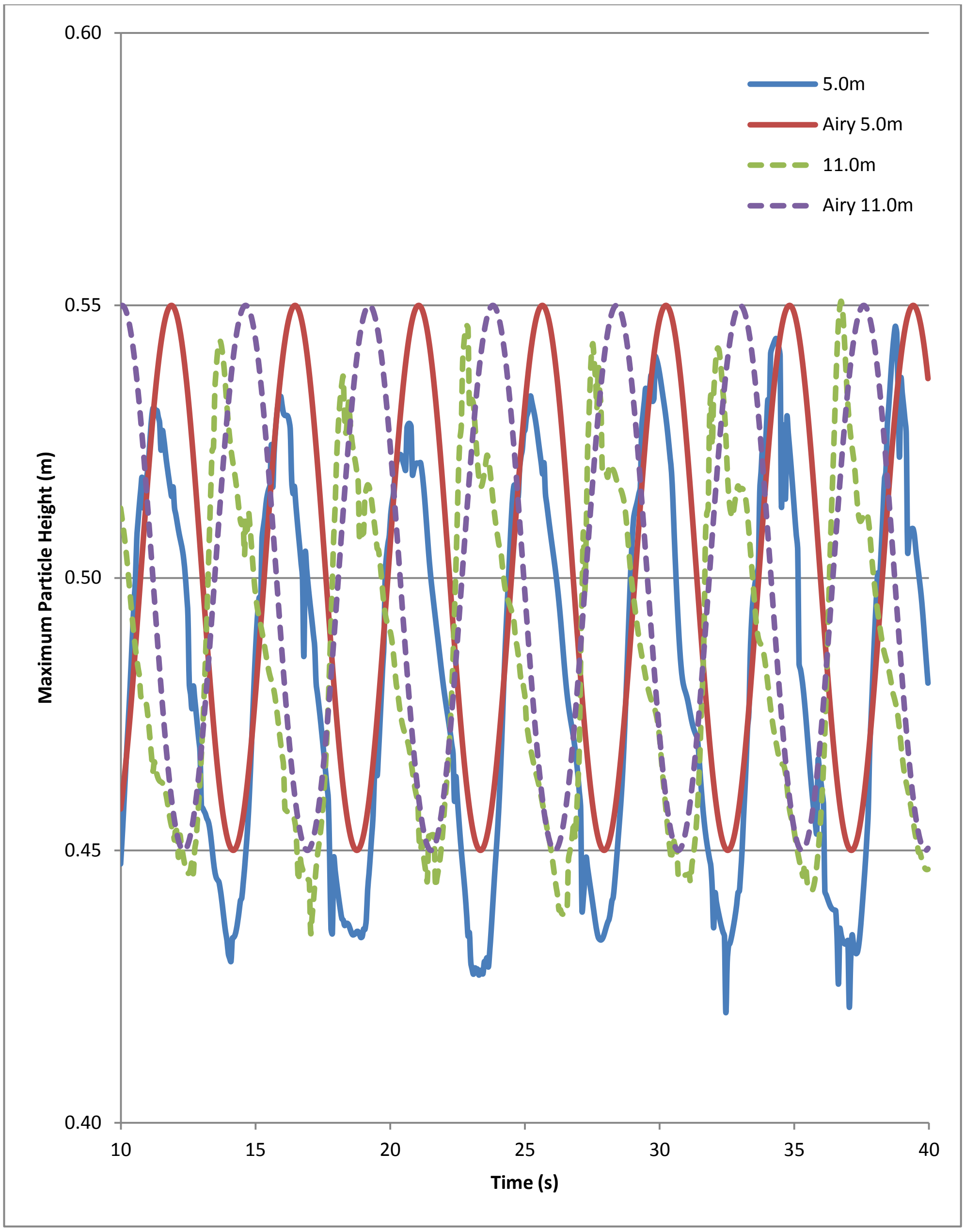

Figure 5.14: Wave propagation test 5A. 50m wave tank, 10m wavelength, 0.05m spatial resolution, 0.05m wave amplitude. Lines represent maximum particle height measured at each point over time. The solid lines represents results at 5.0m, the dashed lines at 11.0m.

Figure 5.14 shows the results of measurements taken at 5m and 11m for test case 5A compared against the wave motion calculated using the Airy wave theory. The first point to note is that the results from the test case were affected by the fact that the wave maker does not instantaneously generate full amplitude waves as it takes time to accelerate the wave maker particles from rest. This explains the phase shift between the Airy wave theory prediction and the simulation results that can be observed in figure 5.14. The test case results appear to have a phase lag of three quarters of a phase (or alternatively the calculated results lag by one quarter of a phase, since the waves generated are regular). This phase difference must be taken into account when comparing the results from the simulations with the motion predicted by the Airy wave theory. In practical terms this means that if the wave maker is to be used then the time taken to begin generating waves that agree with the Airy wave theory must be allowed for before meaningful measurements can be taken.

The test case results agree well with the calculated results (with the exception of the phase shift). However, one feature of the test case results that can be clearly seen is that the mean surface height appears to be slightly lower than the initial value of 0.5m. This result is caused by the particles in the main domain settling somewhat after the simulation is initialised. This is probably caused by the changes made to the repulsive boundary force. To resolve this problem a calibration simulation could be run to determine by how much the free surface drops and use this new depth in future simulations. It is worth noting that the wave amplitude and frequency is clearly maintained as it agrees well with the calculated results.

5.4 - Conclusions

A new wave maker has been created within the existing SPHysics framework and the effectiveness of the new methodology has been tested in 2D. The results from the test cases show that the wave maker is capable of generating waves. The motion of these simulated waves has been compared with the wave motions calculated using the Airy wave theory as shown in figure 5.14. There is a phase shift between the calculated and simulated wave motion, this is caused by the need for the particles to accelerate from rest.

Varying the wavelength of the waves between simulations has been investigated. The results of this study show that the wave maker produces wave motion that better agrees with the Airy wave theory when higher wavelengths are used. The effect of varying the wave amplitude between simulations has also been investigated. When the results of two simulations where the only variable is the wave amplitude are compared the resulting wave motions exhibit similar characteristics. The amplitude of the resulting waves shows good agreement with the input wave amplitude.

Some problems have been identified, primarily when shorter wavelength waves are generated. In such cases the wave amplitude is heavily damped as the wave propagates along the tank. However, the damping is barely discernible for a reasonable distance along the wave tank. It has a significant effect towards the final measuring points only. Therefore if the domain of a simulation is not too long then the unphysical wave damping can be ignored. The observed over-damping is less prevalent when higher wavelengths are used.

Some minor problems have also been observed. Firstly in the 10m wavelength test cases the wave motion at the latter measuring points can be seen to deviate from the sinusoidal wave motion predicted by the Airy wave theory. This effect has not been observed when other wavelengths have been used. Secondly the particles in the main domain settle downwards as the simulation begins. This behaviour can be accounted for by conducting a calibration simulation to correct the input fluid depth.

Chapter 6

Wave Damping and Inflow-Outflow

6.1 - Introduction

Chapter 5 discussed simulations which involved using a very long wave tank. The purpose of testing such idealisations has been to prevent any waves that were reflected off the boundary wall having time to return to the measuring area. This method clearly has two flaws. The computational domain must be large and this requires either a large computational effort or a low spatial resolution. The second flaw is that the simulation is time limited as eventually wave reflection will occur. To overcome this drawback a wave damping mechanism has been devised to allow a much smaller computational domain to be used whilst still preventing unwanted and unphysical wave reflection interfering with the wave motion.

Both the wave maker and damping mechanisms have been designed for use in simulations where there is a mean flow. Therefore a method for creating this mean flow has been devised and implemented within the SPHysics framework. This method has also been integrated with the wave maker and wave damping systems.

6.2 - Methodology

To generate a mean flow two modelling steps are required. Firstly as particles move downstream new particles must be introduced at the inflow boundary. Secondly as a particle moves outside of the computational domain, by crossing the outflow boundary, they must be removed from the domain. These two actions allow a relatively small number of particles to simulate the important part of a wave tank without having to simulate the entirety of the wave tank.

For the case where there are no waves, only a mean flow (e.g. a channel flow) the motion of particles in the wave maker domain is still prescribed, not according to the Airy wave theory but the desired flow speed. The horizontal velocity of particles in the wave maker domain is the mean flow speed and the vertical velocity is zero. As the particle motion in the wave maker domain is prescribed the time required for a particle to move a set distance is known. At the inflow new particles need to be introduced. The rate at which these particles are introduced is determined by the mean flow speed and the initial particle spacing according to the equation:

$$steps = \left|\frac{dx}{U \times dt}\right| \tag{6.1}$$

Where *steps* is the number of time steps between adding new inflow particles, *dx* is initial horizontal particle spacing, *U* is the mean flow speed and *dt* is the time step. When the number of time steps elapsed has reached the value calculated using equation 6.1 the fluid particles will have moved downstream. The distance that they will have moved downstream is equal to the particle spacing, *dx*. At this point a new column of particles will be added to the domain. The particles will be correctly spaced from existing particles.

The particles that are created are not 'new' particles. They are particles that have been stored at the edge of the computational domain and flagged as inactive. Each time particles are introduced the new particles are taken from the store and placed accordingly at the inflow boundary. The particles in the store are replenished by the particles that leave the computational domain by crossing the outflow boundary. This system allows the number of particles that are active in the computational domain to vary at each iteration. This is desirable as although the particles are introduced in a regular fashion the time at which particles leave the computational domain cannot be known beforehand.

The inflow described thus far has only concerned channel flow, without any waves. The wave maker described in the previous chapter is designed to be usable with a mean flow. To allow these two methods to be combined into one the following alteration is made to equation 6.1:

$$steps = \left|\frac{dx}{(U+u_x) \times dt}\right| \tag{6.2}$$

Where u_x is the horizontal component of a particles' velocity according to Airy wave theory as shown in equation 5.5. This alteration means that the number of time steps between introducing columns of new particles at the inflow boundary is dependent on the motion of the wave that is being generated. When the wave maker is generating the peak of a wave the value of u_x is positive and so the number of time steps between new particles being introduced is smaller. Therefore particles are introduced more frequently. Conversely when the wave maker is generating the trough of a wave u_x is negative and therefore the time between particles being introduced is increased. This method is used as if equation 6.1 is used then the waves that are generated will very quickly dissipate when they enter the main domain. This would occur because the wave maker causes the particles in a wave peak to be spread out vertically, if they are spaced at dx horizontally then the vertical spacing will decrease as the density of the particles will be relatively low. If however equation 6.2 is used then the reduction in density of the particles in a wave peak caused by the increased vertical separation will be countered by the reduced horizontal separation. A similar, but opposite, effect will be seen at a wave trough. Care must be taken to ensure that if the value of u_x is negative then it's magnitude is not greater than U as this will cause the number of time steps calculated by equation 6.2 to become negative. If this were to occur then this method should not be used.

The particle motion in the wave maker domain used by the wave maker method described in the previous chapter is wholly prescribed by the Airy wave theory using equations 5.5 and 5.6. The particle motion in the wave maker domain in the channel flow case is prescribed by the mean flow speed. As the two methods have been combined to create a wave tank method that can generate a mean flow with waves the particle motion from both methods is combined. Hence the particle motion in the wave maker domain is calculated using the following equations:

$$U_x = U + u_x \tag{6.3}$$

$$U_z = u_z \tag{6.4}$$

Where U is the mean flow speed, u_x is calculated using equation 5.5 and u_z is calculated using equation 5.6.

The wave damping mechanism is split into two parts; the first part is a sponge layer damping system and the second is a density based system. These two parts work in conjunction to damp out any waves that may reflect off the downstream boundary. The density based system also functions as the outflow mechanism.

In the preceding chapter the concept of splitting the computational domain into the inflow and main domains was introduced; the sponge layer is imposed in a third domain, the damping domain. This setup is shown in figure 6.1.

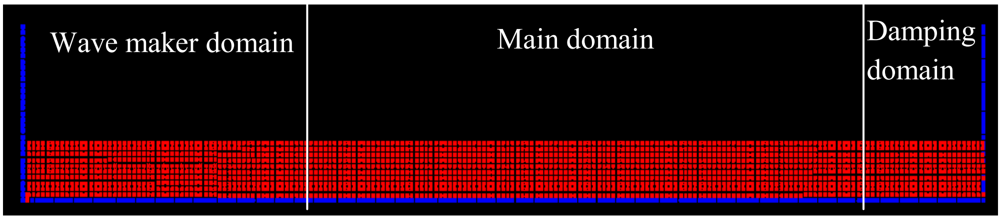

Figure 6.1: Domain layout.

The sponge layer is designed to damp out waves by damping out the vertical motion of the fluid particles. It achieves this by applying an additional term to vertical acceleration of any particle in the damping domain:

$$\dot{W}_{New} = \dot{W}_{Original} + Z_{GAIN} \times W_{DAMP} \tag{6.5}$$

Where $\dot{W}_{Original}$ is the standard SPHysics vertical acceleration, $\dot{W}_{New}$ is the modified vertical acceleration and Z_{GAIN} is a tuning coefficient to allow the effectiveness of the damping domain to be controlled. W_{DAMP} is the damping factor:

$$W_{DAMP} = -w \tag{6.6}$$

Where w is the vertical velocity of a particle. As a particle travels through the damping domain its vertical velocity is reduced to zero, this is designed to damp out any waves that are in the damping domain.

The additional particle acceleration term is not applied constantly across the entire damping domain. At the beginning of the damping domain the wave damping is brought in gradually. This is to prevent any incoming waves being reflected off the start of the damping domain. This arrangement is outlined in figure 6.2. At the boundary between the main domain and damping domain equation 6.5 is not applied. As a particle moves towards the outflow boundary the effectiveness of equation 6.5 is increased in a linear fashion. At a certain point the effectiveness of equation 6.5 is at 100% and remains at this value until the outflow boundary is reached. The way in which equation 6.5 is applied to particles in the damping domain can be altered to suit the requirements of any specific test case.

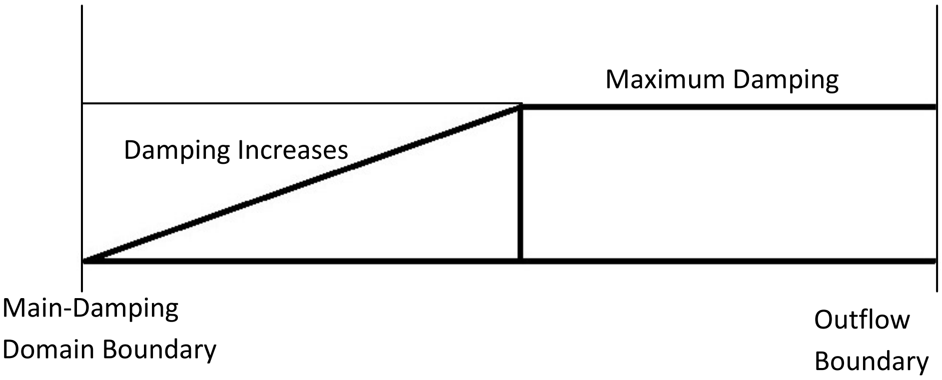

Figure 6.2: Damping domain layout.

The second component of the wave damping mechanism is the density based outflow boundary. This is a modification of the repulsive boundary force method included in SPHysics. The new mechanism works in the same way as the old method, that is as a fluid particle approaches a boundary particle a repulsive force is applied to the fluid particle. The purpose of the outflow boundary is to regulate the flow of particles across the boundary such that the fluid level in the main domain can be controlled. In most cases this will require that the average depth of the fluid in the main domain (both in time and space) is maintained at a constant level. If this constraint on the fluid depth is taken as the variable to be controlled by the outflow boundary then it is desirable that a self-controlling flow rate method be devised.

If the depth of the fluid at the outflow boundary is not the same as the target value that has been set for the test case then it can be deduced that this has been caused by the value of the mass flow rate across the outflow boundary. This could be because more particles have been added into the domain in the wave maker domain or alternatively because a wave that has not been fully damped out by the damping domain has reached the outflow boundary. If the fluid depth is below target then the mass flow rate across the boundary can be seen as having been too great. Conversely, if the fluid depth is above target then the mass flow rate has been too low. The outflow boundary has been designed to control the flow rate of particles leaving the domain and controls this rate by comparing the actual depth of the fluid near the outflow boundary to a preset target value.

The density of water at the surface was 1000 kgm^{-3}. This has been the starting point for calculation of the target density. The rate at which the density increases with depth in SPHysics must be calculated. This was done by conducting a test simulation using the correct input variables of the full simulation (spatial resolution, kernel, etc.); it is only necessary for the correct depth to be simulated, and therefore a much smaller computational domain can be used. The simulation is run for sufficient time for the particles to settle into an equilibrium and then the density of the particles is measured over depth so that the rate at which the density changes over depth can be deduced. The third component in calculating the target density is a correction factor for mean flow. The complete equation to calculate the target density (ρ_T) with zero mean flow is:

$$\rho_T = 1000 + d \times \Delta\rho_d \tag{6.7}$$

Where d is the depth below the still water free surface, in metres, and $\Delta\rho_d$ is the rate of change of density with depth. If there is a mean flow then equation 6.7 becomes:

$$\rho_T = 1000 + d \times \Delta\rho_d + V_{GAIN} \times \left(\frac{u}{U} - 1\right) \tag{6.8}$$

Where V_{GAIN} is a tuning coefficient, u is the horizontal component of the fluid particles' velocity and U is the mean flow speed.

When a fluid particle is within distance 2h of the outflow boundary the outflow boundary particles will apply a repulsive force on the fluid particle. If the outflow boundary were a normal repulsive boundary then the force applied would be sufficient to repulse the fluid particle before it is able to penetrate the boundary. However, since the outflow boundary is designed to be permeable this repulsive force needs to regulate the movement of the fluid particle. The repulsive force that is applied by the outflow boundary particles was modified using the following equation:

$$F_{OUTFLOW} = F_{REPULSIVE} \times \left(1 - \rho_{GAIN} \times \left(\frac{\rho_i - \rho_T}{\rho_T}\right)\right) \tag{6.9}$$

Where $F_{OUTFLOW}$ is the repulsive force applied by outflow boundary particles, $F_{REPULSIVE}$ is the repulsive force applied by a standard repulsive force boundary particle, ρ_{GAIN} is a tuning coefficient, ρ_i is the density of the fluid particle and ρ_T is calculated using either equation 6.7 or 6.8. Equation 6.9 compares the density of a fluid particle to the target density for that particle based upon the particles' depth and velocity. If the density of the fluid particle is below that of the target value, then the repulsive force applied by the outflow boundary particles will be increased. The density of the fluid particle may be below the target value for two reasons. Firstly, because the fluid particle velocity is greater than the mean flow speed. Secondly, because the free surface is below the target value. This will have the effect of reducing the horizontal velocity of the fluid particles or reducing the mass flow rate across the boundary therefore increasing the free surface level towards target. The opposite effect would occur if the density of the fluid particle is above target.

6.3 - Experiments

6.3.1 - Wave Damping

The test cases in this chapter are designed to test the effectiveness of the new wave damping mechanism and also the inflow-outflow method that generates a mean flow. The wave damping mechanism was tested by using a series of wave tank test cases, with no mean flow. For simplicity, the wave maker described in the previous chapter was used to generate waves and wave height measurements taken to see if any waves have been able to be reflected off the outflow boundary back into the main domain.

The wave tank test cases used a combination of different wave tank lengths and spatial resolutions. These variables are shown in table 6.1. The wave tank lengths have been chosen based upon the wavelength. The 6.0m wave tank was used to test the case where the wavelength is longer than the computational domain, the 20.0m wave tank case for when the wavelength is less than the wave tank. The 10.0m wave tank length was used to test the case where the wavelength is equal to the wave tank length and the 14.0m wave tank length was used to test the case where the main domain was the same length as the wavelength. In each test case the wave maker and damping domains were both of length 2m. It is important to note that the wavelength used is greater than the length of the damping domain. This is an improvement on the simulations described in Lind *et al* (2011) where the damping domain was at least as long as the wavelength.

Test Case	Wave Tank Length (m)	Wavelength, λ (m)	Spatial Resolution (m)
6A	6.0	10.0	0.1
6B	6.0	10.0	0.05
6C	6.0	10.0	0.025
6D	6.0	10.0	0.0125
6E	10.0	10.0	0.05
6F	14.0	10.0	0.05
6G	20.0	10.0	0.05
6H	20.0	10.0	0.025

Table 6.1: Wave damping test cases.

The wave heights are measured at points along the wave tank in all three domains. The wave height is measured at 1.0m, at the mid-point of the wave maker domain. This allows the waves generated to be checked against the wave motion predicted by the Airy wave theory. The wave height is also measured in the damping domain. The point at which the measurement is taken is at the mid-point of the damping domain; this point is 1.0m from the outflow boundary. This measurement point allows the effectiveness of the wave damping methodology to be determined. The wave height is also measured at points in the main domain, the data taken from these measurement points will form the results of these test cases. The measurement points used in the main domain are firstly at 3.0m, 1.0m into the main domain, and secondly at 3.0m from the outflow boundary. This second measuring point is 1.0m from the end of the main domain. Clearly the location of this measuring point depends upon the length of the wave tank.

Kernel	Gaussian
Time-Stepping	Symplectic
Viscosity Treatment	Full viscosity method
Spatial Resolution	0.1m / 0.05m / 0.025m / 0.0125m
Smoothing Distance, h	0.13m / 0.065m / 0.0325m / 0.0163m
Time Step, dt	0.000125s
Mean Depth	0.5m

Table 6.2: SPHysics inputs for test cases 6A-6H.

The Gaussian kernel was used in these test cases even though the quintic (Wendland) kernel is determined as superior in Macià *et al* (2011). In this work when the test cases were run using the quintic (Wendland) kernel an unacceptably small time step was required to ensure that the simulation remained stable. The Symplectic time-stepping scheme has been chosen as it performed most reliably when compared to the other time-stepping schemes. The full viscosity method was used as it had been used successfully in the test cases in the previous chapter.

For test cases 6A to 6H a series of six simulations were carried out and the value of Z_{GAIN} used in equation 6.5 was varied. The values of Z_{GAIN} used in each test case were 0, 10, 25, 50, 100 and 250, when Z_{GAIN} is zero there is no damping. In each of these test cases the wave tank has solid boundaries and therefore there was no outflow boundary. Therefore the value of ρ_{GAIN} was set to zero. Test cases 6A to 6H are designed to show that the wave damping methodology is capable of damping out waves that enter the damping domain to such an extent that a wave cannot be reflected off the outflow boundary and return to interfere with the waves in the main domain.

Figures 6.3 to 6.8 show the results from test case 6H. The wave height is measured at 1.0m (in the wave maker domain), 3.0m (in the main domain) and 19.0m (in the damping domain). Figure 6.3 shows the results from the test case where a value of Z_{GAIN} is zero. The value of Z_{GAIN} is increased in each further figure until figure 6.8 where the value of Z_{GAIN} is 250. It should be noted that due to the effect of Stokes' drift discussed in chapter 5 the mean wave height measured in the main and damping domains will increase over time.

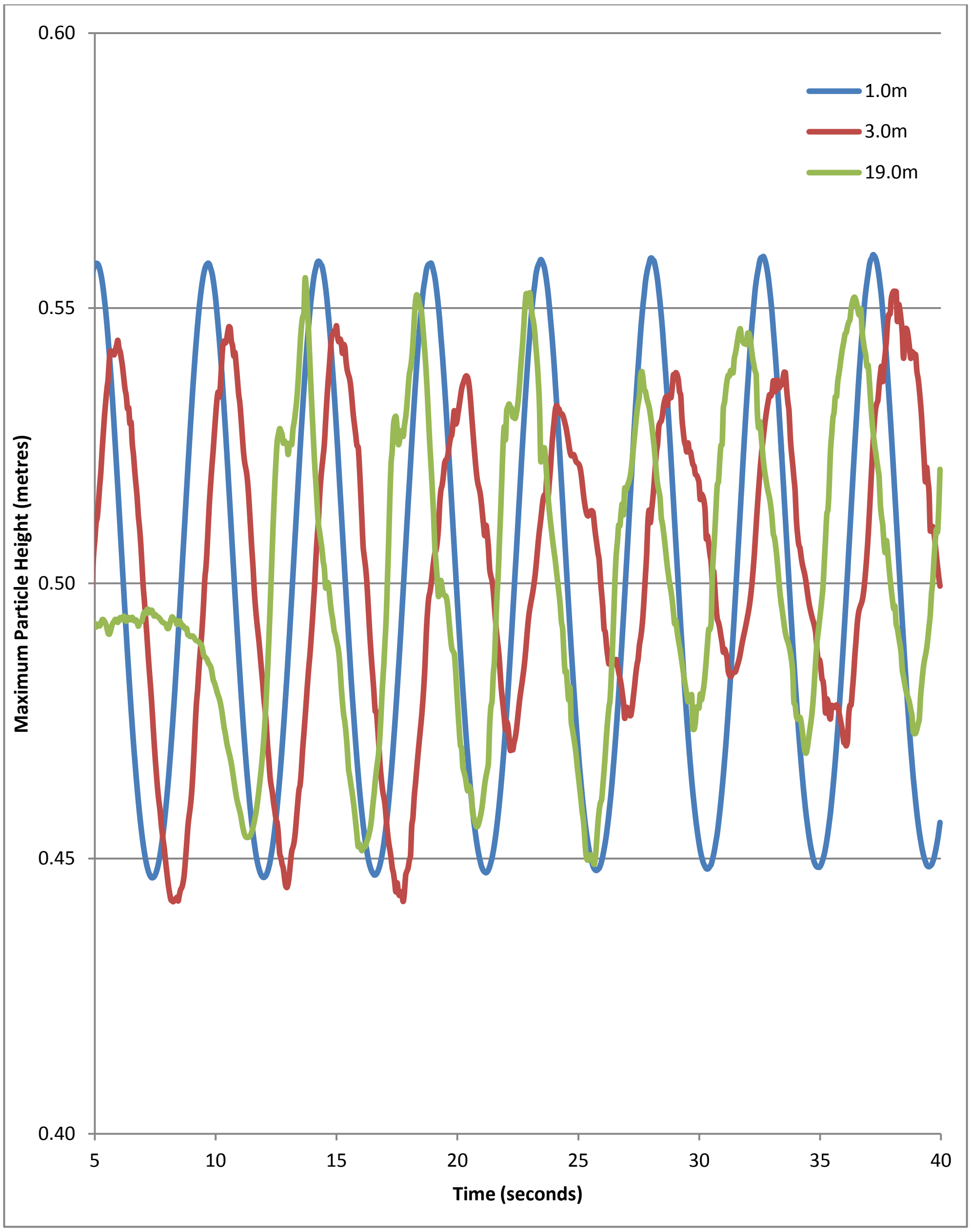

Figure 6.3: Wave propagation test 6H. $Z_{GAIN} = 0$. 20m wave tank, 10m wavelength, 0.025m spatial resolution, 0.05m wave amplitude. Lines represent maximum particle height measured at each point over time. The blue line is measured at 1.0m (within the wave maker domain), the red line is measured at 3.0m (within the main domain) and the green line is measured at 19.0m (within the damping domain).

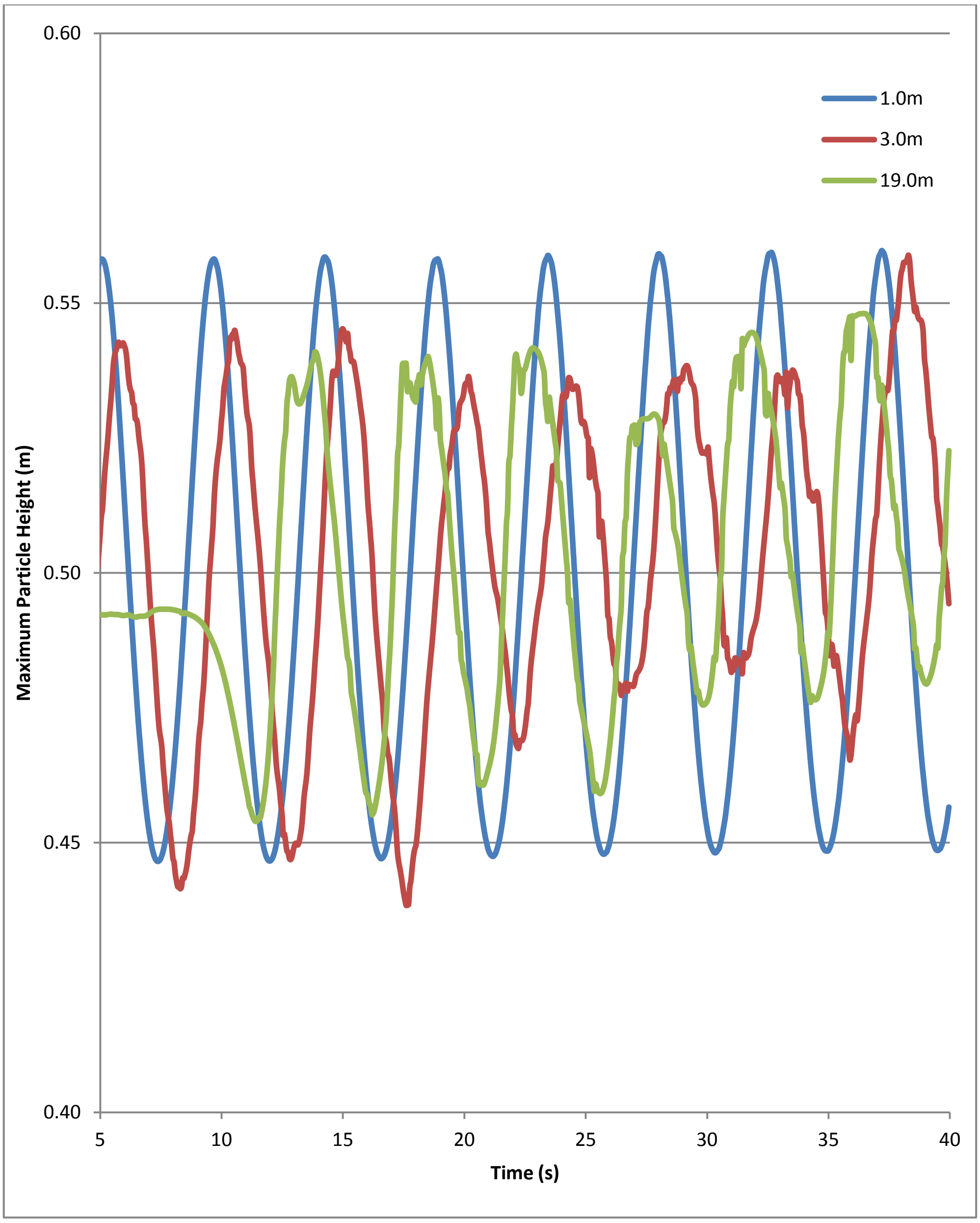

Figure 6.4: Wave propagation test 6H. Z_{GAIN} = 10. 20m wave tank, 10m wavelength, 0.025m spatial resolution, 0.05m wave amplitude. Lines represent maximum particle height measured at each point over time. The blue line is measured at 1.0m (within the wave maker domain), the red line is measured at 3.0m (within the main domain) and the green line is measured at 19.0m (within the damping domain).

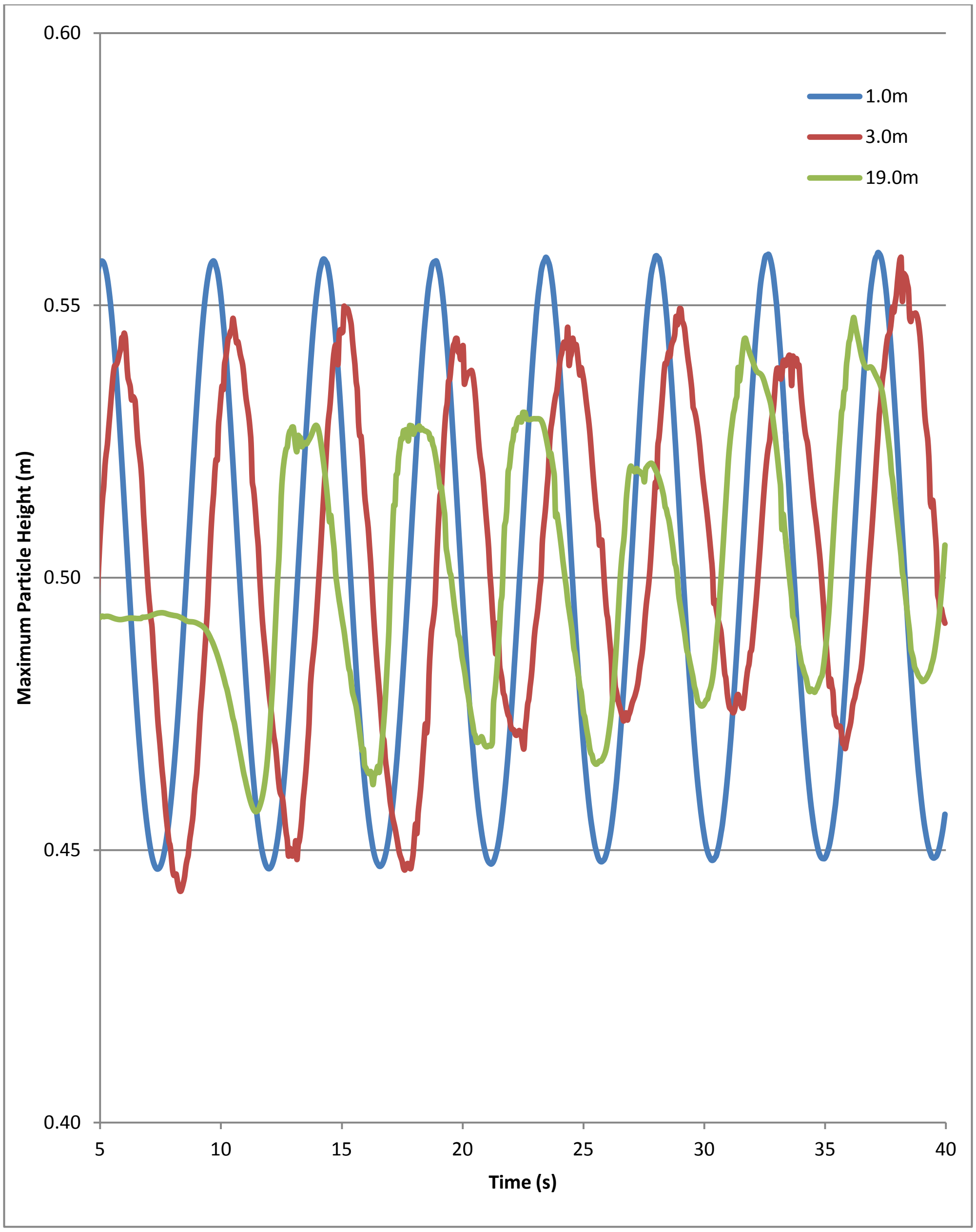

Figure 6.5: Wave propagation test 6H. Z_{GAIN} = 25. 20m wave tank, 10m wavelength, 0.025m spatial resolution, 0.05m wave amplitude. Lines represent maximum particle height measured at each point over time. The blue line is measured at 1.0m (within the wave maker domain), the red line is measured at 3.0m (within the main domain) and the green line is measured at 19.0m (within the damping domain).

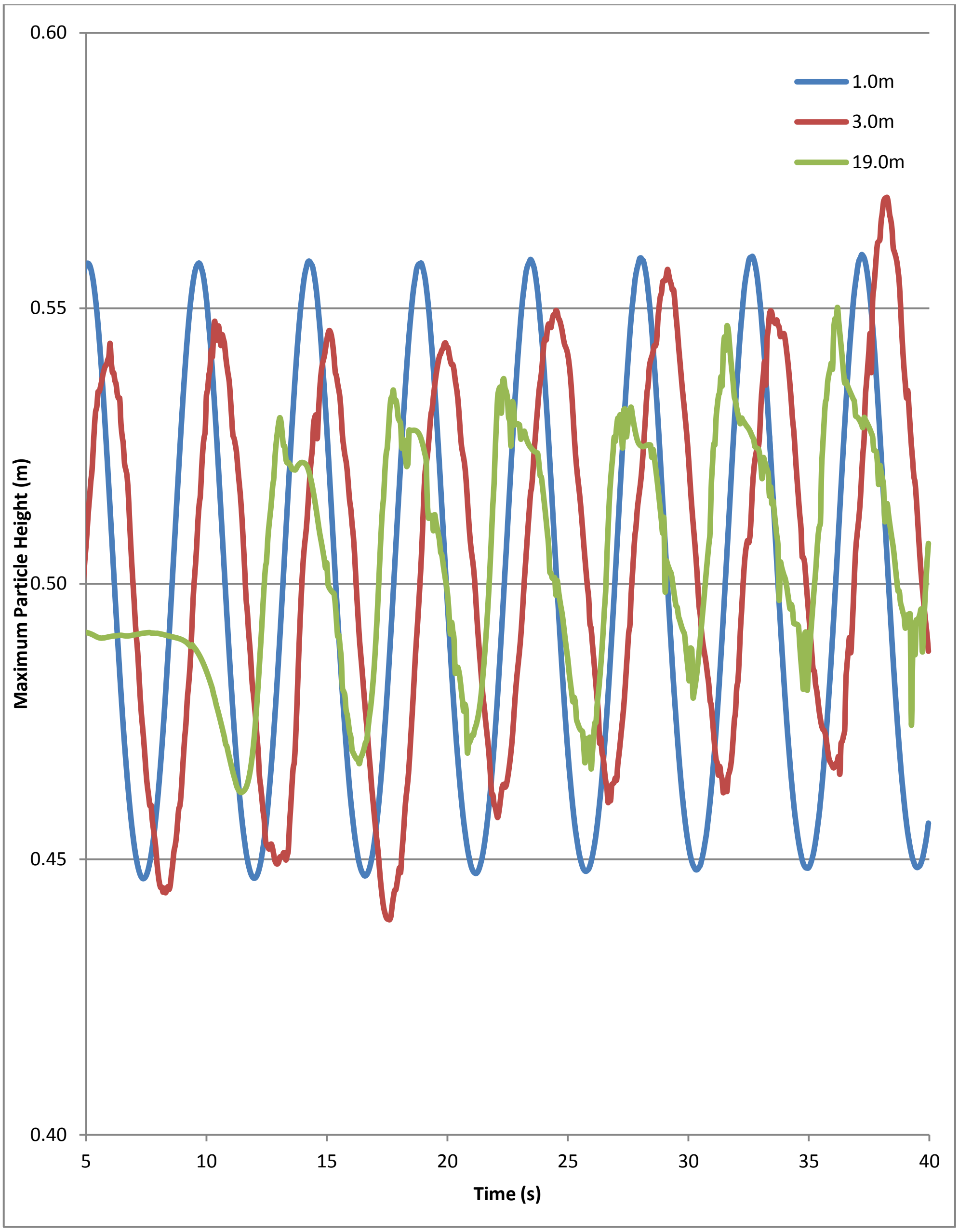

Figure 6.6: Wave propagation test 6H. Z_{GAIN} = 50. 20m wave tank, 10m wavelength, 0.025m spatial resolution, 0.05m wave amplitude. Lines represent maximum particle height measured at each point over time. The blue line is measured at 1.0m (within the wave maker domain), the red line is measured at 3.0m (within the main domain) and the green line is measured at 19.0m (within the damping domain).

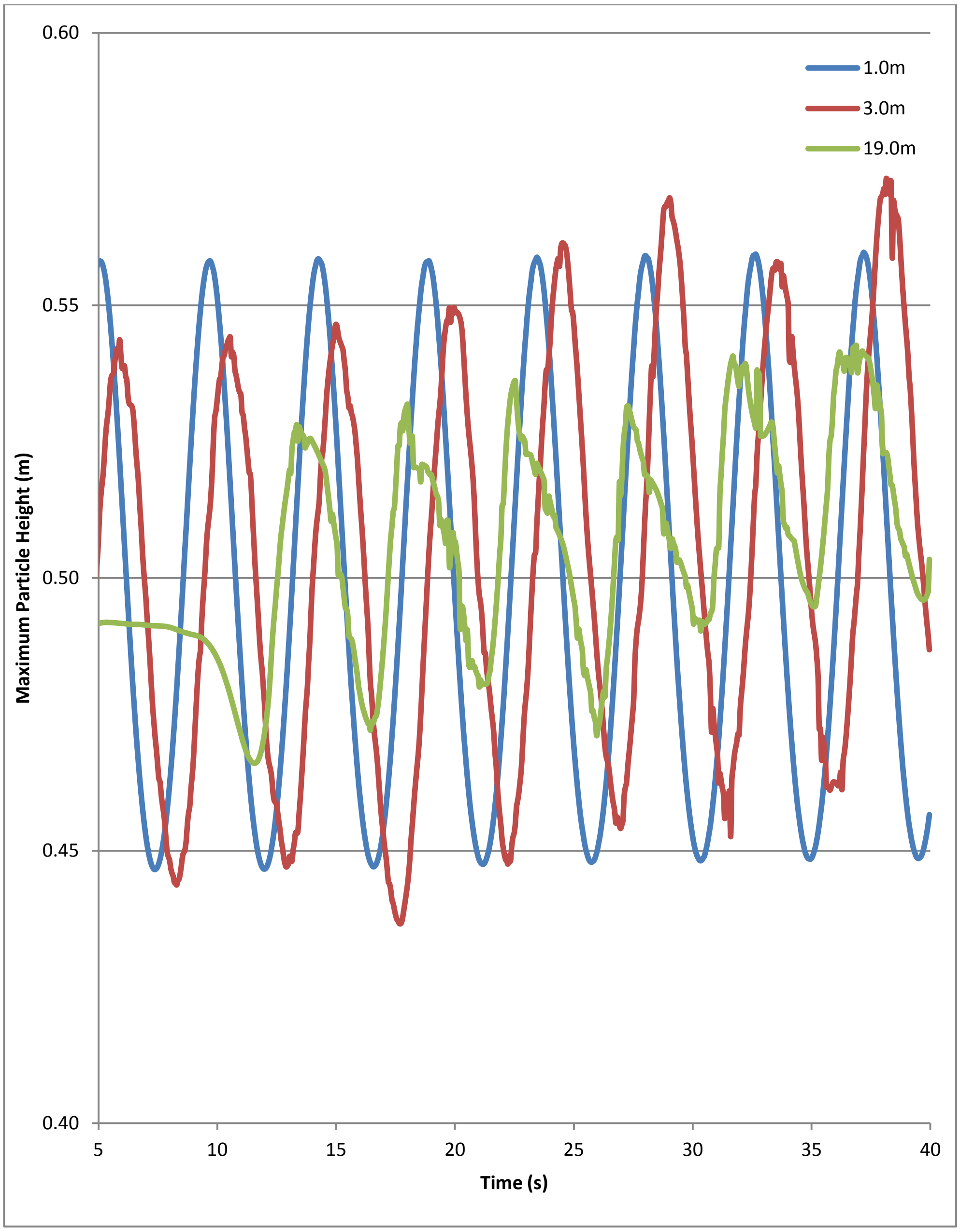

Figure 6.7: Wave propagation test 6H. Z_{GAIN} = 100. 20m wave tank, 10m wavelength, 0.025m spatial resolution, 0.05m wave amplitude. Lines represent maximum particle height measured at each point over time. The blue line is measured at 1.0m (within the wave maker domain), the red line is measured at 3.0m (within the main domain) and the green line is measured at 19.0m (within the damping domain).

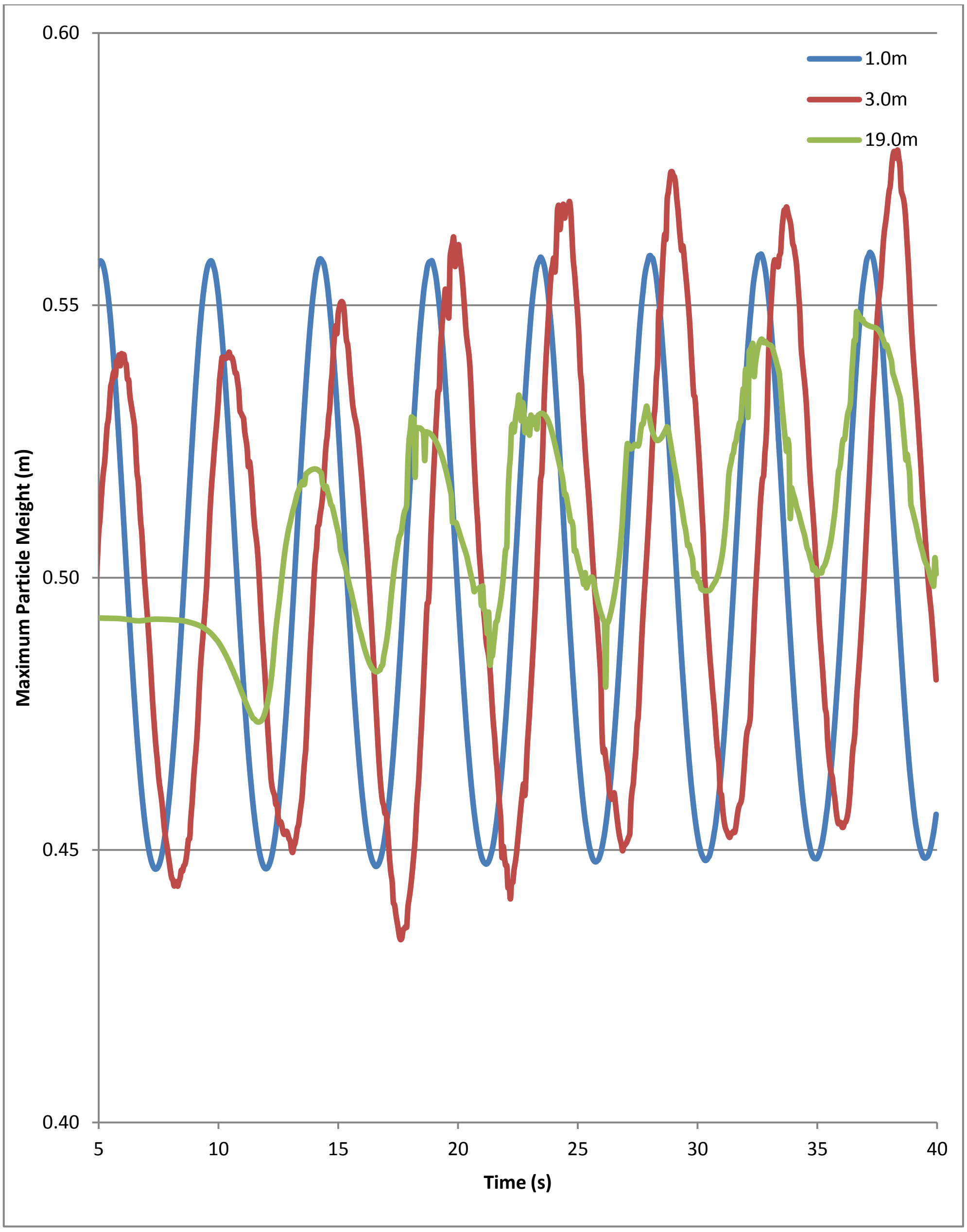

Figure 6.8: Wave propagation test 6H. Z_{GAIN} = 250. 20m wave tank, 10m wavelength, 0.025m spatial resolution, 0.05m wave amplitude. Lines represent maximum particle height measured at each point over time. The blue line is measured at 1.0m (within the wave maker domain), the red line is measured at 3.0m (within the main domain) and the green line is measured at 19.0m (within the damping domain).

Figure 6.3 shows the results when Z_{GAIN} is zero, as expected the wave amplitude measured at 19.0m initially is similar to that measured at 1.0m and 3.0m; this is because there is no damping to damp out the waves. The waves measured at 3.0m show that initially the waves show the correct amplitude. However after 18 seconds the amplitude of the waves can be seen to decrease. This is clearly the effect of reflected waves interfering with the incoming waves. Again this effect is to be expected as there is no wave damping applied. A similar result is seen in figures 6.4 and 6.5 where the value of Z_{GAIN} is 10 and 25 respectively. However, the effect of the reflected waves on the amplitude of the incoming waves is reduced as the value of Z_{GAIN} is increased.

Figure 6.6 shows the results when Z_{GAIN} is 50. The wave amplitude measured at 3.0m is much closer to the input wave amplitude. However, there is still a change in the wave amplitude after 18 seconds. This shows that the wave damping is still not sufficiently effective to fully damp out the wave. Figure 6.7 shows the result when Z_{GAIN} is 100, the wave amplitude measured at 3.0m is now almost identical to the input wave amplitude. There is also no discernible change in the measured wave amplitude at 18 seconds as was observed in the previous figures where the value of Z_{GAIN} is less. A further point to note when comparing the results shown in figures 6.6 and 6.7 is that the wave amplitude measured at 19.0m is significantly less than that observed in the previous figures. This clearly demonstrates that the wave damping mechanism is capable of damping out incoming waves sufficiently to prevent the waves interfering with other waves in the main domain.

When comparing the results shown in figures 6.6 and 6.7 it is important to note that motion of the waves at 3.0m is closer to the wave motion at 1.0m (which is defined by the Airy wave theory) in figure 6.7 than 6.6. This shows that the increase in Z_{GAIN} has reduced the wave reflection which is interfering with the wave motion at 3.0m. The fifth and seventh peaks at 3.0m in figure 6.7 are much closer, in terms of amplitude, to the peaks at 1.0m when compared to the same peaks in figure 6.6. The fourth trough at 3.0m in figure 6.7 is much closer to the 1.0m value when compared to the same trough in figure 6.6. The value for subsequent troughs is also closer to the 1.0m value in figure 6.7 when compared to 6.6.

Figure 6.8 shows the results when Z_{GAIN} is 250. The wave amplitude measured at 19.0m shows that the wave damping mechanism is damping out the incoming wave very successfully, more effectively than when a Z_{GAIN} of value 100 was used. The wave amplitude measured at 3.0m shows the wave amplitude initially being correct. However at approximately 15 seconds the wave amplitude can be seen to increase above the correct value. The wave amplitude decreasing at about 18 seconds was seen in figures 6.3 to 6.6 and had been caused by a wave reflecting off the outflow boundary due to insufficient wave damping. In figure 6.8 the wave amplitude is seen to increase rather than decrease and the change occurs slightly sooner than in figures 6.3 to 6.6. The change in amplitude is caused by a reflected wave as before but in this case the wave has been reflected off the beginning of the damping domain. This becomes most obvious by the time at which the amplitude change occurs. The amplitude change occurs slightly sooner because the wave has been reflected off the beginning of the damping domain rather than the outflow boundary and has therefore had less distance to travel. This shows that there is an optimum value of Z_{GAIN}, above or below which wave reflection and subsequent interference with waves in the main domain can be expected.

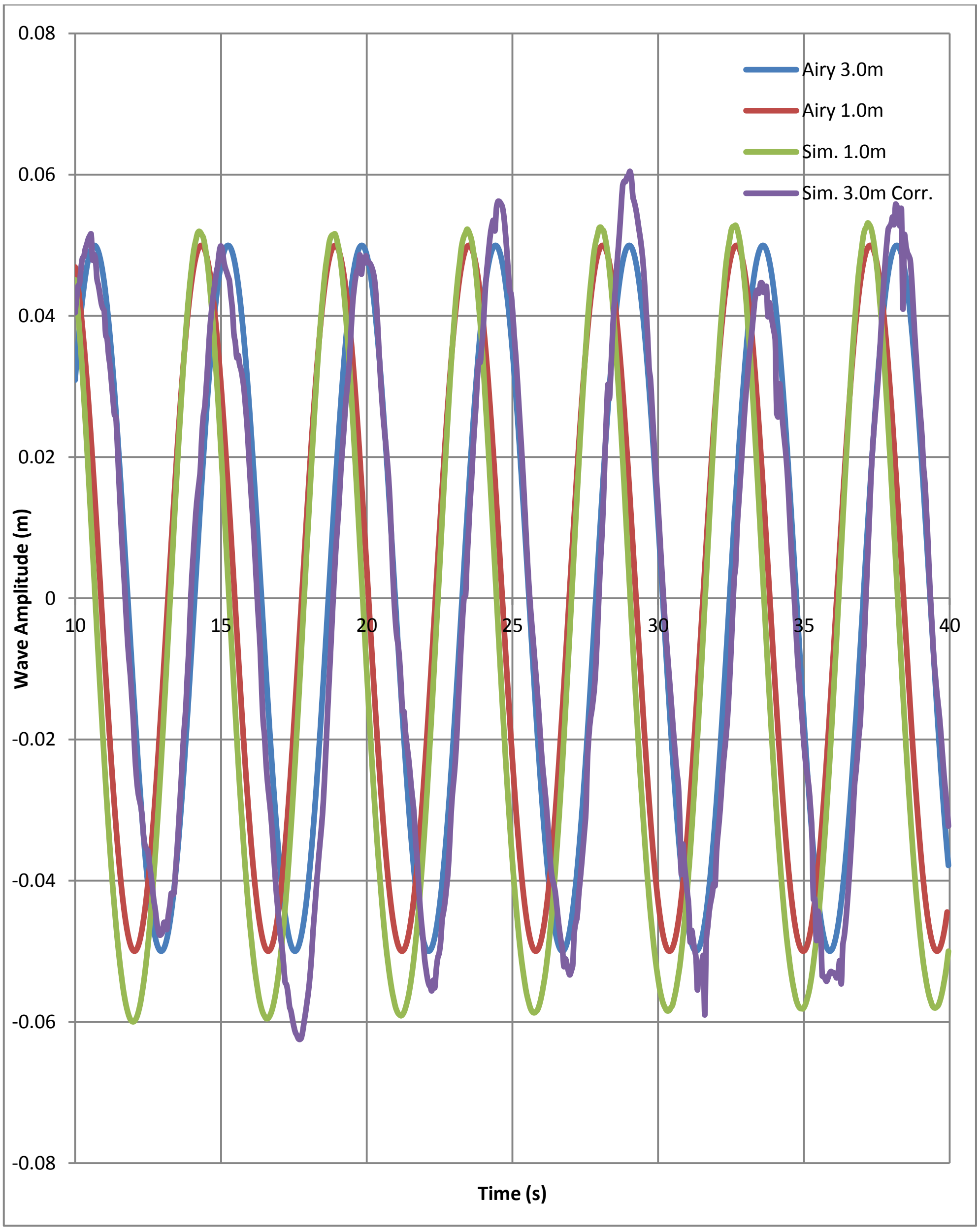

Figure 6.9: Wave propagation test case 6H, $Z_{GAIN} = 100$. This graph demonstrates how the error values shown in figures 6.10 and 6.11 are calculated.

Figure 6.9 shows the results from test case 6H compared to the results predicted by the Airy wave theory. The measuring points used are 1.0m and 3.0m. The simulated and predicted results at 1.0m are very similar as would be expected as the motion of the particles at 1.0m is wholly determined by the Airy wave theory. The comparison between the simulated and predicted results at 3.0m are of more interest as the motion of the particles at 3.0m is determined by the standard SPH equations. One point to note is that although the simulated results are in good agreement with the wave motion predicted by the Airy wave theory for most of the wave, the wave motion at the peak and trough of the wave is not correct. This effect is more pronounced at 3.0m, once the wave has entered the main domain. This discrepancy is probably caused by the time step used during the simulation. The time step is not sufficiently small to fully capture the motion of the particles in the wave maker domain when they are at the peak and trough of the wave, where the acceleration is greatest. This causes the motion of the particles in the wave maker domain to deviate from that predicted by the Airy wave theory as seen in figure 6.9. As the motion of the particles in the wave maker domain is not correct, the motion of the particles in the main domain will also not be correct. This problem could be solved by decreasing the time step used. However, this would cause the time required to complete the simulation to greatly increase.

Figure 6.9 also demonstrates the method by which the results in figures 6.10 and 6.11 are calculated. The measurements taken during the simulation are compared to the results predicted by the Airy wave theory using the following equation:

$$Error = \frac{|Result_{SIM} - Result_{AIRY}|}{a} \times 100 \qquad 6.10$$

Where $Result_{SIM}$ is the maximum particle height measured at the point of interest, $Result_{AIRY}$ is the result predicted by the Airy wave theory and a is the wave amplitude. Once 10 seconds have elapsed, to allow sufficient time for the waves to propagate through the entire wave tank, the error is calculated every 0.05 seconds. The average of the error over the duration of the simulation is then calculated for each test case.

The results for test cases 6A to 6H are presented in figures 6.10 and 6.11. The results in figure 6.10 are measured at 3.0m, The results in figure 6.11 are measured at 3.0m from the end of the wave tank. Clearly the location of the measuring point used in figure 6.11 is dependent on the length of the wave tank used. In the cases where a 6 metre wave tank is used the two measuring points are at the same location. The reason that the second measuring point, located 1.0m from the end of the main domain, is used is to investigate the possibility that larger values of error calculated in the test cases where a shorter wave tank is used could be caused by a reflected wave having to travel less distance. This would cause a wave that has been reflected in a shorter wave tank to be damped out to a lesser extent because the main domain is shorter and therefore the wave damping due to the distance that the wave has travelled, would be less. The reflected wave will cause more interference increasing the error measured at 3.0m when compared with a test case where a longer wave tank was used. However, the wave damping due to propagation will have a greater adverse affect on the error measured as the wave tank length increases. This is because the wave motion has been shown to deviate from that predicted by the Airy wave theory as the wave propagates.

The general trend in both of the figures is that as the value of Z_{GAIN} is increased the error decreases. This trend occurs up to a certain value of Z_{GAIN}, which is dependent on the wave tank length and spatial resolution, above the critical value the error begins to increase. This effect has been discussed previously and is believed to be caused by waves being reflected off the start of the damping domain due to a too high value of Z_{GAIN} being used. The length of the wave tank used evidently has an effect on the error value. The results shown in figure 6.10 show a reduction in the error value as the wave tank length is increased. However, the same pattern is not seen in figure 6.11. In figure 6.11 the results where Z_{GAIN} equals zero show the same pattern as seen in figure 6.10, namely that the error decreases as wave tank length increases; however the error value is greater than that shown in figure 6.10. As Z_{GAIN} is increased the trend in the error measured at 3 metres from the end of the damping domain becomes the opposite of that seen in figure 6.10.

The results show that the error measured at 3.0m for the test cases where a long wave tank is used is lower than for the test cases where a 6 metre wave tank is used. The error measured at 3.0m from the end of the damping domain is greater than for the test cases where a 6 metre wave tank is used. This suggests that when a longer wave tank is used the results measured at 3.0m are lower because the reflected waves have had further to travel and therefore have been damped during the propagation, reducing their ability to interfere with the incoming waves. The results at 3.0m from end of the damping domain suggest that the increase in error with increasing wave tank length is also caused by waves having to propagate further. However, this time the error is mostly caused by the incoming waves deviating from the motion predicted by the Airy wave theory as they propagate.

The results for the 20 metre wave tank in figure 6.10 give the error value where there is very little or no wave reflection interfering with the incoming waves. This is because any reflected wave will have been damped out before it can return to the 3.0m measuring point. The minimum error value for this test case can therefore be taken as the reference point for all other test cases. The minimum error value for test case 6H (20m wave tank, 0.025m spatial resolution) is 11.21%. The minimum error value for test case 6C (6m wave tank, 0.025m spatial resolution) is 18.13%, this shows that the minimum error due to wave reflection in test 6C is 6.92%. In both cases the minimum error values occurred when Z_{GAIN} was 100.

The wave damping mechanism has been shown to be able to minimise unwanted wave reflection by the use of a damping domain. The wave reflection could be completely eliminated by extend the length of the damping domain. However, this would increase the number of particles required and therefore require more computational resources. It should be noted that the length of the damping domain used in these test cases corresponds to 20% of the wavelength.

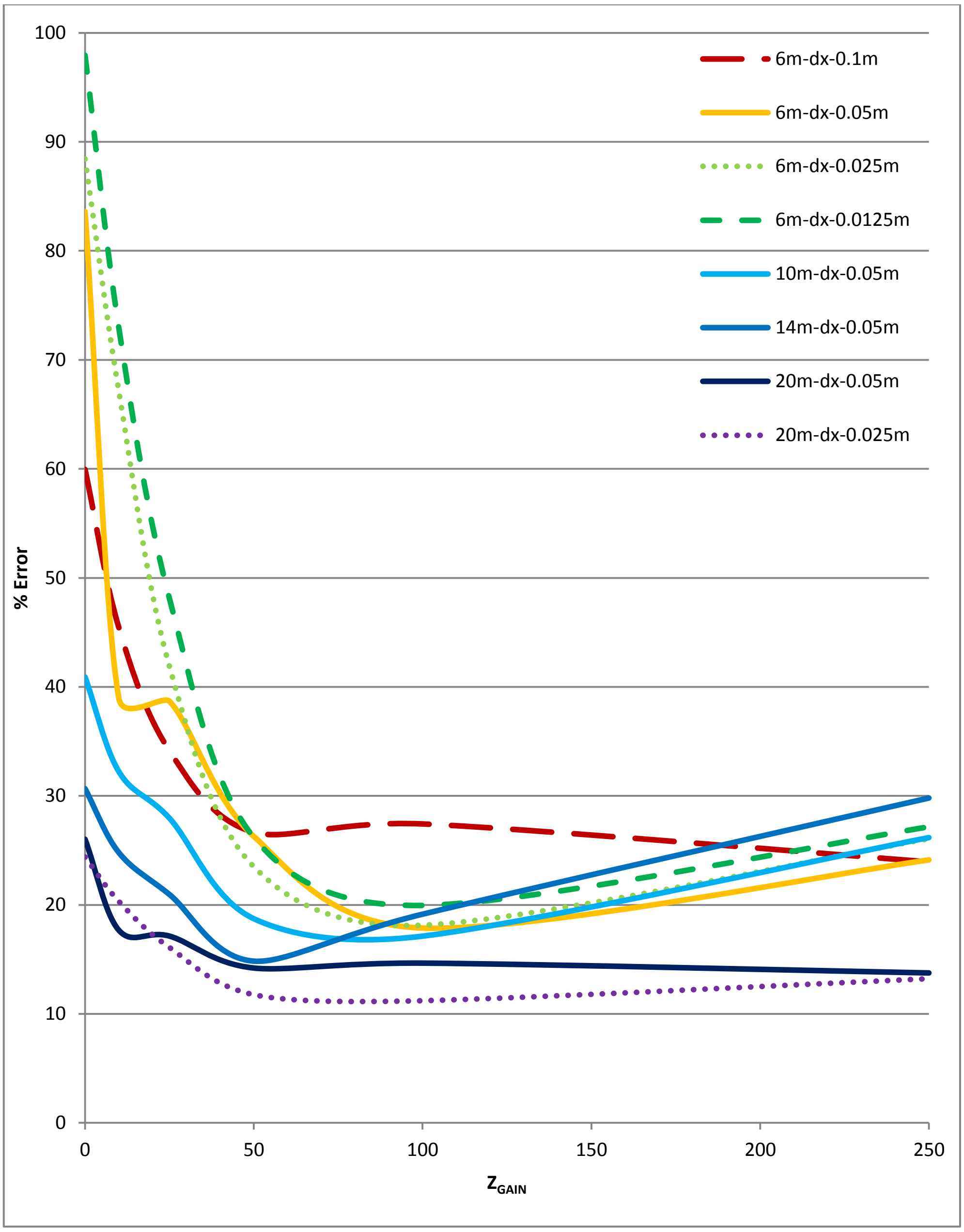

Figure 6.10: Wave propagation test cases 6A-6H. Lines represent the error at 3.0m when compared to the result calculated using the Airy wave theory. The line style indicates the spatial resolution.

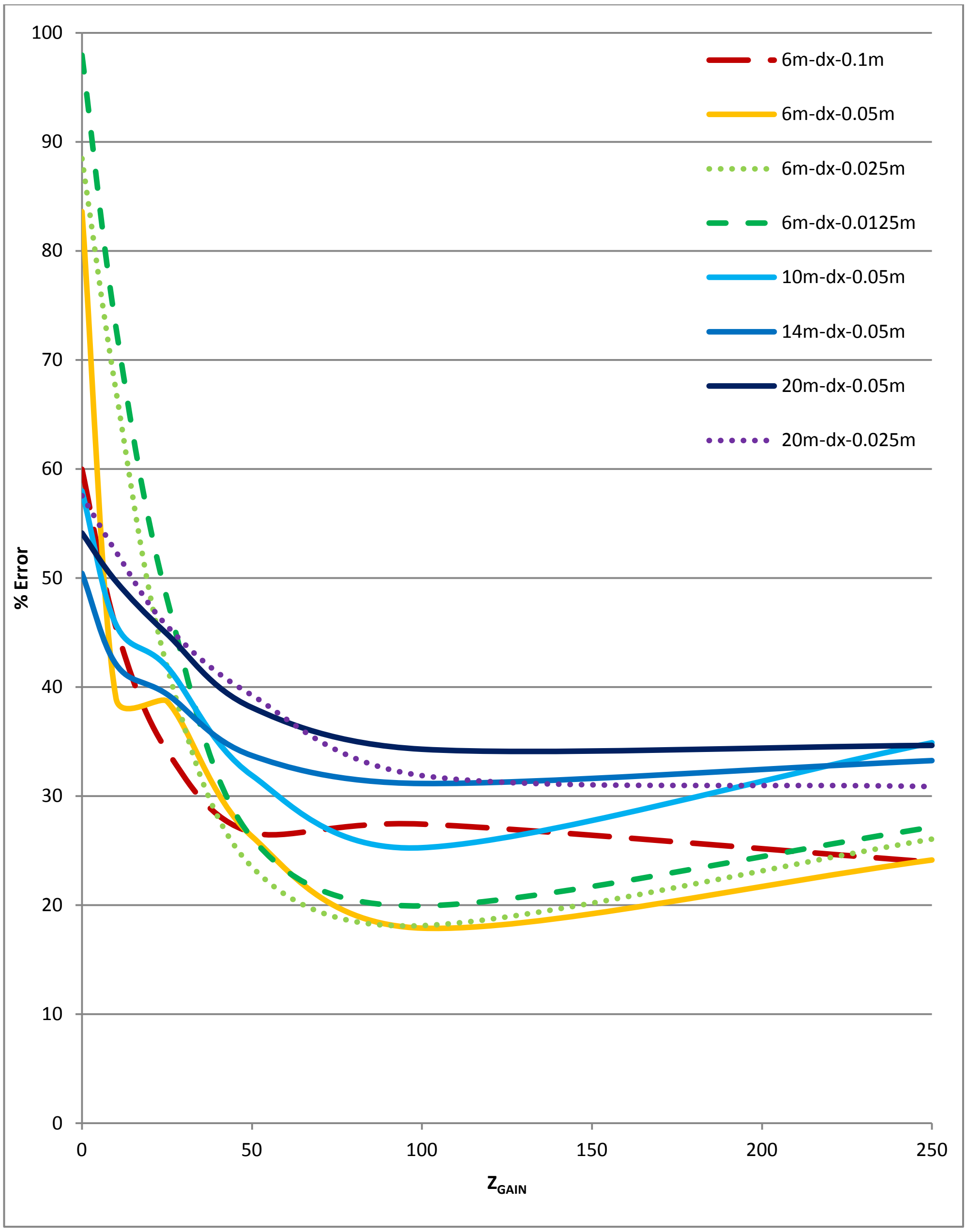

Figure 6.11: Wave propagation test cases 6A-6H. Lines represent the error at 3.0m from the end of the damping domain when compared to the result calculated using the Airy wave theory. The line style indicates the spatial resolution.

6.3.2 - 3D Channel Flow

The second set of test cases discussed in this chapter are designed to test the new wave generation and wave damping mechanisms together in a 3 dimensional situation where there is a mean flow, i.e. a channel flow. For the test cases to be considered successful the following criteria must be met:

- The inflow and outflow boundaries must regulate the flow of particles so that the average free surface height remains constant.
- The waves generated must maintain the correct wave motion, including wavelength and wave amplitude, as the wave propagates along the tank.
- There must be no wave reflection that will interfere with the incoming waves.

The test cases use the maximum particle height measuring system to determine the height of the free surface. However, since these test cases are in 3D the system has been modified. Instead of only searching for particles for a distance *dx* upstream and downstream of the actual measuring point the system is modified to also search for particles cross-stream for a distance *dy* (which equals *dx*) in both directions. The measuring points are at every metre along the wave tank longitudinally and at the centre of the wave tank laterally.

Wave tank length	6.0m
Wave tank width	0.5m
Wave maker domain length	1.0m
Damping domain length	4.0m

Table 6.3: Wave tank dimensions for channel flow test cases.

Test Case	Mean Flow Speed (ms^{-1})	Wave Amplitude (m)
6I	0.75	0.015625
6J	1.0	0.015625
6K	1.0	0.025
6L	1.0	0.03
6M	1.0	0.048
6N	1.5	0.015625
6O	2.0	0.015625
6P	2.0	0.025
6Q	2.0	0.03
6R	2.0	0.048
6S	3.0	0.015625
6T	3.0	0.025
6U	3.0	0.03
6V	3.0	0.048
6W	3.0	0.03125
6X	3.0	0.06

Table 6.4: Channel flow test cases.

Kernel	Gaussian
Time-Stepping	Symplectic
Viscosity Treatment	Full viscosity method
Spatial Resolution	0.05m
Smoothing Distance, h	0.065m
Time Step, dt	0.00025s
Mean Depth	0.5m

Table 6.5: SPHysics inputs for test cases 6I - 6X.

The SPHysics inputs used in these test cases are the same as those used in test cases 6A - 6H and have been chosen for the same reasons as previously discussed. For each test case a wavelength of 3.0 metres is used, this relatively short wavelength has been chosen to determine whether the problems with unwanted wave damping associated with short wavelength waves observed in previous 2 dimensional test cases is also a problem in 3 dimensions. The wave amplitudes 0.025 and 0.048 metres have been chosen as they are the wave amplitudes used in the Wigley hull test cases described in Journée (1992). The other wave amplitudes have been chosen as during the early tests there was a discrepancy between the input wave amplitude used and the wave amplitude measured. It was determined that there is a correlation between the wave amplitude measured and the flow speed used. Therefore the input wave amplitude was varied to try to account for this effect. The flow speeds have been chosen to investigate the effect of using flow speeds that are lower, similar and higher than the phase speed of the wave. The phase speed of the waves in each test case is calculated using equation 5.8 to be 1.91 ms^{-1}.

The results of test cases 6M and 6L are shown in figures 6.12 and 6.13 respectively. The wave amplitude at 1.0m (this measuring point is on the boundary between the wave maker and main domains) shown in figures 6.12 and 6.13 is much greater than the input wave amplitude. This effect was observed in both test cases. However the effect was not observed in either of the previous two sets of test cases where the wave maker system was used. This error in wave amplitude in the wave maker domain is transferred into the main as can be seen in figure 6.12. The wave amplitude at each of the measuring points in the wave domain is approximately 0.08m; approximately 1.6 times the desired wave amplitude of 0.048m.

The difference between this test case and the other test cases, where the wave maker is used, are that the test case is 3D not 2D and that a mean flow is used. As the motion of the particles in the wave maker domain is wholly controlled by the Airy wave equations (i.e. there is no interaction between the particles, as there is in standard SPH) it is impossible that the test case being 3 dimensional would make any difference. As far as the wave maker domain is concerned each sheet of particles in the flow direction can be seen as an individual 2 dimensional sheet, which when placed alongside other sheets creates a 3 dimensional volume. Therefore the most likely explanation for the wave amplitude error is the introduction of a mean flow. To determine whether this is the case a number of different mean flow speeds are used.

To correct for the wave amplitude error in test case 6M the input wave amplitude used in test case 6L is 0.03m (1.6 times smaller than the input wave amplitude used in test case 6M). The results for test case 6L are shown in figure 6.13. The wave amplitude measured at 1.0m is still much greater than the input wave amplitude. However, the wave amplitudes measured at the measuring points in the main domain are now much closer to the desired value.

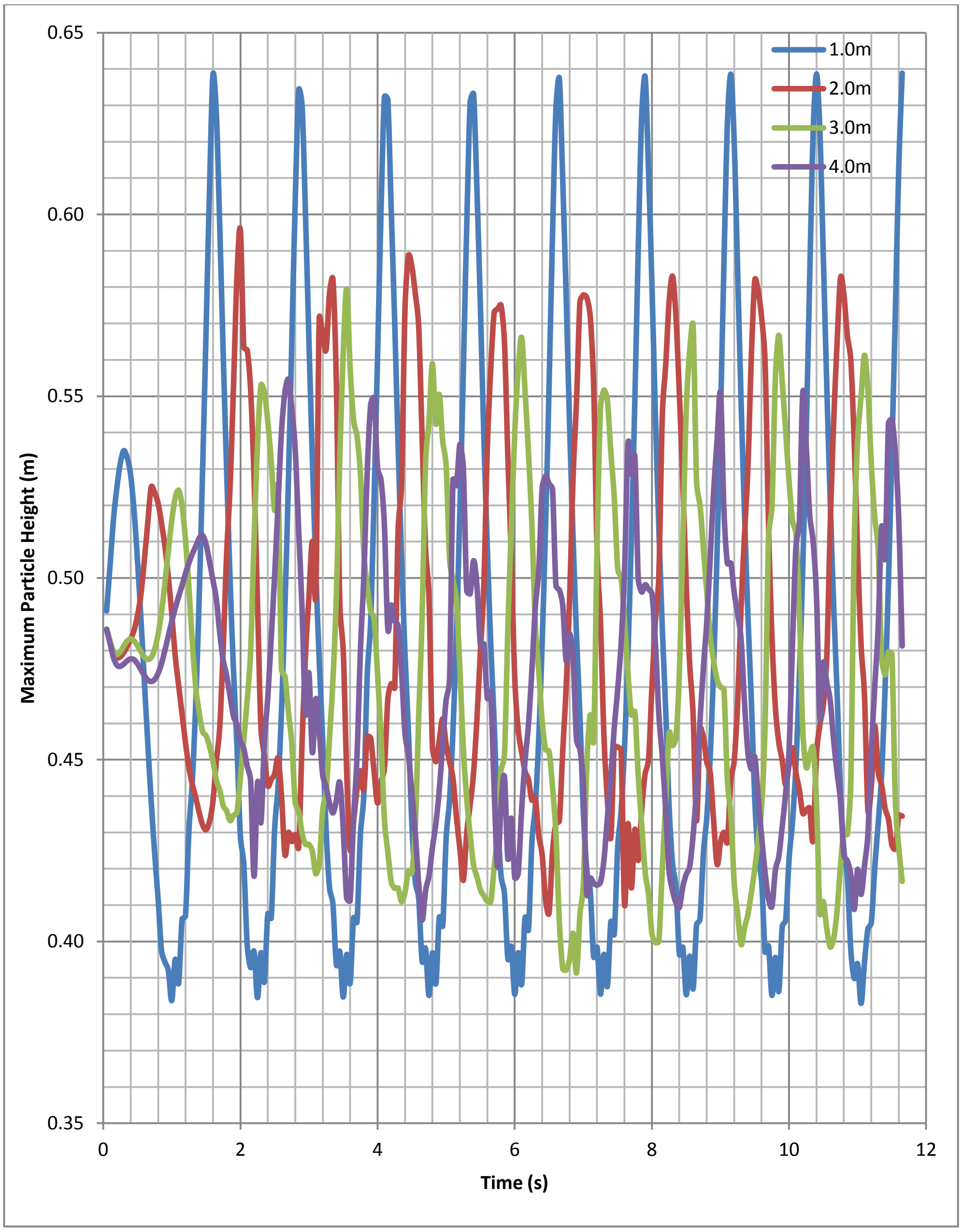

Figure 6.12: Test case 6M. 1.0ms^{-1} flow speed, 0.048m wave amplitude. The lines indicated the maximum particle height measured at each measuring point.

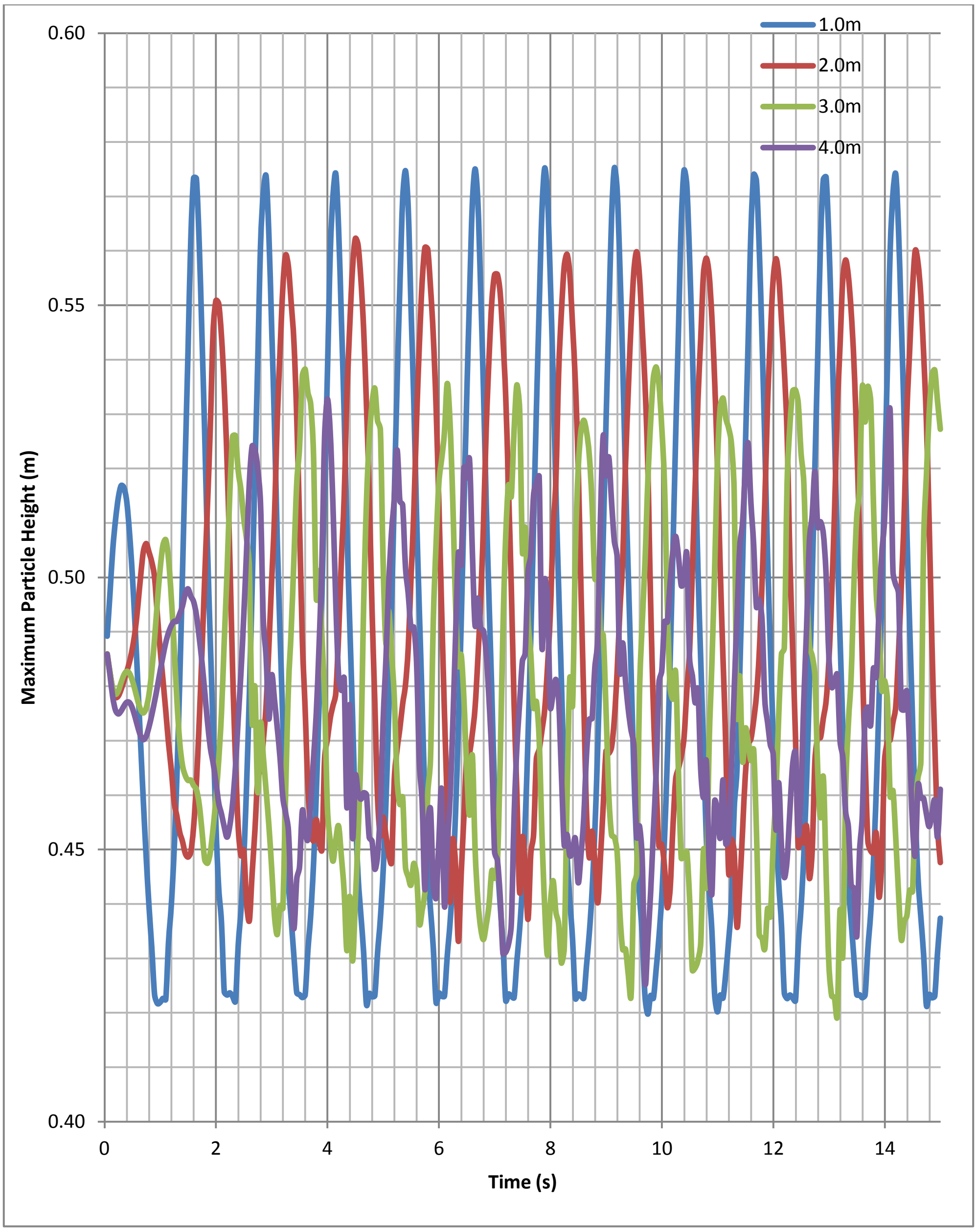

Figure 6.13: Test case 6L. 1.0ms^{-1} flow speed, 0.03m wave amplitude. The lines indicated the maximum particle height measured at each measuring point.

The discrepancy between the input wave amplitude and the wave amplitudes measured in the main domain that was observed in test case 6M (and to which a solution was tested in test case 6L) was also observed in other test cases. The output for each test case is a comparison of the wave amplitude measured at 2.0, 3.0 and 4.0 metres (the measuring points in the main domain) with the input wave amplitude (therefore a result of 1 means the measured wave amplitude is correct). The results for test cases 6I - 6X are shown in table 6.6.

		Wave Amplitude, a (m)					
Mean Flow Speed, U (ms^{-1})		0.015625	0.025	0.03	0.048	0.03125	0.06
	0.75	0.8					
	1	1	1.6	1	1.6		
	1.5	1					
	2	0.6	1	0.6	1		
	3	0.6	0.8	0.42	0.8	0.9	1

Table 6.6: Results for test cases 6I - 6X. Green fill columns represent results where the wave amplitude are those used in Journée (1992).

As can be seen in table 6.6 the results for the 0.025m and 0.048m standard wave amplitude test cases show that the error in wave amplitude is dependent on the mean flow speed. When the flow speed is $2.0\mathrm{ms}^{-1}$ the wave amplitude is correct (the phase speed of the waves generated by the wave maker is $1.91\mathrm{ms}^{-1}$). However, when the mean flow speed is less than the wave phase speed the measured wave amplitudes are greater than the input wave amplitude. Conversely when the mean flow speed is greater than the wave phase speed the measured wave amplitudes are less than the input wave amplitude.

To attempt to correct the error in measured wave amplitude observed in the 0.025m and 0.048m standard wave amplitude test cases further test cases have been conducted. For test cases where the mean flow speed is $1\mathrm{ms}^{-1}$ (test cases 6K and 6M) using the correct input wave amplitude gives a measured wave amplitude 1.6 times greater than the input wave amplitude. To correct this an input wave amplitude 1.6 times less is used in test cases 6J and 6L. As can be seen in table 6.6 the measured wave amplitude in test cases 6J and 6L is correct. The results for test cases 6I and 6N also show that reducing the input wave amplitude used in these test cases results in the measured wave amplitude being correct.

The results for test cases 6P and 6R (where the mean flow speed is $2\mathrm{ms}^{-1}$) show that no correction to the input wave amplitude is required as the measured wave amplitude is already correct. Test cases 6O and 6Q show what happens if a input wave amplitude reduction of 1.6 times (as used in the lower mean flow speed test cases) is used. As would be expected the measured wave amplitude is reduced by approximately 1.6 times. Test cases 6S - 6X use a mean flow speed of $3\mathrm{ms}^{-1}$. Test cases 6T and 6V use the standard wave amplitude input values. The measured wave amplitudes in both test cases is 1.25 times less than the input value.

Therefore test cases 6W and 6X use input wave amplitudes 1.25 times greater than the standard input wave amplitudes. The results for these test cases again demonstrate that this correction in the input wave amplitude gives the correct measured wave amplitudes. Test cases 6S and 6U test whether reducing the input wave amplitude by 1.6, compared to the standard input wave amplitude, would produce a corresponding reduction in the measured wave amplitude as had been observed in the previous test cases. However the measured wave amplitude in test case 6S is only 1.3 times less than the measured wave amplitude in test case 6T. A similar discrepancy is observed in the results for test case 6U where the measured wave amplitude is 1.9 times less than the measured wave amplitude in test case 6V.

6.4 - Conclusions

A new two part wave damping mechanism has been developed and integrated into the SPHysics framework. Test cases have been conducted in 2 dimensions and 3 dimensions the wave damping mechanism has been shown to be effective. The 2 dimensional test cases have shown that the sponge layer wave damping mechanism is capable of damping out waves sufficiently to prevent any significant wave reflection interfering with the wave motion in the main domain. The sponge layer could be made even more effective by extending the length of the damping domain, but this comes at a price as it would increase the number of particles and therefore the computational effort required to complete the simulation. The value of the damping tuning coefficient, Z_{GAIN}, has been shown to have an optimum value. If the value of Z_{GAIN} is too low then wave reflection off the boundary will occur. If the value of Z_{GAIN} is too great then wave reflection off the damping domain will occur.

The 3 dimensional channel flow test case tests the effectiveness of both parts of the new wave damping mechanism. However, an unexpected problem with the wave maker system described in the previous chapter has arisen. This problem occurs because a mean flow is used, the wave amplitude measured in the main domain differs from the input wave amplitude. The problem is dependent on the value of the mean flow speed and the phase speed of the waves being generated.

If the mean flow speed and the wave phase speed are similar then the problem does not occur. If the mean flow speed is lower than the wave phase speed then the amplitude of the waves that are generated will be greater than the input wave amplitude. Conversely, if the mean flow speed is greater than the wave phase speed then the amplitude of the waves that are generated will be lower than the input wave amplitude. To resolve this problem the input wave amplitude was adjusted to account for the error in the amplitude of the waves that were generated.

Chapter 7

Wigley Hull Test Cases

7.1 - Introduction

In preceding chapters the necessary new methodologies that are required to allow SPHysics to be used to simulate a wave tank have been discussed. Now that a wave tank can be simulated the next step is to simulate a ships' hull in that wave tank. The simulations involve using the previously discussed methodologies to model the wave tank. The floating body mechanism that is included within SPHysics is modified to model a ships' hull. The simulations described in this chapter are based upon the experiments conducted in Journée (1992).

The experiments conducted in Journée (1992) concern a series of experiments that take measurements of the forces and motions of a Wigley hull that is subjected to regular head waves. Although the paper outlines a number of different experiments there are two that have been chosen to be simulated in this chapter. The first is where the hull is restrained, the heave and surge forces and the pitching moments are measured. The second is where the hull is free to heave and pitch only and these motions are measured.

7.2 - Methodology

The new methodologies presented in this chapter concern the modelling of the Wigley hull. The Wigley hull is a hull form that is commonly used in validation experiments and simulations. The hull is symmetrical about its longitudinal and lateral axes. The shape of the hull is defined by the following equation:

$$\eta = \left(1-\zeta^2\right)\left(1-\iota^2\right)\left(1+a_2\iota^2+a_4\iota^4\right)+\alpha\zeta^2\left(1-\zeta^8\right)\left(1-\iota^2\right)^4 \tag{7.1}$$

Where the origin is located at the centre of the ship longitudinally and laterally, the vertical origin is located at the still water line. ι is the longitudinal axis (positive forwards, $-1 \leq \iota \geq 1$), η is the lateral axis (positive to port) and ζ is the vertical axis (positive downwards, $0 \leq \zeta \geq 1$). ι, η and ζ are multiplied by $WH_l/2$, $WH_b/2$ and WH_d respectively to give the dimensional hull form (WH_l is the length of the hull, WH_b is the breadth of the hull and WH_d is the draught of the hull). The geometry of the hull below the still waterline is described by equation 7.1, above the still waterline the sides of the hull are vertical. Four different Wigley hulls are used in Journée (1992), these are determined by the variables a_2, a_4 and α in equation 7.1. The Wigley hull used in the simulations described in this chapter is Wigley hull III. This hull has been chosen because it has a narrow breadth which will cause less blockage in the wave tank tests.

The hull is modelled in SPHysics by modifying the floating body mechanism that is already in place in SPHysics. However, the default floating body mechanism is only capable of modelling simple objects. The mechanism is modified so that the geometry that is generated during the initialisation is that of the Wigley hull. The particles that make up the hull are placed according to equation 7.1. The hull is split into sections longitudinally and vertically, evenly spaced along the length and height of the hull. As the longitudinal and vertical position of each particle has been decided equation 7.1 is used to calculate the lateral position with two particles being placed (one on the port side and one on the starboard). The geometry described thus far has generated the two halves of the sides of the hull. Further particles are placed at the top of the hull to create a flat upper surface. Water particles that would be placed inside or very close to the hull are removed from the simulation to prevent the simulation crashing once the simulation has begun.

The mass of the hull is determined by simulation with varying masses until the hull rests in the water with the waterline at the correct point on the hull. The moment of inertia about the lateral axis is given in Journée (1992). The moments of inertia about other axes are irrelevant as the experiments do not allow motion about either of these axes. The values of the volume of displacement, centre of rotation and centre of gravity are given in Journée (1992).

A problem found when conducting the simulations was that the simulation would frequently crash very soon after the simulation was begun. This problem was caused by fluid particles which begun the simulation very close to the hull. As the fluid particles are given an initial velocity equal to the mean flow speed this allowed for some fluid particles to get too close to the hull particles and therefore experience a very large repulsive force. This caused the fluid particles to be accelerated very rapidly, causing the simulation to crash. Although not tested, a solution to this problem would be to allow the flow to accelerate from rest instead of imposing an initial flow speed equal to the mean flow speed. However this solution is not desirable as it would increase the amount of time and therefore computational resources required to complete each simulation.

Another way to solve this problem was to decrease the time step. This would of course increase the computational resources required to complete the simulation. A further solution that does not require the time step to be reduced was devised. The distance between the fluid and boundary particles (q) used in equation 3.26 was limited to a minimum value of 0.01 to prevent the large repulsive forces being imposed. This allowed for the simulation to be commenced without the need to accelerate the flow and without resorting to the crude approach of reducing the time step.

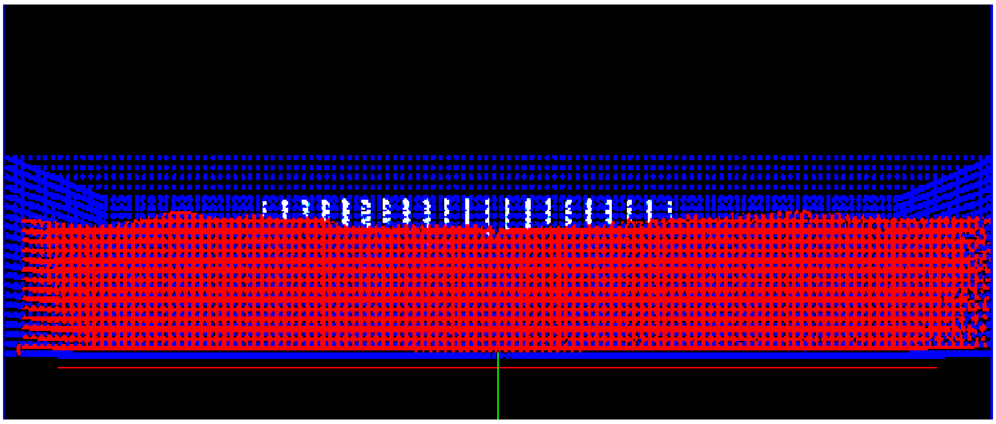

Figure 7.1: Side view of the simulated Wigley hull in the wave tank.

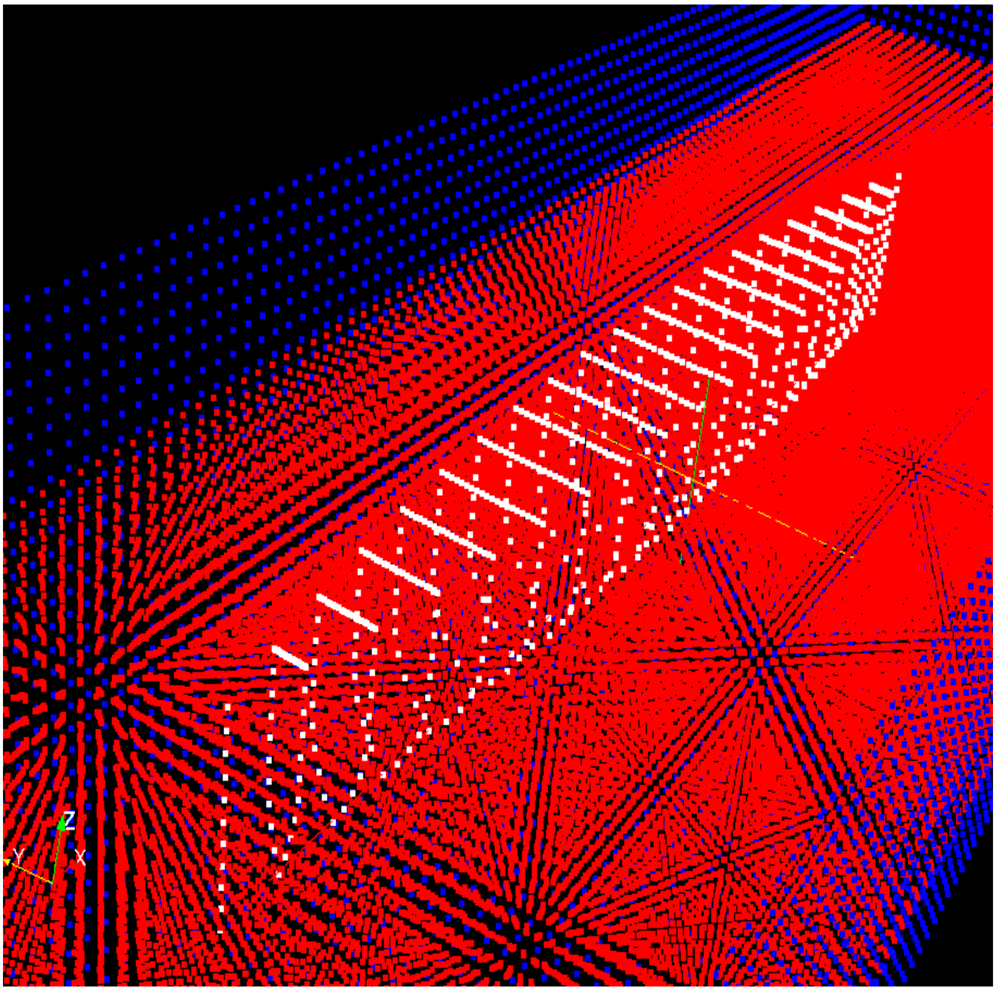

Figure 7.2: Close-up of the Wigley hull in the wave tank.

7.3 - Experiments

The experiments presented in Journée (1992) were chosen to validate the use of the modified SPHysics framework to simulate a Wigley hull in a wave tank. These experiments concern simulating a restrained Wigley hull that is subjected to head waves with a mean flow speed and a similar set of experiments where the Wigley hull is allowed to pitch and heave only. Table 7.1 shows the wave tank geometry used in both sets of simulations.

Wave tank length	6.5m
Wave tank width	1.8m
Wave tank height	1.0m
Water depth	0.7m
Wave maker domain length	1.0m
Damping domain length	1.5m

Table 7.1: Wave tank geometry.

The dimensions of the wave tank have been chosen to allow the simulations to be run with the maximum amount of particles that can be used by the single central processing unit (CPU) version of SPHysics. In such idealisation the wave maker domain length allows the waves that are being generated to fully form before they enter the main domain. For this reason the main domain does not need to be much longer than the length of the Wigley hull. The length of the hull is 3m and the main domain is of length 4m. The hull is placed in the middle of the main domain (both longitudinally and laterally). The width of the wave tank has been chosen to minimise the blockage effect that the hull will cause. The width of the wave tank is six times greater than the breadth of the hull. Having established the length and width of the wave tank the depth of the water is chosen to be as large as possible without the number of particles exceeding the maximum allowable number.

The geometry of the Wigley hull is shown in table 7.2 and is also common to both sets of simulations. The hull used is referred to as Wigley hull III in Journée (1992). With the exception of the mass of the hull and the moment of inertia for pitch (which is dependent on the mass of the hull) all of the variables in table 7.2 are defined in Journée (1992). The mass of the hull is determined by running simulations to determine the correct value that causes the waterline of the hull to be in the correct place in relation to the free surface.

Hull length, WH_l	3.0m
Hull breadth, WH_b	0.3m
Hull draught, WH_d	0.1875m
Volume of displacement, WH_v	0.0780m^3
Total volume of hull	0.3m^3
Centre of rotation above keel	0.1875m
Centre of gravity above keel	0.17m
Radius of inertia for pitch, k_{yy}	0.75m
Mass of hull, m	93.75kg
Moment of inertia for pitch, I_{yy}	52.73kgm^2

Table 7.2: Wigley hull geometry.

Kernel	Gaussian
Time-Stepping	Symplectic
Viscosity Treatment	Full viscosity method
Spatial Resolution	0.05m
Smoothing Distance, h	0.065m
Time Step, dt	0.001s

Table 7.3: SPHysics inputs for all Wigley hull test cases.

The Gaussian kernel was used in these simulations for the same reason that it is used in the simulations described in chapter six, namely that whilst the Wendland kernel would be preferred it will not allow the simulations to run with a reasonable time step. The reasons behind the choice of time-stepping and viscosity treatment have been discussed in previous chapters. The spatial resolution has been chosen as the dimensions of the hull are already prescribed in Journée (1992) and therefore the spatial resolution has to be proportional to the size of the hull to ensure the correct number of particles. The time step is chosen as the largest time step that will ensure that each simulation will not crash.

7.3.1 - Restrained Hull

The restrained hull simulations are conducted to allow the forces and moments exerted on the Wigley hull to be measured. The forces that are measured are the surge and heave forces, the measured moment is the pitch moment. Each of these measurements are taken 100 times per second. The main variables for each of the test cases are the wavelength, wave amplitude and mean flow speed; these variables are shown in table 7.4. The input wave amplitude is corrected in test cases 7A and 7B as the mean flow speed in these test cases is low, the correction factor has been obtained from the results from chapter 6. As the mean flow speed in test case 7C is 2.17ms^{-1}, which is similar to the flow speed that required no correction to the input wave amplitude, no correction has been applied. Note that the original wave amplitude and not the corrected wave amplitude is used in equations 7.2, 7.3 and 7.4. In each test case seven separate simulations were conducted. The wavelength was varied in each of these simulations. The wavelengths used are 1.5m, 2.25m, 3.0m, 3.75m, 4.5m, 5.25m and 6.0m. The simulations were run for between 10 and 20 seconds.

Test Case	Mean Flow Speed, U (ms^{-1})	Wave Amplitude, a (m)	Corrected Wave Amplitude (m)
7A	1.085	0.025	0.15625
7B	1.085	0.048	0.03
7C	2.17	0.025	0.025

Table 7.4: Restrained hull test cases.

For both flow speeds simulations were conducted with no waves to determine the forces and pitching moments exerted by the mean flow on the hull. These results were used to correct the forces and pitching moments measured during the simulations with waves by subtracting the results with no waves from the results with waves.

The heave force is measured and then non-dimensionalised according to the following equation:

$$X_{w3a}" = \frac{X_{w3a}}{a \times C_{33}} \tag{7.2}$$

Where $X_{w3a}"$ is the non-dimensionalised heave force, X_{w3a} is the maximum corrected heave force measured over a period of time (positive upwards), a is the wave amplitude and C_{33} is a static coefficient (6119 Nm^{-1} for Wigley hull III). The surge force is measured and then non-dimensionalised according to the following equation:

$$X_{w1a}" = \frac{X_{w1a}}{k \times a \times \rho \times g \times W H_v} \tag{7.3}$$

Where $X_{w1a}"$ is the non-dimensionalised surge force, X_{w1a} is the maximum corrected surge force measured over a period of time (positive forwards), k is the angular wavenumber (see equation 5.1), ρ is the density of water, g is the acceleration due to gravity and WH_v is the volume of displacement of the hull. The pitching moment is non-dimensionalised according to the following equation:

$$X_{w5a}" = \frac{X_{w5a}}{k \times a \times C_{55}} \tag{7.4}$$

Where $X_{w5a}"$ is the non-dimensionalised pitching moment, X_{w5a} is the maximum corrected pitching moment measured over a period of time (positive upwards) and C_{55} is a static coefficient (2874 Nm^{-1} for Wigley hull III). The measurements are taken once regular waves are established throughout the domain.

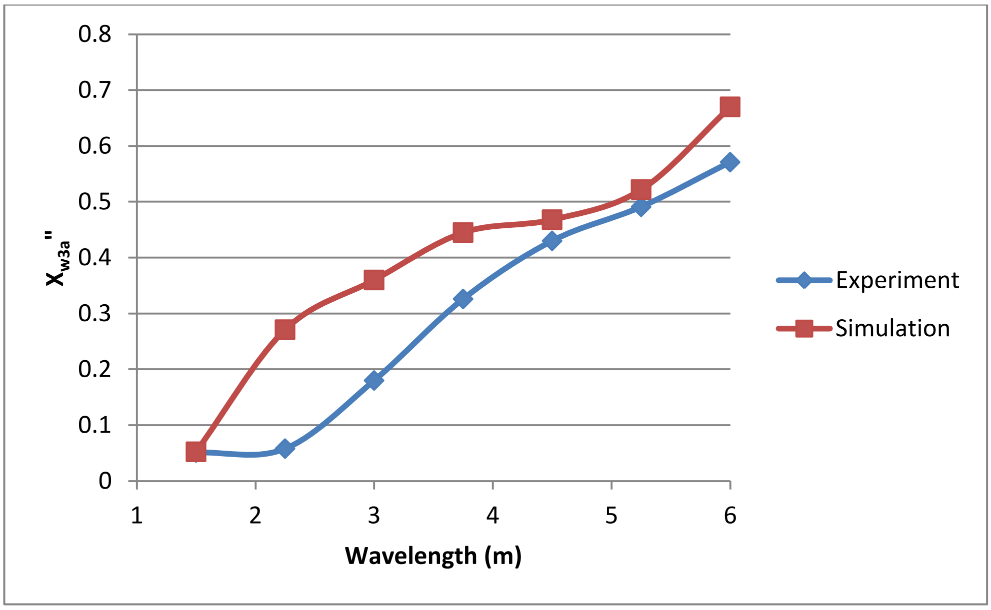

Figure 7.3: Test case 7A, heave force measurements.

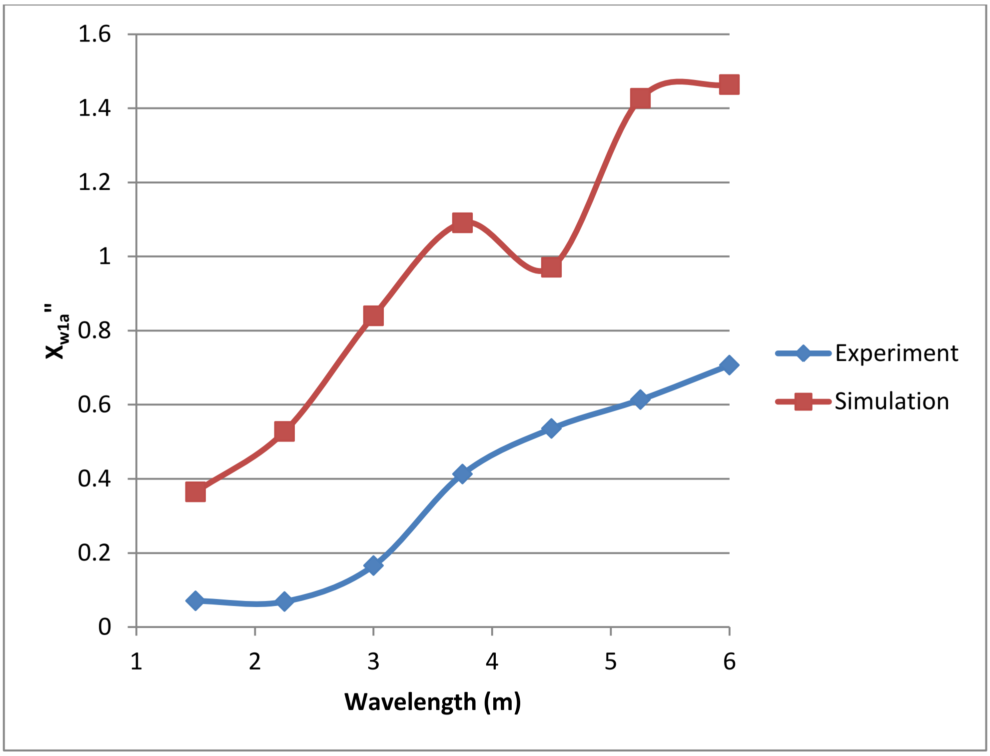

Figure 7.4: Test case 7A, surge force measurements.

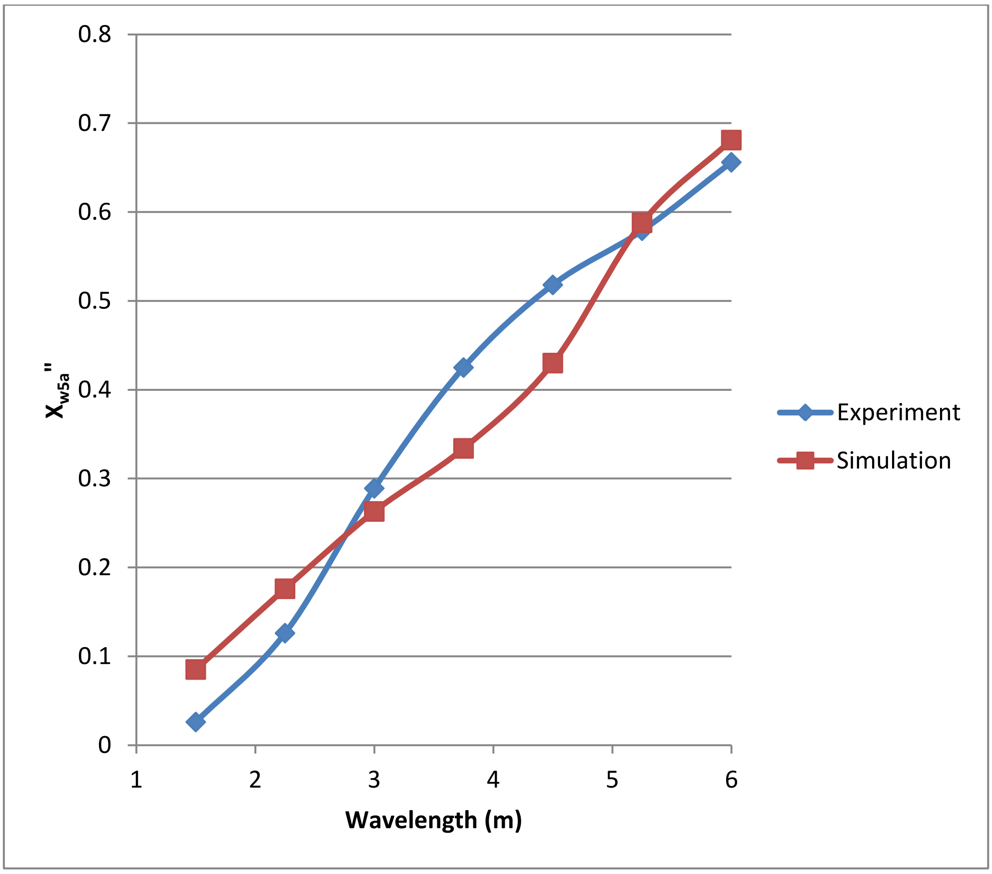

Figure 7.5: Test case 7A, pitching moment measurements.

Figures 7.3, 7.4 and 7.5 show the results from test case 7A. Both the heave force and pitching moment simulation results show agreement with the trend in the experimental results. However, the heave force simulation results give greater values than the experimental data for all but the shortest wavelength. The surge force simulation results do not show good agreement with the simulation results, the trend is correct but the maximum measured force is consistently much greater than that in the simulation results for all wavelengths.

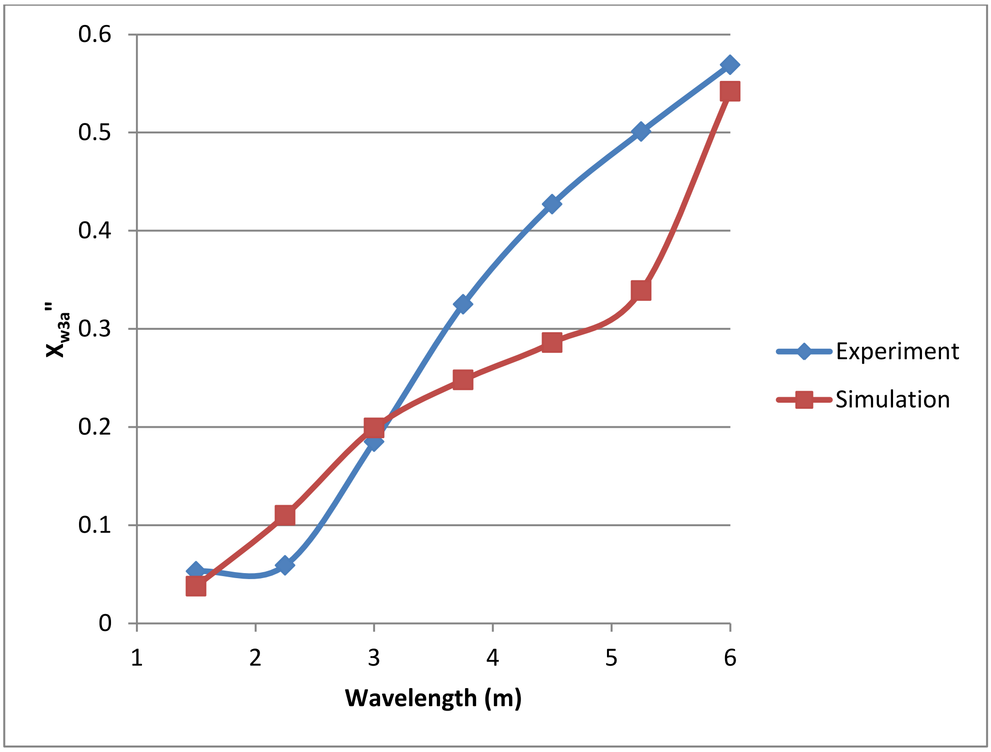

Figure 7.6: Test case 7B, heave force measurements.

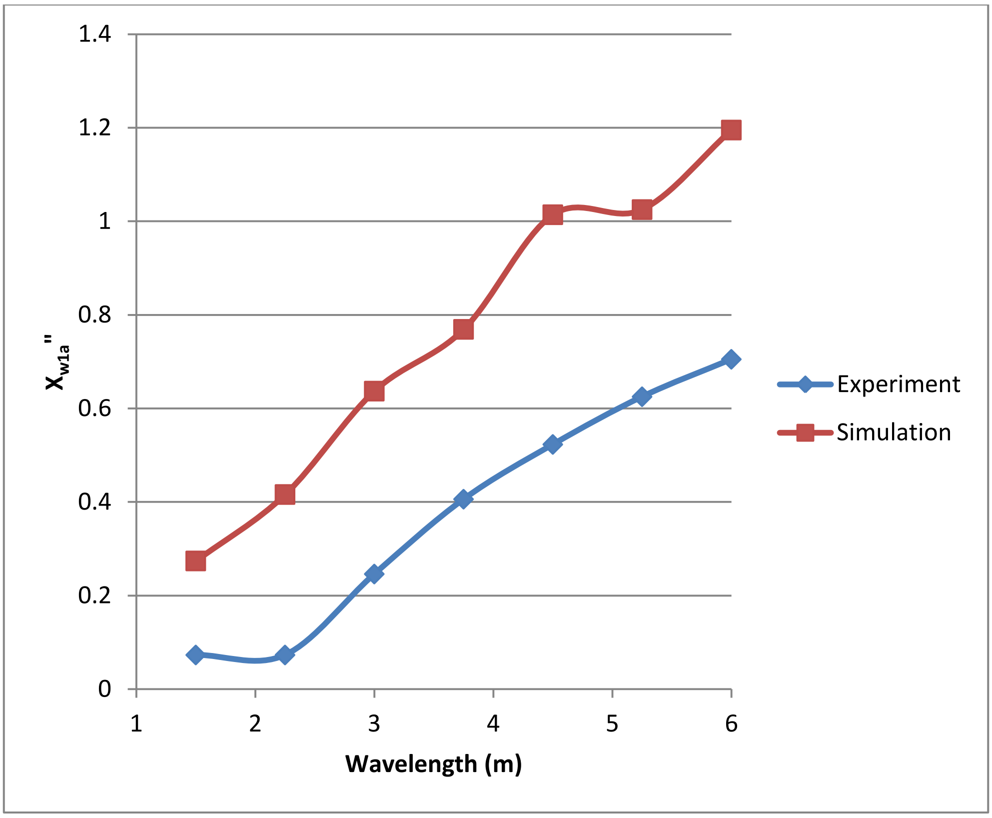

Figure 7.7: Test case 7B, surge force measurements.

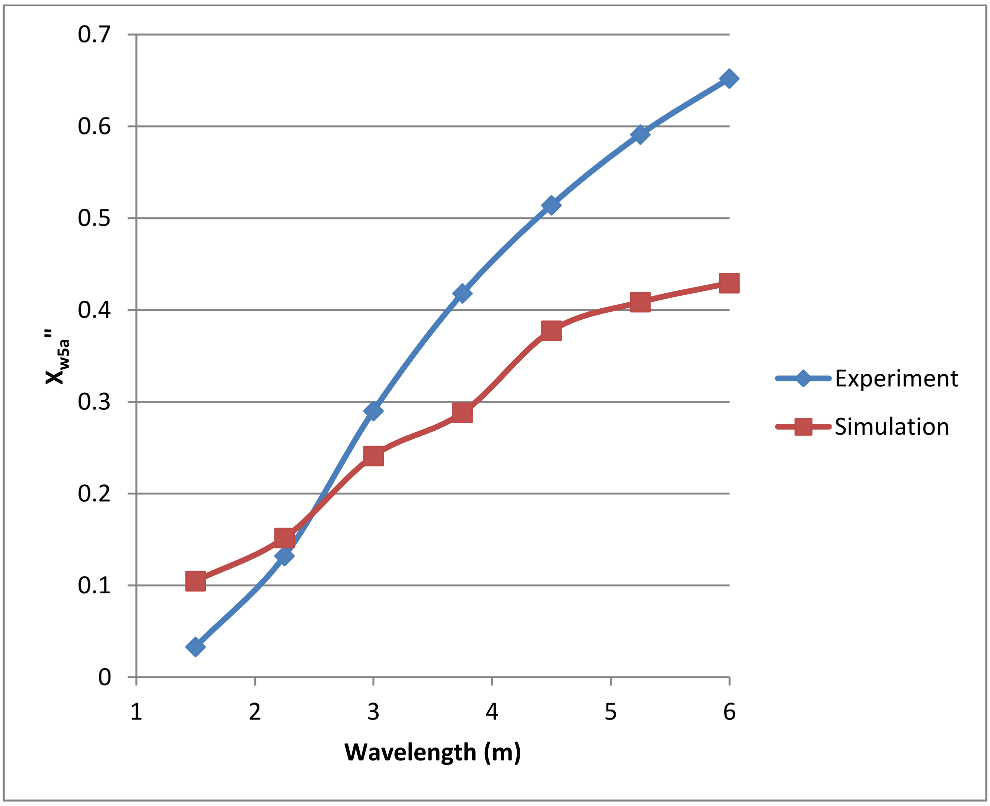

Figure 7.8: Test case 7B, pitching moment measurements.

Figures 7.6, 7.7 and 7.8 show the results from test case 7B. The surge force and pitching moment measurements results show good agreement with the experimental results at the lower wavelengths. However, as the wavelengths increase the simulations results for both measurements are lower than the experimental results. If simulations were conducted where the hull was allowed to move then the results for this test case indicate that at the higher wavelengths the heave and pitching motion would be smaller than in the experimental data. The surge force measurements show the same result as observed in test case 7A. The trend in the simulation results is similar to that in the experimental data. However, the surge force values are consistently over-predicted.

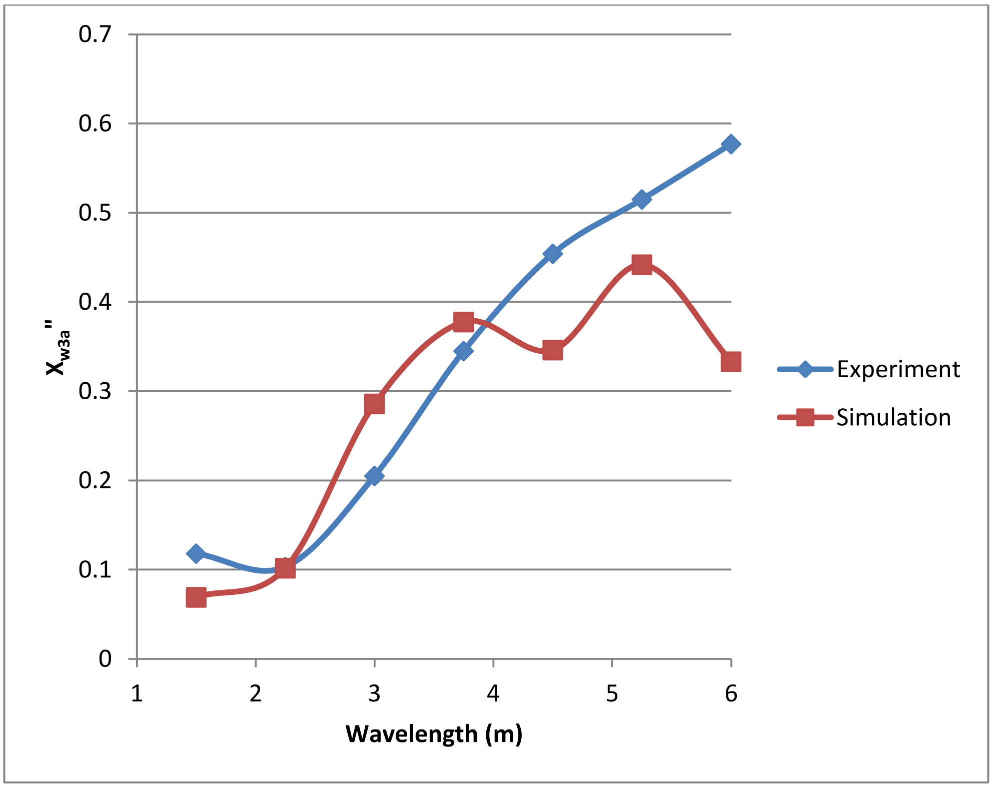

Figure 7.9: Test case 7C, heave force measurements.

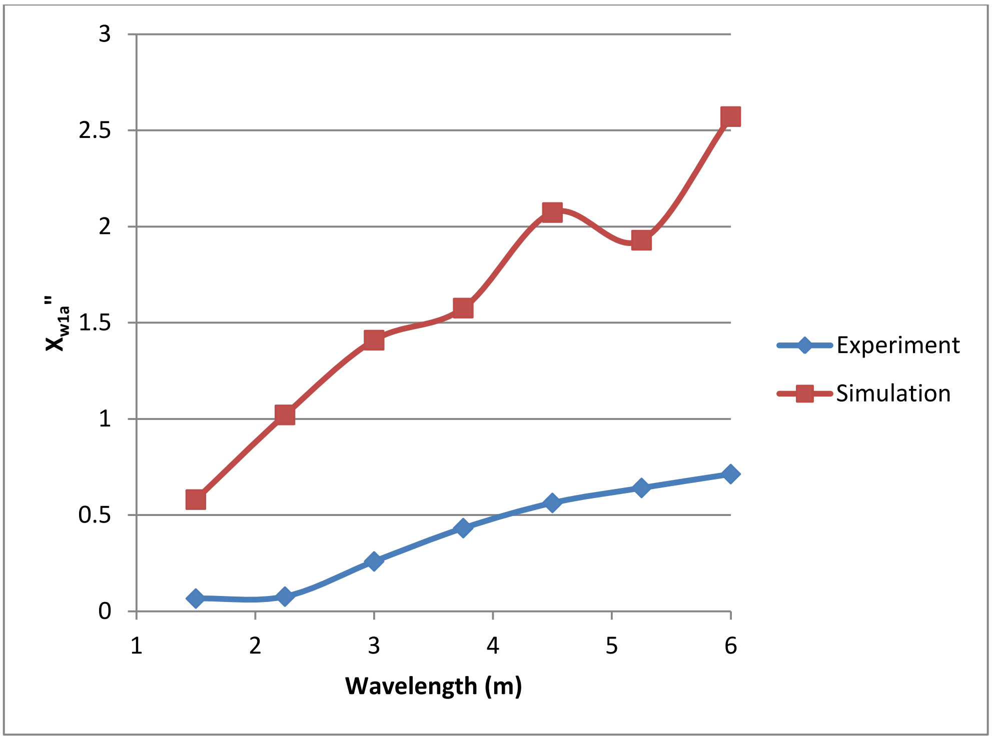

Figure 7.10: Test case 7C, surge force measurements.

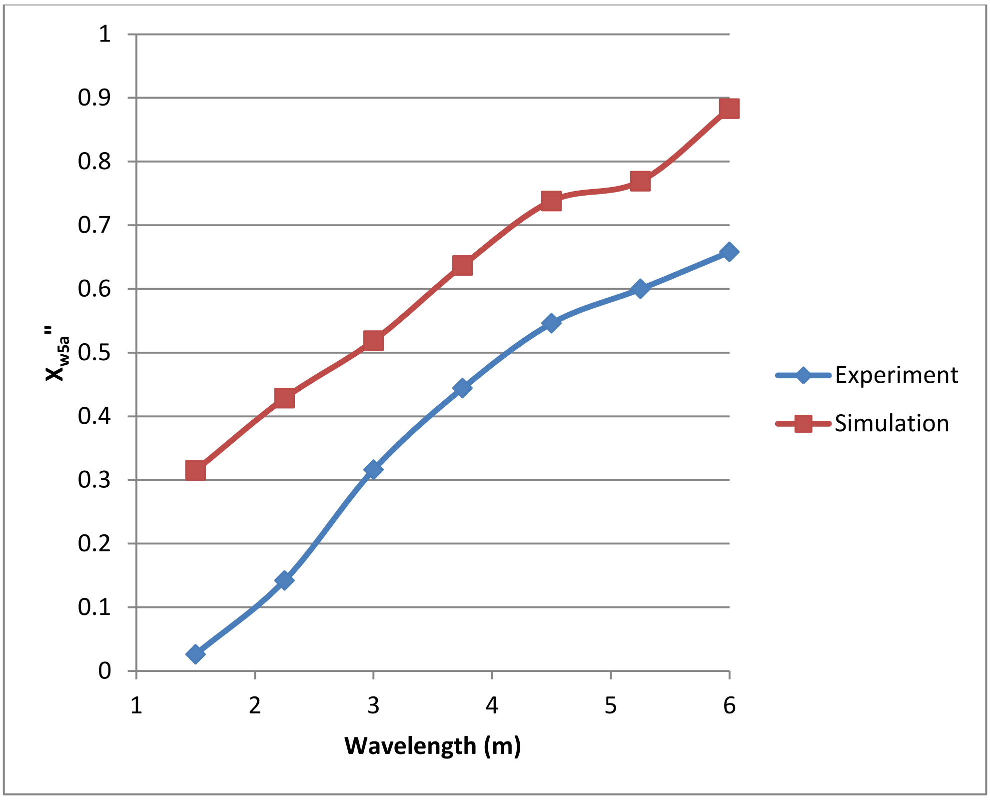

Figure 7.11: Test case 7C, pitching moment measurements.

Figures 7.9, 7.10 and 7.11 show the results for test case 7C. As with the previous two test cases the heave force simulation results show reasonable agreement with the experimental results. However, as was the case in test case 7B as the wavelength is increased the heave force measurements are under-predicted. The surge force measurements show the same trend as seen in the previous two test cases. However, unlike test cases 7A and 7B (where the mean flow speed was 1.085ms^{-1}) the pitching moment measured in test case 7C simulations is much greater than the experimental results. The gradient of the pitching moment measurements is very similar to the gradient of the experimental results. This is an unexpected result as the pitching moment is created by the vertical force acting on the hull, which is also responsible for creating the heave force, the results for which are much closer to the experimental results.

If the maximum pitching moment is greater than expected then this must be caused by a large heave force acting on the front half of the hull and a smaller heave force acting upon the rear half of the hull. Overall this balances out to give the correct heave force. This can be seen in the screenshot shown in figure 7.12, a very large bow wave can be seen which persists throughout the simulation. It is this bow wave that is causing the large upwards pitching moment. This bow wave was not observed in any of the simulations conducted for test cases 7A and 7B where the mean flow speed was 1.085ms^{-1}. It is clear that the greater mean flow speed is causing this problem.

It is also possible that the width of the wave tank is too small. The blockage caused by the hull causes the free surface to rise around the front half of the hull. Again this effect would be more pronounced when the mean flow speed is greater. Due to the limitation on the number of particles in the single central processing unit version of SPHysics the width of the wave tank cannot be increased.

The results of these restrained hull simulations show that the modified SPHysics framework is capable of calculating the heave force and pitching moment on the hull. A problem with the measured pitching moment when the mean flow speed is increased was observed. The results for the surge force measured during the simulations were poor. However, the hull is not permitted to surge in the simulations in the second section of this chapter so this should not cause further problems.

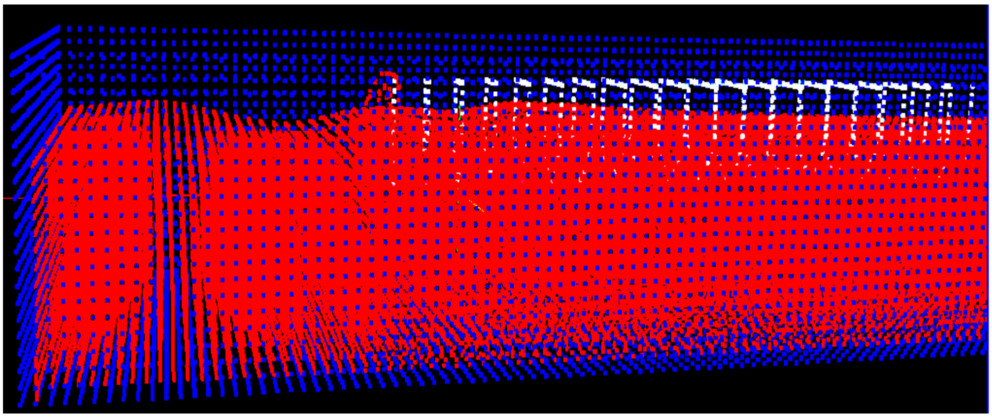

Figure 7.12: Screenshot of large bow wave generated with a mean flow speed of 2.17ms^{-1}.

7.3.2 - Semi-Free Hull

The semi-free hull simulations are so called as the hull is free to move in the heave axis and free to rotate about the pitching axis only. The position and angle of the hull is measured 100 times per second. As in the previous test case the main variables for each test case are the wavelength, wave amplitude and mean flow speed; these variables are shown in table 7.5. As with the fixed hull simulations the input wave amplitude is corrected as per the recommendations made in chapter 6. The original wave amplitude is used in equations 7.5 and 7.6. In each test case seven separate simulations were conducted, the wavelength is varied in each of these simulations. The wavelengths used are 1.5m, 2.25m, 3.0m, 3.75m, 4.5m, 5.25m and 6.0m. Each simulation was run for 10 seconds.

Test Case	Mean Flow Speed, U (ms^{-1})	Wave Amplitude, a (m)	Corrected Wave Amplitude (m)
7D	1.085	0.01	0.00625
7E	1.085	0.02	0.0125
7F	2.17	0.01	0.01
7G	2.17	0.02	0.02

Table 7.5: Semi-Free hull test cases.

The maximum positive vertical displacement and maximum pitch angle of the hull is measured over time once the oscillations have reached a regular state. The value of the maximum positive vertical motion is non-dimensionalised according to the following equation:

$$z_a'' = \frac{z_a}{a} \tag{7.5}$$

Where z_a'' is non-dimensionalised value of the maximum vertical displacement, z_a is the maximum vertical displacement and a is the wave amplitude. The value of the maximum pitch angle is non-dimensionalised according to the following equation:

$$\theta_a'' = \frac{\theta_a}{k \times a} \tag{7.6}$$

Where θ_a'' is the non-dimensionalised pitch angle, θ_a is the corrected maximum pitch angle and k is the angular wavenumber (see equation 5.1). θ_a is corrected by finding the maximum pitch angle measured once the oscillations have reached a regular state and subtracting the average pitch angle measured once the oscillations have reached a regular state.

Following the discovery of problems with the measurements taken during the simulations a second series of simulations were conducted to investigate whether these problems were being caused by the time step. The second set of simulations use a time step (dt) of 0.0001 seconds which is 10 times smaller than that used in the first set of simulations.

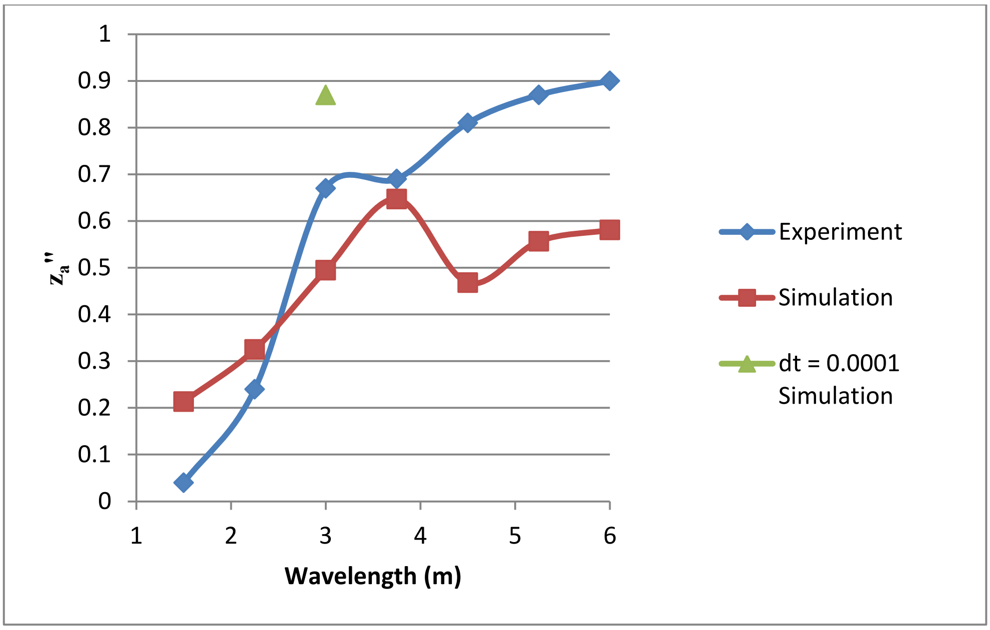

Figure 7.13: Test case 7D, heave motion measurements.

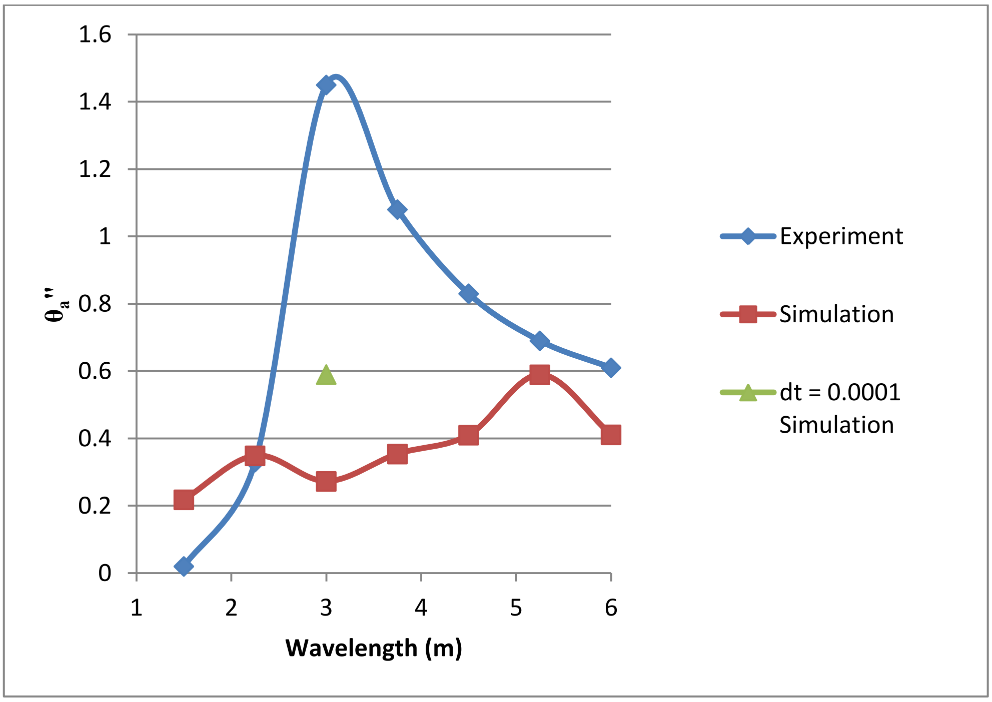

Figure 7.14: Test case 7D, pitching motion measurements.

Figures 7.13 and 7.14 show the results from test case 7D. The heave motion simulation results show reasonable agreement with the experimental results for the lower wavelengths (1.5m, 2.25m, 3.0m and 3.75m). The simulation results for higher wavelengths (4.5m, 5.25m and 6.0m) show the same trend as the experimental results. However, the simulation results are lower than the experimental results. The pitch motion simulation results show reasonable agreement with the experimental results for the shortest and longest wavelengths. However, values of the simulation results for the other wavelengths are much lower than the experimental results.

The 3.0m simulation was rerun using a smaller time step (dt = 0.0001 seconds) to investigate what effect this alteration would have upon the results. The pitching motion results shown in figure 7.14 show that the smaller time step simulation result is closer to the experimental result than that measured in the greater time step simulation. However the smaller time step simulation result is still much less than the experimental result. The heave motion results shown in figure 7.13 show that the result from the smaller time step simulation is greater than the experimental results. On the other hand the result from the greater time step simulation was less than the experimental result.

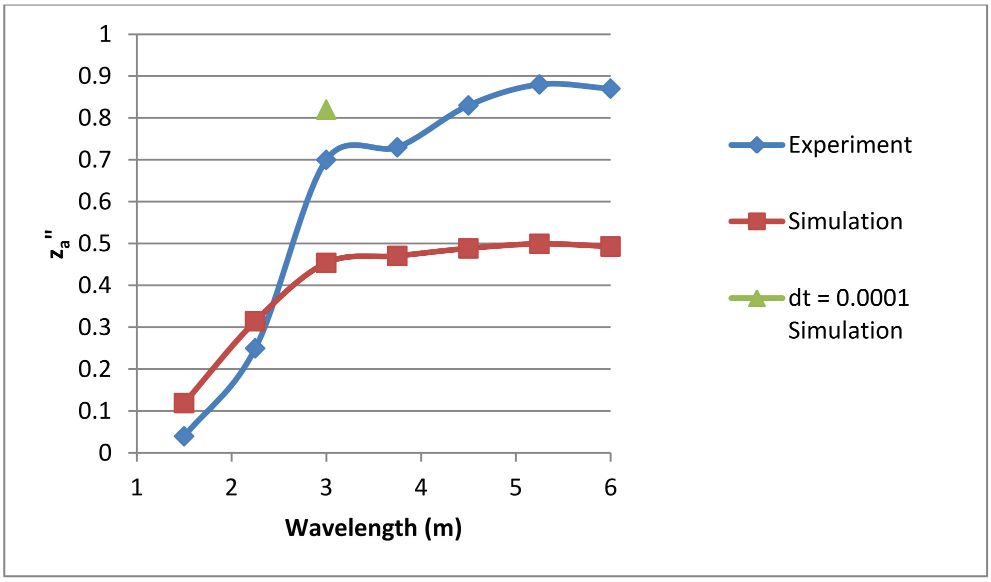

Figure 7.15: Test case 7E, heave motion measurements.

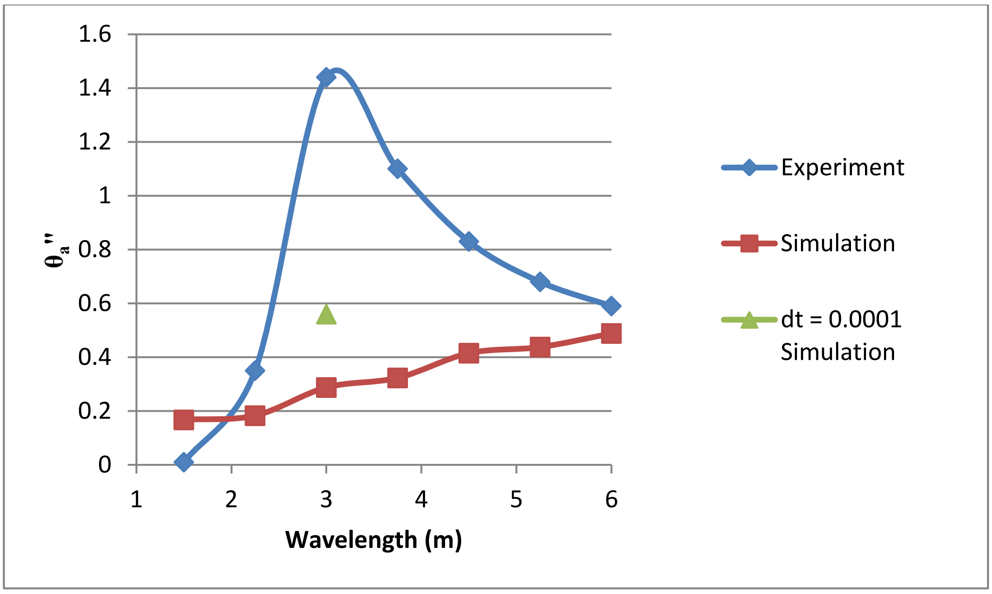

Figure 7.16: Test case 7E, pitching motion measurements.

Figures 7.15 and 7.16 show the results for test case 7E. The heave motion simulation results agree relatively well with the experimental results for the first two wavelengths (1.5m and 2.25m). Conversely, the results for the other wavelengths are much lower than the experimental results. The trend seen in the experimental results is not seen in the simulation results. The maximum heave motion appears to reach a limit of $z_a'' = 0.5$ regardless of wavelength. This result was not observed in either test case 7D or the restrained hull test cases. The pitching motion simulation results show the same pattern as seen in the previous test case although the discrepancy between the simulation and experimental results is greater in this case.

The 3.0m simulation was rerun using a smaller time step to investigate what effect this alteration would have upon the results. The results of the second simulation are similar to those observed in test case 7D. The pitching motion result from the second simulation is greater than the first simulation but still much less than the experimental results. The heave motion results show that the result from the second simulation is greater than the experimental result.

The reason that the second set of simulations was conducted using a wavelength of 3.0m is that the pitching motion results for this wavelength from the first set of simulations showed the greatest discrepancy compared to the experimental results. The results from test cases 7D and 7E show the same results, the heave motion results are greater than the experimental results. The difference between the second set of results and the experimental results is almost the same as the difference between the first set of results and the experimental results. The pitching motion results show a slight improvement over the measurements taken in the first set of simulations, but the results are still much less than the experimental results. The results from the second set of simulations show little improvement over the first set of simulations so it can be concluded that the effect of decreasing the time step provides only a very small benefit but an increased cost in terms of the time taken to run each simulation. Due to this increase in the simulation run time no further simulations were conducted using the smaller time step.

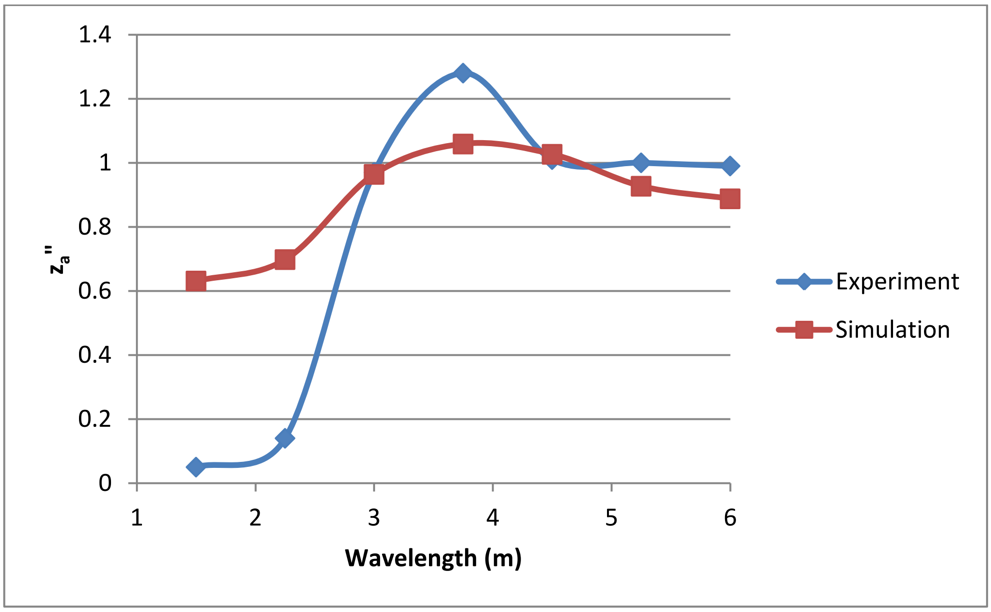

Figure 7.17: Test case 7F, heave motion measurements.

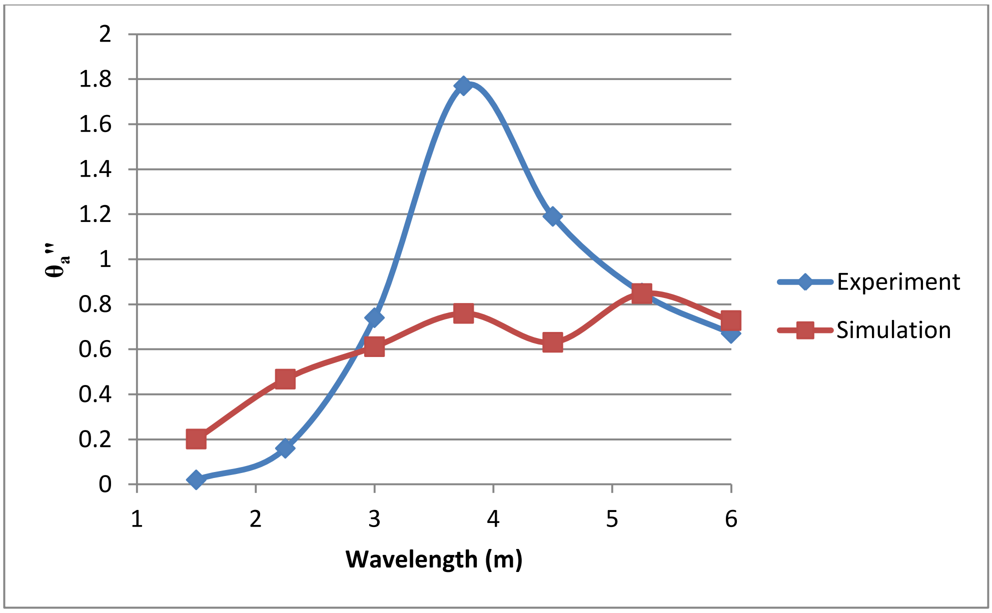

Figure 7.18: Test case 7F, pitching motion measurements.

Figures 7.17 and 7.18 show the results from test case 7F. The heave motion simulation results show a very different trend to the two preceding test cases (where the mean flow speed was 1.085ms^{-1}). Whereas the results from test cases 7D and 7E showed reasonable agreement with the experimental results at the lower wavelengths and then the results diverged as the wavelength increases in test case 7F the reverse is observed. The simulated results at the lower wavelengths over-predicted the maximum heave motion, but the results at higher wavelengths are more accurate. A further difference compared to the lower mean flow speed test cases is that the gradient of the maximum heave motion over wavelength is much less than that seen in test cases 7D and 7E.

The pitching motion simulation results show a similar pattern to that seen in test case 7D (which uses the same wave amplitude as test case 7F). The simulation results show some agreement with the experimental results at the lower and higher wavelengths. The simulation results at the medium wavelengths however are much lower than the experimental results. However, the difference between the simulated and experimental results is less than the difference observed in test case 7D.

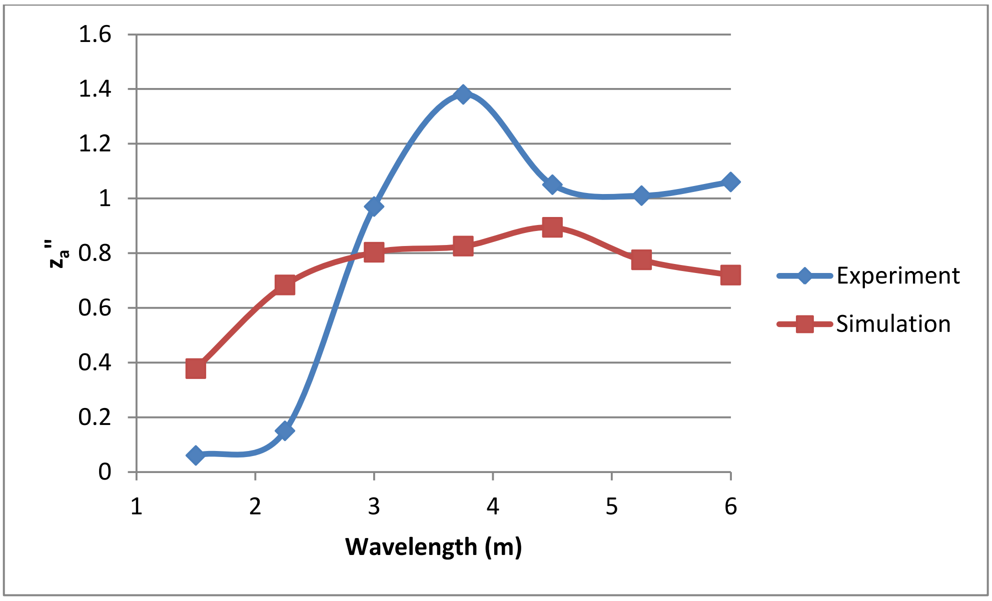

Figure 7.19: Test case 7G, heave motion measurements.

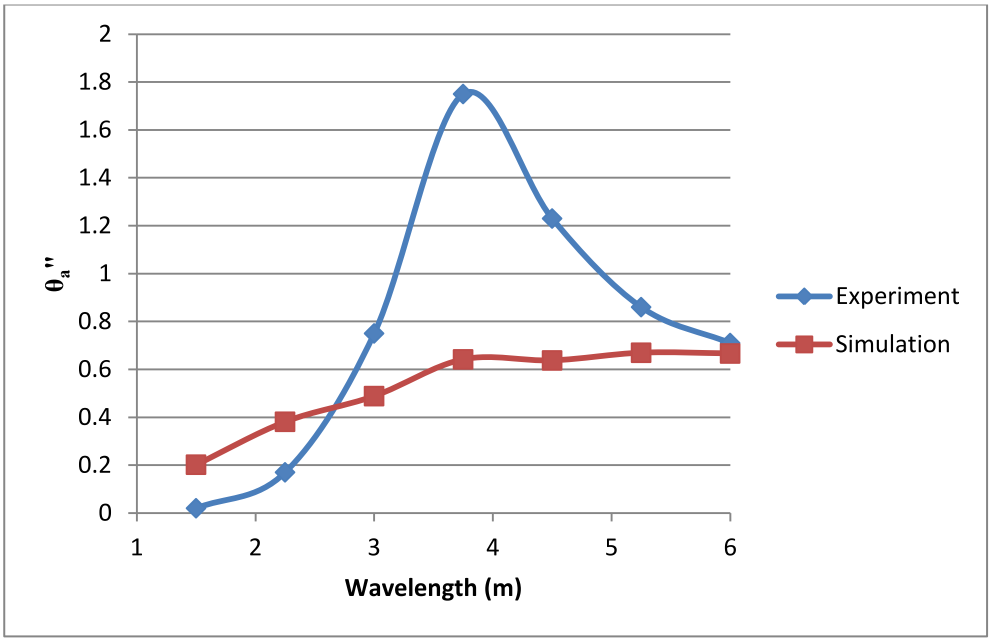

Figure 7.20: Test case 7G, pitching motion measurements.

Figures 7.19 and 7.20 show the results for test case 7G. The simulated heave motion results in this test case show as similar trend to that seen in test case 7F. The simulated results at lower wavelengths still over predicts the results as in test case 7F, but to a lesser degree. At higher wavelengths there is a greater discrepancy than in test case 7F as the simulated results under-predict the heave motion. The same low heave motion over wavelength gradient trend that was observed in test case 7F is seen here. The pitching motion simulated results show the same trend observed in test case 7E, which uses the same wave amplitude as test case 7G.

The results of the semi-free motion simulations are surprising as they do not show good agreement with the results of the fixed hull simulations. The results for the maximum pitching moment measured in the fixed hull simulations show reasonable agreement with the experimental results for all wavelengths in both test cases 7A and 7B (in both test cases the mean flow speed is 1.085ms^{-1}). However the results for test case 7C (where the mean flow speed is 2.17ms^{-1}) show over prediction of the maximum pitching moment for all wavelengths. The maximum pitching angle results for test cases 7D and 7E (where the mean flow speed is 1.085ms^{-1}) show reasonable agreement at the shorter and longer wavelengths (1.5m, 2.25m, 5.25m and 6.0m) the results for the intermediate wavelengths show a very large under prediction. The maximum pitching angle results for test cases 7F and 7G (where the mean flow speed is 2.17ms^{-1}) show a similar trend but the result for the simulations where the wavelength is 3.0m shows a similar degree of accuracy to the shorter and longer wavelengths. As with the results in test cases 7D and 7E the results at the intermediate wavelengths are much less than the experimental results.

Possible causes for the discrepancies observed in the maximum pitching angle results have been considered. An attempt to solve the problem by reducing the simulation time step by an order of magnitude was investigated. However the results show little improvement over the larger time step results. As the decrease in time step is significant no further benefit would be expected by decreasing the time step further. There is also a significant penalty in simulation run time when the time step is reduced significantly. For this reason further investigations on the effect of time step upon the results were discontinued.

The large bow wave that was observed in the fixed hull simulations where the mean flow speed was 2.17ms^{-1} was not observed in the semi-free hull simulations. It is possible that as the hull is free to pitch and heave in the semi-free hull simulations the bow wave causes the hull to heave upwards therefore reducing the blockage effect of the hull allowing the bow wave to move downstream. However, the large bow wave will cause an increase in the pitching moment. This may cause the maximum pitch angle to be lower. Whilst this may explain why the maximum pitch angle measured is too low at the intermediate wavelengths in the semi-free hull simulations it does not explain why the results at the shorter and longer wavelengths are much closer to the experimental results. It also does not explain why the maximum pitch angle measured at the intermediate wavelengths where the mean flow speed was 1.085ms^{-1} (test cases 7D and 7E) shows poor agreement with the experimental results as the large bow wave was not observed in the corresponding fixed hull simulations (test cases 7A and 7B).

A further potential cause for the under-prediction of the maximum pitching angle in all of the semi-free hull test cases is that whilst the fixed hull simulations showed reasonable agreement with the experimental results this was only for the case where the hull had a pitch angle of zero degrees. It is possible that the reason that the maximum pitch angle is under-predicted is that the pitching moment exerted on the hull is not correct when the hull is not at zero degrees of pitch. There is no data in Journée (1992) concerning the measurement of pitching moment measured when the hull is not a zero degrees of pitch so this hypothesis cannot be investigated. However the likelihood of this being the cause of the under-prediction of the maximum pitch angle at the intermediate wavelengths is low precisely because the under-prediction occurs only at the intermediate wavelengths. If this hypothesis were accurate then it would be expected that the maximum pitch angle would be inaccurate at all wavelengths not just specific wavelengths.

Another potential cause of the under-prediction of the maximum pitch angle that has not been investigated is the effect of the spatial resolution upon the results. The spatial resolution and dimensions of the computational domain have been selected as they allow for the best spatial resolution and largest computational domain that is possible when using the single CPU version of SPHysics. To increase the spatial resolution further would require the use of the parallel version of SPHysics. This requires significant modification of the standard version of parallel SPHysics to incorporate the new features that have been described in this and previous chapters. The time required to complete the conversion of the standard version of parallel SPHysics and the subsequent testing that would be needed prevented this course of action being undertaken.

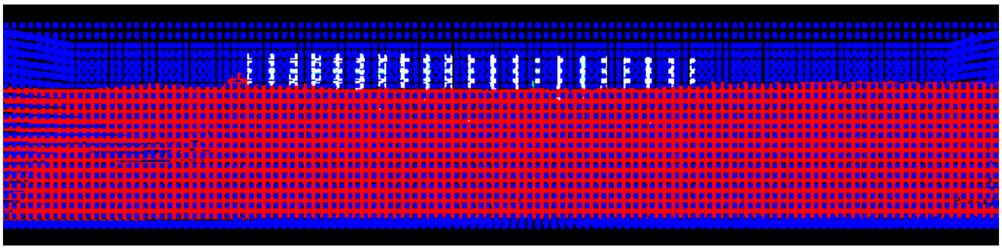

Figure 7.21: Test case 7D, wavelength = 3.0m, time step = 0.0001s. Side elevation at t = 9.875s.

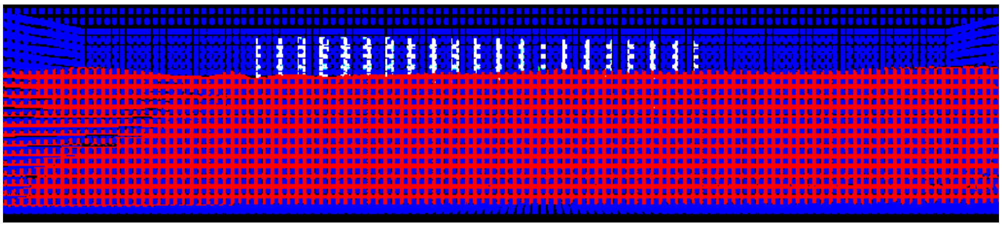

Figure 7.22: Test case 7D, wavelength = 3.0m, time step = 0.0001s. Side elevation at t = 9.375s.

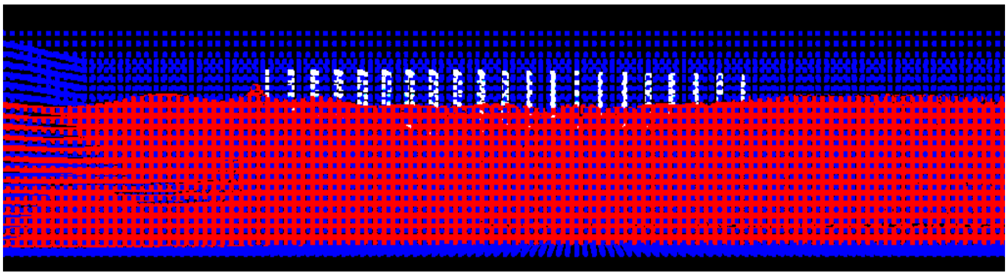

Figure 7.23: Test case 7E, wavelength = 3.0m, time step = 0.0001s. Side elevation at t = 9.875s.

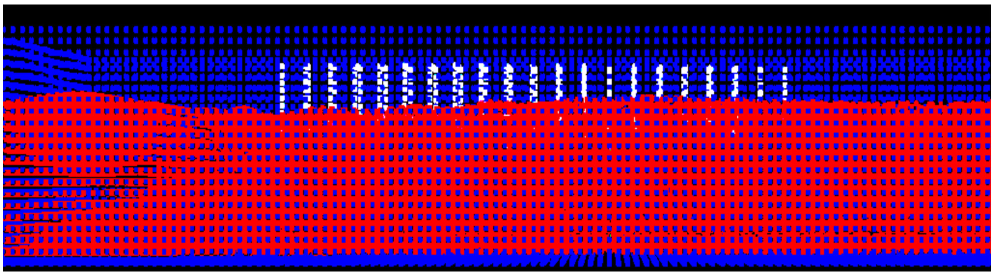

Figure 7.24: Test case 7E, wavelength = 3.0m, time step = 0.0001s. Side elevation at t = 9.375s.

Figures 7.21-7.24 show screenshots of the side elevations of test cases 7D and 7E, where the mean flow speed was 1.085ms^{-1}. All of the screenshots show simulations where the wavelength was 3.0m. It can be seen that in figures 7.21 and 7.23, which were taken 9.875 seconds after the simulations were begun that there is a bow wave present. This bow wave is not seen in figures 7.22 and 7.24, which were taken 9.375 seconds after the simulations were begun. The bow waves seen in figures 7.21 and 7.23 are also not as large as the bow wave seen in figure 7.12. The fact that the bow wave is present in both simulations at t = 9.875s but not present at t = 9.375s shows that the bow wave observed in figures 7.21 and 7.23 is not a permanent feature as was the case with the bow wave observed in the fixed hull simulations (test case 7C).

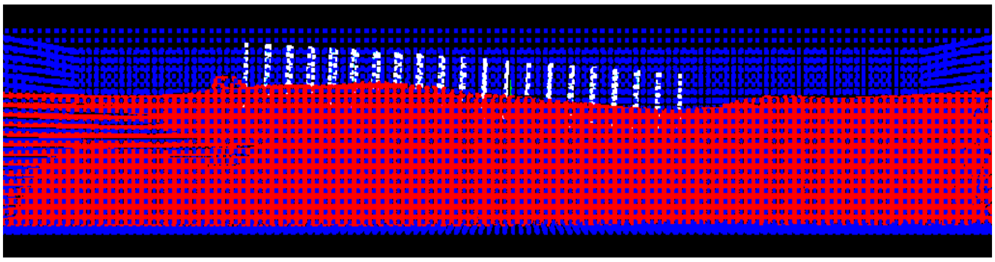

Figure 7.25: Test case 7G, wavelength = 4.5m, time step = 0.001s. Side elevation at t = 9.875s.

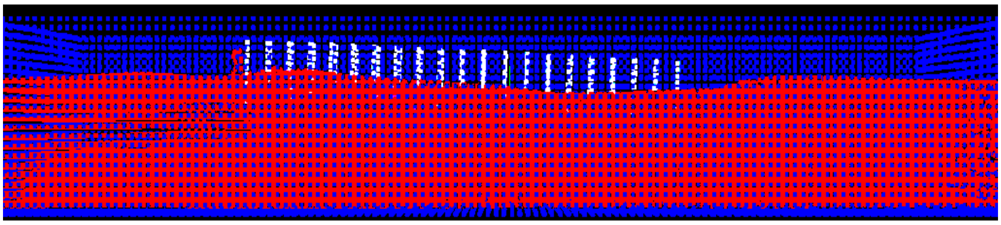

Figure 7.26: Test case 7G, wavelength = 4.5m, time step = 0.001s. Side elevation at t = 9.375s.

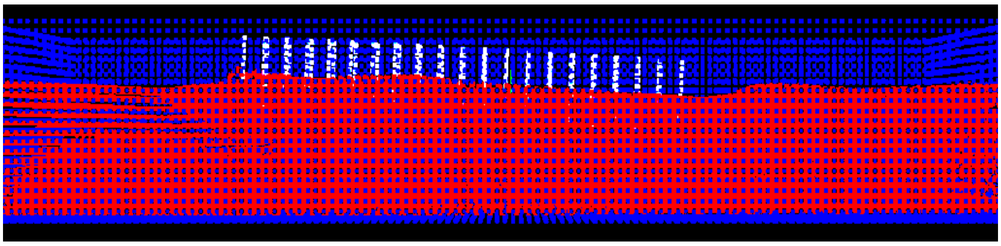

Figure 7.27: Test case 7G, wavelength = 4.5m, time step = 0.001s. Side elevation at t = 8.875s.

Figures 7.25, 7.26 and 7.27 show screenshots of the side elevation in test case 7G (where the mean flow speed was 2.17ms^{-1}), the wavelength in this simulation was 4.5m. The bow wave is present once more, however in figure 7.26 it extends to a greater height than is seen in figures 7.21 and 7.23, this is entirely expected as the mean flow speed in test case 7G is twice that used in test cases 7D and 7E. Also the bow wave in figure 7.26 is smaller than that seen in figure 7.12; test cases 7G and 7C use a mean flow speed of 2.17ms^{-1} and although the wave amplitude used in test case 7C is greater than that used in test case 7G the height of the bow wave in figure 7.12 is much greater than would be expected because of the larger wave amplitude used in test case 7C.

The bow wave that is observed in test cases 7D and 7E is seen to appear and disappear in a cycle, figure 7.27 shows the minimum bow wave height found in the final cycle in test case 7G. It is clear that the bow wave does not disappear in this case. The bow wave that is generated in test cases 7D and 7E must be being produced solely by the incoming waves, however the bow wave generated in test case 7G does not disappear at all during a cycle so must be being generated partly by the incoming waves but a second component of the bow wave is caused by the mean flow. This phenomenon is seen in the fixed hull test case although the component of the wave created by the mean flow is much larger. The smaller bow wave observed in the semi-free hull test cases could be a factor behind the under-prediction of the maximum pitch angle at the intermediate wavelengths although the under-prediction does not occur at the lower or higher wavelengths.

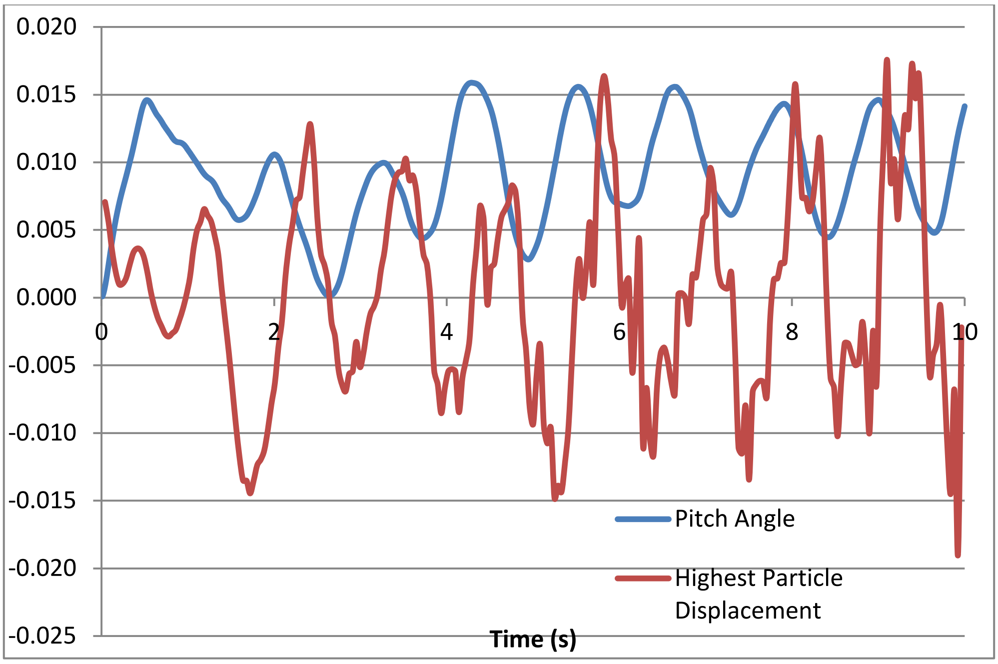

Figure 7.28: Wave and pitch motion frequency comparison. Test case 7D, wavelength 3.0m.

Figure 7.28 shows a comparison between the pitch angle of the hull and the highest particle displacement (the maximum particle height minus the average maximum particle height across the entire simulation). This figure shows that the pitching motion of the hull has the same frequency as the incoming waves, therefore it can be seen that the frequency of the hulls' motion is correct only the amplitude of the motion is inconsistent with the experimental results. The cause of the pitch amplitude being too low is damping of the motion. There are a number of factors that may cause the excessive damping, a likely candidate is the hull viscosity being set too high. The hull is modelled as a movable boundary and therefore has a user-defined viscosity similar to the immovable boundaries that form the edge of the computational domain.

To investigate the effect of reducing the hull viscosity two test cases were run that were identical to the 3.0m wavelength test case 7D except that the hull viscosity value is varied. The original hull viscosity value used was $100\text{m}^2\text{s}^{-1}$; the first simulation used a hull viscosity value of $0.0\text{m}^2\text{s}^{-1}$ and the second used a value of $10\text{m}^2\text{s}^{-1}$. The results of these simulations are shown in table 7.6.

	Heave	Pitch
Experimental	0.67	1.45
Original Simulation ($100m^2s^{-1}$)	0.4948	0.2725
Hull Viscosity = $10m^2s^{-1}$	0.4100	0.2630
Hull Viscosity = $0.0m^2s^{-1}$	0.4723	0.2514

Table 7.6: Hull viscosity tests.

The results of the hull viscosity tests show that both the heave and pitch results differ very little from the original simulation results. Decreasing the hull viscosity did not increase the maximum pitch angle as expected, as the hull viscosity is decreased the maximum pitch angle decreases slightly. The heave results show no discernible pattern.

The heave force results for the fixed hull test cases show reasonable agreement with the experimental results, as with the pitch results this pattern does not translate over to the heave motion results for the semi-free hull test cases. There are two trends in the heave motion results for the semi-free test cases, the mean flow speed determines which trend the results belong to.

The results for test cases 7D and 7E, where the mean flow speed was $1.085ms^{-1}$, show reasonable agreement with the experimental results at the low and medium wavelengths but the results at the high wavelengths are lower than the experimental results. The results for test cases 7F and 7G, where the mean flow speed is $2.17ms^{-1}$, show almost the opposite trend. The simulation results show better agreement with the experimental results at the medium and higher wavelengths than the simulation results at low wavelengths.

It is clear that the mean flow speed is having an effect on the accuracy of the results, one consequence of varying the mean flow speed is the correction made to the input wave amplitude suggested in the previous chapter. When the mean flow speed is $1.085ms^{-1}$ the wave amplitude is reduced by a factor of 1.6, in the test cases where the mean flow speed is $2.17ms^{-1}$ no correction is applied. When compared to the heave motion results trends it can be seen that when the wave amplitude is reduced the results show either reasonable agreement or an under-prediction compared to the experimental results. Conversely when no wave amplitude correction is applied the results show either reasonable agreement or an over-prediction compared to the experimental results. It is possible that the although if the wave correction reduces the input wave amplitude produces waves of the desired amplitude the energy in the waves is too low and therefore the hull will not be displaced vertically as much as it should be.

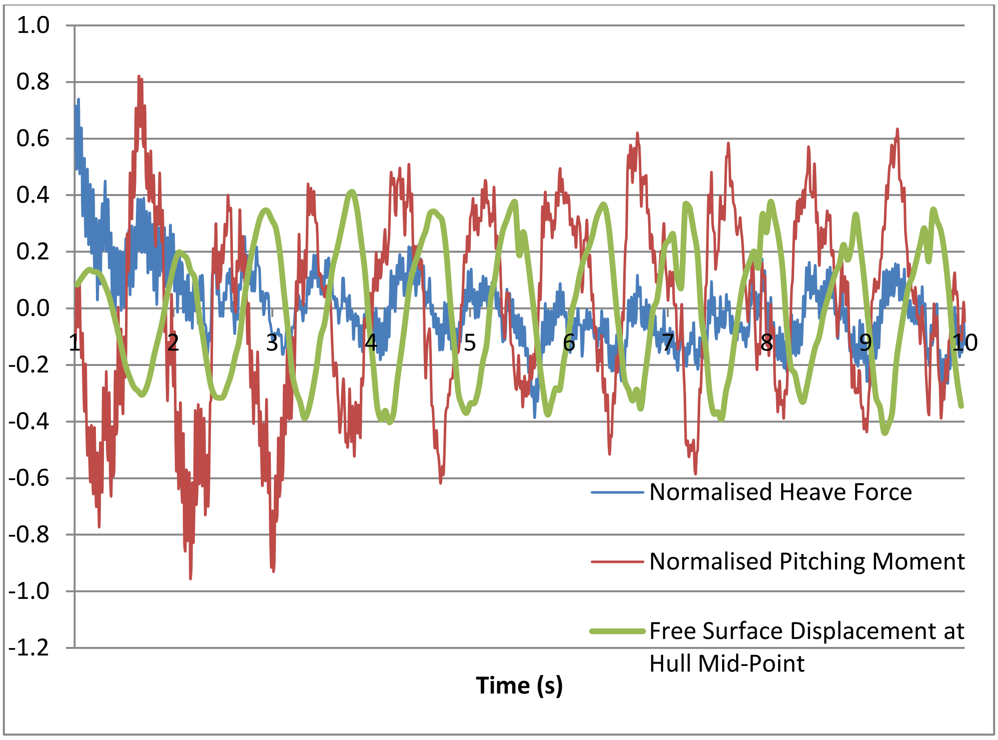

Figure 7.29: Test case 7A, wavelength = 1.5m. Comparison between heave force, pitching moment and free surface displacement at hull mid-point.

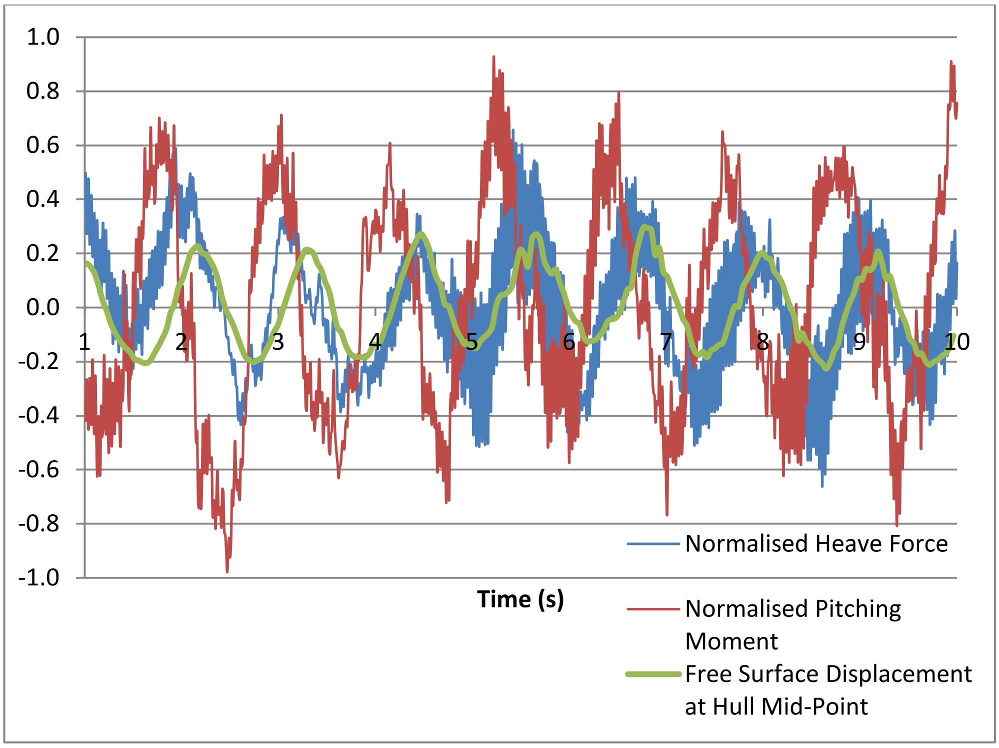

Figure 7.30: Test case 7A, wavelength = 3.0m. Comparison between heave force, pitching moment and free surface displacement at hull mid-point.

Figures 7.29 and 7.30 show a comparison between the normalised heave force and pitching moment measured during test case 7A compared to the free surface displacement at the mid-point of the hull. The purpose of these figures is to compare the phase difference between the maximum measured heave force and pitching moment and the peak of a wave passing the mid-point of the hull. The phase difference in figure 7.29 appears to be approximately 140 degrees the equivalent result for figure 7.29 in Journée (1992) is 110 degrees. The phase difference in figure 7.30 appears to be similar to the previous result however the equivalent result in Journée (1992) is 286 degrees. This may be the reason that the results for the shorter wavelengths in the semi-free test cases is much more accurate than the results for the higher wavelengths.

7.4 - Conclusions

All of the novel methodologies that have been presented in the previous chapters have been brought together in this chapter to simulate a Wigley hull in a wave tank using the results in Journée (1992) for comparison. Both restrained and semi-free motion test cases have been conducted and the mean flow speed, wave amplitude and wavelength used varied in each test case. A problem with an overly large bow wave being generated at the higher flow speed during the restrained hull test cases was observed, however this problem did not occur to such an extent during the semi-free test cases. Suggestions have been made as to the source of the errors in the semi-free hull test cases. A possible avenue for further investigation has been discovered, that the phase of the pitching moment and heave force measured during the fixed hull test cases does not match that in Journée (1992) for medium to longer wavelength waves.

Chapter 8

Conclusions and Future Work

8.1 - Conclusions

The objectives of this thesis were to:

1. Develop a robust inflow-outflow boundary condition that can allow a channel flow to be simulated in both two and three dimensions.
2. Create a wave generator that is capable of generating regular waves and works with the inflow boundary to generate a channel flow with waves.
3. Devise a wave damping mechanism that can be placed at the outflow end of the domain to damp out waves to prevent unwanted wave reflection. Combined with objectives 1 and 2 this will allow for the simulation of a wave tank.
4. Modify the floating body method within SPHysics to simulate a ships' hull.
5. Combine all of the features together to allow a floating body to be simulated in a wave tank with a mean flow.

The open source code SPHysics has been investigated and adapted with the ultimate aim of simulating the motion of a ships' hull in regular head waves. The benefits and drawbacks of the various boundary methods that have been used in SPH methods have been discussed and the most promising have been tested. The experimental data in Yim *et al* (2008) has been used as the basis of a test case for a proposed non-reflecting open boundary methodology that was developed to be a simple and efficient adaptation of the repulsive boundary method in SPHysics. The methodology was found not able to function correctly as a non-reflecting open boundary as the simulations showed that wave reflection was occurring, therefore not meeting the third thesis objective.

After dismissing the proposed methodology for a non-reflecting open boundary in chapter 4 a new methodology was devised. This was described in chapters 5 and 6. The new methodology combined a non-reflecting open boundary with an inflow method with the capability to generate regular waves, thus meeting the second thesis objectives and is the first novel contribution. The wave generator is described in chapter 5, it is shown that the wave generator is capable of generating regular head waves in 2D. Excessive wave damping has been identified but this is only significant over relatively long distances meaning that if the distances involved in a test case are short then the problem will not have a significant effect on the results.

The wave generator outlined in chapter 5 has been combined with a new wave damping and outflow methodology presented in chapter 6. This is the second novel contribution of the thesis. The method is tested in both 2D and 3D and the performance of the wave damping is very good. The wave damping method is adaptable dependant on the situation. This allows the performance of the wave damping mechanism to be balanced against the computational cost of the implementation. The wave generator can be combined with an inflow mechanism that creates a mean flow with regular waves. A problem with the amplitude of the waves that are generated has been identified and a solution has been proposed that corrects the original error. The methodologies described in chapters 5 and 6 are combined to create the ability to simulate a 2 or 3 dimensional channel flow with regular head waves. The work described up to this point meets the first, second and third objectives of the thesis.

The methodologies developed in the preceding chapters are used in chapter 7 to simulate the experiments carried out in Journée (1992), this satisfies the fourth and fifth objectives and is the third novel contribution. Both fixed hull and semi-free hull simulations have been conducted, the fixed hull simulations show reasonable prediction of the heave forces and pitching moments when compared to the experimental results. However the maximum heave displacements and pitching angles measured in the semi-free hull simulations show a worse agreement with the experimental results. This is unexpected given the level of agreement between the experimental and simulation results in the fixed hull simulations. Numerous suggestions have been made as to the cause of this discrepancy.

8.2 - Future Work

The work presented in this thesis provides a framework for further development; there are numerous experiments that have been conducted concerning ships in wave tanks, using the framework presented in this thesis further validation simulations could be conducted. The rigid body motion mechanism within SPHysics has 6 degree of freedom capability, this further extends the array of validation studies that could be conducted.

The development of the parallel and hybrid (central and graphical processing unit) versions of SPHysics open up the possibility of increasing the spatial resolution of the simulations by fully utilising modern computer hardware. The methodologies presented in this thesis are readily adaptable to conversion to these newer versions of SPHysics. The wave generator is also capable of generating non-regular waves with minimal alteration to the wave generator methodology.

The problem of excessive wave damping will be a problem in some test cases where the length of the simulation domain is long. The problem could be being caused by the low spatial resolution used. The new versions of SPHysics will allow the effect of increasing spatial resolution to be investigated.

A problem that was noted during the Wigley hull test cases was the presence of an overly large bow wave, this may not have been caused by the simulation of the fluid but the way that the hull was modelled. The bow of the hull is modelled as two vertical column of particles that are located at the same longitudinal and lateral position. An alternative solution would be to model the bow using two vertical columns of particles that are at the same longitudinal position but with each column displaced laterally. It is possible that the original geometry is causing the large bow wave as there is no lateral gap between the hull particles at the bow. The original and proposed solutions are shown in figure 8.1.

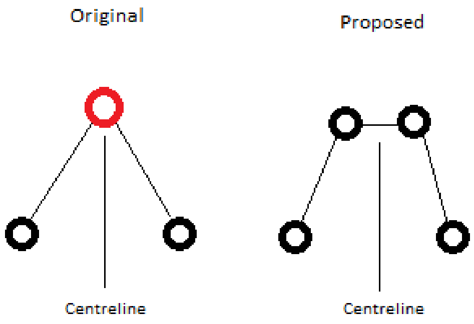

Figure 8.1: Original and proposed bow geometry.

Appendix A - Published Papers

1. **Pearce M., Takeda T., Hudson D.**. "Prediction of ship motions for a Wigley Hull", *Proc. 6th International SPHERIC Workshop*, ISBN: 978-3-89220-658-3, Editors T.Rung & C.Ulrich, Hamburg 8-10 June, 2011, p. 226-232.
2. **Pearce M., Thomas G., Hudson D.**. "Using SPHysics to simulate a Wigley hull in head waves", *Proc. 7th International SPHERIC Workshop*, Prato 29-31 June, 2012, p. 252-258.

References

Airy, G. B., *Tides and waves,* 1841. In Hugh James Rose, et al. Encyclopædia Metropolitana.

Atluri S. N. and Zhu T., *A new meshless local Petrov-Galerkin (MPLG) approach in computational mechanics,* 1998. Computational Mechanics, 22:117-127.

Belytschko T., Lu Y. Y. and Gu L., *Element-Free Galerkin methods, 1994. International Journal for Numerical Method in Engineering,* 37:229-256.

Bierbrauer, F., Bollada, P. C. and Phillips, T. N., *A Consistent Reflected Image Particle Approach to the Treatment of Boundary Conditions in Smoothed Particle Hydrodynamics.* 2009, Comput. Methods Appl. Mech. Engrg., pp. 198:3400-3410.

Bouscasse B., Marrone S., Colagrossi A. and Broglia R., *SPH simulations of bow wave dynamics.* 2012. Proceedings of the 7th International SPHERIC Workshop.

Cartwright, B. et al, *Motion Prediction of Ships and Yachts by Smoothed Particle Hydrodynamics.* 2006. 2nd High Performance Yacht Design Conference.

Chang K.-H. and Chang T.-J., *SPH modeling of non-rectangular channel flows with open boundaries.* 2012. Proceedings of the 7th International SPHERIC Workshop.

Cherfils, J.-M. et al, *IB-SPH Simulations of Wave-Body Interactions.* 2010. Proceedings of the 5th International SPHERIC Workshop.

Colagrossi, A. and Landrini, M., *Numerical Simulation of Interfacial Flows by Smoothed Particle Hydrodynamics.* 2003, Journal of Computational Physics, pp. 191:448-475.

Colagrossi, A., Antuono, M. and Le Touzé, D., *Theoretical Considerations on the Free-Surface Role in the Smoothed-Particle-Hydrodynamics Model.* 2009, Physical Review.

Crespo, A. J. C., *Application of the Smoothed Particle Hydrodynamics Model SPHysics to Free-Surface Hydrodynamics.* s.l. : PhD Thesis, 2008.

Crespo, A. J. C. et al., *Development of a Dual CPU-GPU SPH Model.* 2010. Proceedings of the 5th International SPHERIC Workshop.

Dalrymple, R. A. and Knio, O., *SPH Modelling of Water Waves.* 2001, Proc. Coastal Dynamics, Lund, pp. 779-787.

De Padova, D. et al, *Hydraulic Jump Simulation by SPH.* 2010. Proceedings of the 5th International SPHERIC Workshop.

Delorme, L. et al, *A Set of Canonical Problems in Sloshing, Part I: Pressure Field in Forced Roll - Comparison Between Experimental Results and SPH.* 2009, Ocean Engineering, pp. 36:168-178.

DualSPHysics code v1.0. *http://www.dual.sphysics.org.*

Duarte C. A. and Oden J. T., *An HP adaptive method using clouds, 1996. Computer Methods in Applied Mechanics and Engineering,* 139:237-262.

Federico, I. et al, *Simulating Free-Surface Channel Flows Through SPH.* 2010. Proceedings of the 5th International SPHERIC Workshop.

Fernández-Méndez, S., Bonet, J. and Huerta, A., *Continuous Blending of SPH with Finite Elements.* 2005, Computers and Structures, pp. 83:1448-1458.

Ferrand, M. et al., *Improved Time Scheme Integration Approach for Dealing with Semi Analytical Boundary Conditions in SPARTACUS2D.* 2010. Proceedings of the 5th International SPHERIC Workshop.

Ferrari, A. et al, *A New 3D Parallel SPH Scheme for Free Surface Flows.* 2009, Computers & Fluids, pp. 38:1203-1217.

Fleissner, F. and Eberhard, P., *Load Balanced Parallel Simulation of Particle-Fluid DEM-SPH Systems with Moving Boundaries.* 2007, Parallel Computing: Architectures, Algorithms and Applications, pp. NIC Series Vol. 38:37-44.

Gerritsma, Ir. J., *Motions, Wave Loads and Added Resistance in Waves of Two Wigley Hull Forms.* s.l. : Delft University of Technology, 1988.

Gingold R. A. and Monaghan J. J., *Smoothed Particle Hydrodynamics: Theory and Application to Non-spherical stars,* 1977. Monthly Notices of the Royal Astronomical Society, 181:375-389.

Gómez-Gesteira, M. et al, *User Guide for the SPHysics Code v1.4.* http://www.sphysics.org, 2008.

Groenenboom P. H. L. and Cartwright B. K., *SPH Simulations of Free Surface Waves and the Interactions with Objects.* 2010. V European Conference on Computational Fluid Dynamics.

Guo B. J., Steen S. and Deng G. B., *Seakeeping Prediction of KVLCC2 in head waves with RANS,* 2012. Applied Ocean Research 35, 56-67.

Harada, T., Koshizuka, S. and Kawaguchi, Y., *Smoothed Particle Hydrodynamics on GPUs.* 2007, In Proc. of Computer Graphics International, pp. 63-70.

He, J. et al., *Real-Time Adaptive Fluid Simulation with Complex Boundaries.* 2010, Vis Comput, pp. 26: 243-252.

Hoetzlein, R. and Höllerer, T., *Analyzing Performance and Efficiency of Smoothed Particle Hydrodynamics.* 2008.

Journée, J. M. J. *Experiments and Calculations on 4 Wigley Hull Forms in Head Waves.* s.l. : Delft University of Technology, 1992.

Kelager, M., *Lagrangian Fluid Dynamics Using Smoothed Particle Hydrodynamics.* s.l. : University of Copenhagen, Jan. 2006.

Kim, B. and Shin, Y-S., *Steady Flow Approximations in Three-Dimensional Ship Motion Calculation.* 2007, Journal of Ship Research, pp. Vol. 51, No. 3, 229-249.

Lastiwka, M., Basa, M. and Quinlan, N., *Permeable and Non-Reflecting Boundary Conditions in SPH.* 2009, International Journal for Numerical Methods in Fluids, pp. 61:709-724.

Lehnart, A., Fleissner, F. and Eberhard, P., *An Alternative Approach to Modelling Complex Smoothed Particle Hydrodynamics Boundaries.* 2010. Proceedings of the 5th International SPHERIC Workshop.

Lennard-Jones, J. E., *On the Determination of Molecular Fields.* 1924. Proc. R. Soc. Lond. A, 106 (738): 463-477.

Lewis, S. G. et al, *Impact of a Free-Falling Wedge with Water: Synchronized Visualization, Pressure and Acceleration Measurements.* 2010, Fluid Dynamics Research.

Libersky, L. D. and Petscheck, A. D., *Smoothed Particle Hydrodynamics with Strength of Materials.* 1991, Proceedings of the Next free Langrange Conference, pp. Volume 395, Pages 248-257.

Lind S. J., Xu R., Stansby P. K. and Rogers B. D., *A Stabilising Diffusion-Based Shifting Algorithm for Incompressible Smoothed Particle Hydrodynamics.* 2011. Proceedings of the 6th International SPHERIC Workshop.

Liszka T. and Orkisz J., *The finite difference method at arbitrary irregular grids and its applications in applied mechanics,* 1980. Computers and Structures, 11:83-95.

Liu G. R. and Gu Y. T., *A point interpolation method, 1999. Proceedings of 4th Asia-Pacific Conference on Computational Mechanics,* pp. 1009-1014.

Liu G. R. and Gu Y. T., *A truly meshless method based on the strong-weak form, 2002. Liu G. R. (Ed.) Advances in Meshfree and X-FEM Methods,* pp. 259-261.

Liu M. B. and Liu G. R., *Smoothed Particle Hydrodynamics (SPH): an Overview and Recent Developments*. 2010. Arch Comput Methods Eng, 17: 25-76.

Liu W. K., Jun S. and Zhang Y. F., *Reproducing Kernel Particle Methods, 1995. International Journal for Numerical Methods in Fluids,* 20:1081-1106.

Lucy L. B., *Numerical approach to testing the fission hypothesis,* 1977. Astronomical Journal, 82:1013-1024.

Macià F., Souto-Iglesias A., Antuono M. and Colagrossi A., *Benefits of using a Wendland kernel for free-surface flows.* 2011. Proceedings of the 6th International SPHERIC Workshop.

Mahmood O., Voileau D., Kassiotis C., Rogers B. D. and Ferrand M., *Absorbing Inlet/Outlet boundary conditions for 2D SPH turbulent free-surface flows*. 2012. Proceedings of the 7th International SPHERIC Workshop.

Marrone, S. et al., *Violent Fluid-Structure Impacts Solved Through a δ-SPH Model.* 2010. Proceedings of the 5th International SPHERIC Workshop.

Marrone S., Bouscasse B., Colagrossi A. and Antuono M., *Study of ship wave breaking patterns using 3D parallel SPH simulations,* 2012. Computers & Fluids 69, 54-66.

Marsh, A. et al, *Numerical Predictions of Ship Flooding Scenarios Using SPH.* 2010. Proceedings of the 5th International SPHERIC Workshop.

Modave A, Deleersnijder É. and Delhez É., *On the parameters of absorbing layers for shallow water models.* Ocean Dynamics, 2010 60:65-79.

Monaghan, J. J., *On the Problem of Penetration in Particle Methods.* 1989, Journal of Computational Physics, 82:1-15.

Monaghan, J. J., *Simulating Free Surface Flows with SPH.* 1994, Journal of Computational Physics, pp. 110:399-406.

Monaghan, J. J. and Kos, A., *Solitary Waves on a Cretan Beach.* 1999, J. Waterway, Port, Coastal and Ocean Engineering, pp. 125:145-154.

Monaghan, J. J., Kos, A. and Issa, N., *Fluid Motion Generated by Impact.* 2003, J. Waterway, Port, Coastal and Ocean Engineering, pp. 129(6):250-259.

Narayanaswamy, M. S., *A Hybrid Boussinesq-SPH Wave Propagation Model with Applications to Forced Waves in Rectangular Tanks.* s.l. : PhD Thesis, 2008.

Nayroles B., Touzot G. and Villon P., *Generalizing the finite element methods: diffuse approximation and diffuse elements,* 1992. Computational Mechanics, 10:307-318.

Oger, G. et al., *Hybrid CPU-GPU Acceleration of the 3-D Parallel Code SPH-Flow.* 2010. Proceedings of the 5th International SPHERIC Workshop.

ParallelSPHysics code v2.0. *http://www.sphysics.org.*

Price, W. G. and Chen, Y. G., *A Simulation of Free Surface Waves for Incompressible Two-Phase Flows Using a Curvilinear Level Set Formulation.* 2006, International Journal for Numerical Methods in Fluids, pp. 51:305-330.

Quérard, A. B. G., Temarel, P. and Turnock, S. R., *The Hydrodynamics of Ship-Like Sections in Heave, Sway and Roll Motions Predicted Using an Unsteady*

Reynolds-Averaged Navier-Stokes Method. 2009, Proc. IMechE Vol. 223 Part M: J. Engineering for the Maritime Environment.

Randles, P. and Libersky, L., *Smoothed Particle Hydrodynamics some Recent Improvements and Applications.* 1996, Comput. Methods Appl. Mech. Engineering, pp. 138:375-408.

Rogers, B. et al, *Smoothed Particle Hydrodynamics for Naval Hydrodynamics.* Le Croisic Nantes : s.n., 2003. Proc. Int. Workshop on Water Waves and Floating Bodies.

Shadloo, M. S., Zainali, A. and Yildiz, M., *Improved Solid Boundary Treatment Method for the Solution of Flow over an Airfoil and Square Obstacle by SPH Method.* 2010. Proceedings of the 5th International SPHERIC Workshop.

Shadloo M. S., Zainali A., Yildiz M. and Suleman A., *A robust weakly compressible SPH method and its comparison with an incompressible SPH.* 2012. Int. J. Numer. Meth. Engng. 89:939-956.

Shibata K., Koshizuka S., Sakai M. and Tanizawa K., *Lagrangian simulations of ship-wave iunteractions in rough seas,* 2012. Applied Ocean Research 42, 13-25.

Souto-Iglesias, A. et al., *Liquid Moment Amplitude Assessment in Sloshing Type Problems with Smoothed Particle Hydrodynamics.* 2006, Ocean Engineering, pp. 33:1462-1484.

Souto-Iglesias, A., Colagrossi, A. and Antuono, M., *SPH No-Slip BC Implementation Analysis at the Continuous Level.* 2010. Proceedings of the 5th International SPHERIC Workshop.

SPHysics code v1.4. *http://wiki.manchester.ac.uk/sphysics.*

SPHysics code v2.0. *http://www.sphysics.org.*

SPHysics code v2.2. *http://www.sphysics.org.*

Vacondio, R. et al, *SPH Shallow Water Equation Solver for Real Flooding Simulation.* 2010. Proceedings of the 5th International SPHERIC Workshop.

Vandamme J., Zou Q. and Reeve D. E., *Modelling Floating Object Entry and Exit Using Smoothed Particle Hydrodynamics.* 2011. Journal of Waterway, Port, Coastal and Ocean Engineering, September/October 2011, p. 213-224.

Vaughan, G. L., *The SPH Equations for Fluids.* 2009, International Journal for Numerical Methods in Engineering, pp. 79:1392-1418.

Vesterlund, M., *Simulation and Rendering of a Viscous Fluid Using Smooth Particle Hydrodynamics.* s.l. : University of Umea, Dec. 2004.

Vignjevic R. and Powell S., *Non-Reflecting Boundary Conditions and Multi-Resolution SPH.* 2011. Proceedings of the 6th International SPHERIC Workshop.

Weymouth, G. D., Wilson, R. V. and Stern, F., *RANS Computational Fluid Dynamics Predictions of Pitch and Heave Ship Motions in Head Seas.* 2005, Journal of Ship Research, pp. Vol. 49, No. 2, 80-97.

Yagawa G. and Yamada T., *Free mesh method: a new meshless finite element method, 1996. Computational Mechanics,* 18:383-386.

Yim, S. C. et al, *Numerical Simulations of Wave Generation by a Vertical Plunger Using RANS and SPH Models.* 2008, Journal of Waterway, Port, Coastal and Ocean Engineering, p. Vol. 134 No. 3 May 1st.

Bibliography

Airy G. B., *Tides and Waves*, in **Rose H. J. *et al***, *Encyclopaedia Metropolitania*, 3., 1817-1845.

Liu G. R. and Liu M. B., *Smoothed Particle Hydrodynamics a meshfree particle method*, World Scientific, 2003.